UC Berkeley
UC Berkeley Electronic Theses and Dissertations

Title
Modeling 3D Laplace-Fourier domain acoustic wave equation with free-surface topography using finite-difference

Permalink
https://escholarship.org/uc/item/7t40t6kh

Author
AlSalem, Hussain Jummah

Publication Date
2019

Peer reviewed|Thesis/dissertation

eScholarship.org Powered by the California Digital Library
University of California

Modeling 3D Laplace-Fourier domain acoustic wave equation with free-surface topography using finite-difference

by

Hussain J AlSalem

A dissertation submitted in partial satisfaction of the

requirements for the degree of

Doctor of Philosophy

in

Engineering – Civil and Environmental Engineering

and the Designated Emphasis

in

Computational and Data Science and Engineering

in the

Graduate Division

of the

University of California, Berkeley

Committee in charge:

Professor James Rector, Chair
Professor Gregory Newman
Professor Nicholas Sitar
Professor Douglas Dreger

Spring 2019

Modeling 3D Laplace-Fourier domain acoustic wave equation with free-surface topography using finite-difference

Copyright 2019
by
Hussain J AlSalem

Abstract

Modeling 3D Laplace-Fourier domain acoustic wave equation with free-surface topography using finite-difference

by

Hussain J AlSalem

Doctor of Philosophy in Engineering – Civil and Environmental Engineering

University of California, Berkeley

Professor James Rector, Chair

We develop embedded boundary methods to handle arbitrarily shaped topography to accurately simulate acoustic seismic wave propagation in Laplace-Fourier (LF) domain. The purpose is to use this method to enhance accurate wave simulation near the surface. Unlike most existing methods such as the ones using curvilinear grids to fit irregular surface topography, we use regular Cartesian grid system without suffering from staircasing error, which occurs in the conventional implementations. In this improved embedded-boundary method, we account for an arbitrarily curved surface by imposing ghost nodes above the surface and approximating their acoustic pressures using linear extrapolation, quadratic interpolation, or cubic interpolation. Implementing this method instead of using curvilinear grids near the boundaries greatly reduces the complexity of preprocessing procedures and the computational cost. Furthermore, using numerical examples, we show the accuracy gain and performance of our embedded-boundary methods in comparison with conventional finite-difference (FD) implementation of the problem.

In realistic 3D geological settings underlying topography surfaces with a large velocity contrast between shallow and deep regions, simulation of acoustic wave propagation in LF domain using a spatially uniform grid can be computationally demanding, due to over-discretization of the high-velocity material. We introduce a discontinuous mesh (DM) method that exchanges information between regions, discretized with different grid spacings, to improve efficiency and convergence. We present a 3D second- and fourth-order velocity-pressure staggered-grid FD DM acoustic wave propagation method in LF domain for acoustic wave estimation using any spatial discretization ratio between meshes. We evaluate direct and iterative parallel solvers for computational speed, memory requirements and convergence. Benchmarks in realistic 3D models with extreme and realistic topography examples show more efficient and stable results for DM with direct solvers relative to uniform mesh with iterative solvers.

To my parents, whose endless support has made this possible.

Contents

List of Figures

List of Tables

Acknowledgments

Foremost, I would like to express my sincere gratitude to my advisors Dr. Peter Petrov, Dr. Gregory Newman and Prof. James Rector for the continuous support of my PhD study and research, for their patience, motivation, enthusiasm, and immense knowledge. Their guidance helped me in all the time of research and writing of this thesis. I could not have imagined having better advisors and mentors for my PhD study. Besides my advisors, I would like to thank the rest of my thesis committee: Prof. Douglas Dreger and Prof. Nicholas Sitar for their encouragement and insightful comments. At the end I would like express appreciation to my beloved wife who spent sleepless nights with me and was always my support in the moments when there was no one to answer my queries.

Chapter 1

Overview

1.1 Acoustic wave equation analysis

Frequency-domain modeling of wave propagation inside the earth has been studied extensively (see Lysmer and Drake (1972); Marfurt (1984); Pratt and Worthington (1990); Zahradník and Urban (1984); Jo et al. (1996); Štekl and Pratt (1998); Hustedt et al. (2004); Operto et al. (2007)). Most of the methods that have been developed for wave modeling in the frequency domain are based on solving the acoustic wave equation by the finite-difference (FD) method: on a uniform grid, the FD methods provide an excellent compromise between accuracy and computational efficiency.

In Chapter 2, we solve the 3D acoustic wave equation analytically and numerically in Laplace-Fourier (LF) domain. We find the analytical solution for two cases: a point source in unbounded homogenous medium, and a point source in fluid half-space. The numerical solution is achieved using second- and fourth-order FD approximation. We conclude the chapter by comparing both solutions to test the accuracy of our FD numerical solutions.

1.2 Free-surface boundary

Special attention to the numerical treatment of the free-surface boundary for topography is deserved because it does not follow naturally from a Cartesian grid. For acoustic forward modeling, second- and fourth-order accurate FD methods do not implicitly satisfy the free-surface condition as is the case with finite-element methods. Accurately implementing the free-surface condition on an irregular interface is difficult due to the non-local nature of the FD schemes. It implies that acoustic velocities above the free-surface are required to compute the pressure at or immediately below the surface (Fichtner, 2011).

In Chapter 3, we describe an embedded-boundary method for simulating the three-dimensional acoustic wave equation with irregular free-surface boundary on a Cartesian grid. By computing pressure on both sides of the interface, we can satisfy a zero acoustic pressure at the free surface, yielding superior results compared to conventional implementations.

1.3 Numerical Simulations and Optimization

A significant challenge facing the numerical modeling of acoustic seismic wave propagation in LF domain is the increase in model size due to low near-surface velocities in arid environments and usage of high frequency sources to collect seismic data. Hence, it is expensive to define a model, with enough resolution to achieve at least 8 points per wavelength resolution, in these conditions. This often requires the models to be very large, with the need of significant computational resources. This is especially true for full 3D models where the required computational cost grows proportional to the size of the model cubed.

Recent advances in high-performance computing and a significant reduction in their cost have allowed us to conduct this type of research. However, near-surface low-velocity regions, which require a large number of grid nodes, make acoustic wave modeling an extremely computationally challenging problem. Conventional seismic simulations either ignore the relatively thin low-velocity regions or include them using a uniform grid size that is determined by the lowest velocity. The first simulation produces inaccurate results which causes the simulated data to underpredict the true data. The second simulation results in oversampling the deeper regions with higher velocity inevitably leading to a considerable increase of computational time and memory. In Chapter 4, we develop a discontinuous mesh (DM) method that uses different mesh discretizations for shallow and deep regions. This allows the acoustic wave simulations, with realistic 3D heterogeneous velocity models, to be pushed to higher frequencies to meet the requirements of gas and oil exploration in arid environments.

Chapter 2

Analytical and numerical analysis of the acoustic wave equation in LF domain

2.1 Governing equations

In acoustic seismic modeling, the objective is to describe the propagation of waves through the earth. Here, we consider wave propagation that is solved in the LF Domain. We start by discretizing the three-dimensional wave equation on a Cartesian grid $\boldsymbol{x}_{i,j} = (ih, jh, kh)$ in space, where $h > 0$ is the grid size. The solution to the forward problem is employed using a single frequency for 3D acoustic wave simulation (Hustedt et al., 2004). It is reduced from the 3D elastic wave field simulator developed by Petrov and Newman (2012).

We consider the first-order hyperbolic system in a velocity-pressure formulation in the LF domain. Let the 3D isotropic acoustic medium with density ρ and incompressibility κ ($\kappa = \rho \cdot {V_p}^2$) occupy the region Ω. The equations of motion inside Ω are given by:

$$\begin{aligned} s\rho v_x(x,y,z,s) &= \partial_x P(x,y,z,s), \\ s\rho v_y(x,y,z,s) &= \partial_y P(x,y,z,s), \\ s\rho v_z(x,y,z,s) &= \partial_z P(x,y,z,s), \\ sP(x,y,z,s) &= \kappa\left[\partial_x v_x(x,y,z,s) + \partial_y v_y(x,y,z,s) + \partial_z v_z(x,y,z,s)\right] + sm(x,y,z,s), \end{aligned} \tag{2.1}$$

where s is the complex number given by $\sigma + i\omega$, σ is the Laplace damping factor, $\omega = 2\pi$f is the angular frequency, and $i = \sqrt{-1}$. The velocities v_x, v_y and v_z are the velocity wavefield components, P is the acoustic pressure, m is seismic moment density tensor, and the symbols ∂_x, ∂_y, and ∂_z denote the partial differential operators $\frac{\partial}{\partial x}$, $\frac{\partial}{\partial y}$, and $\frac{\partial}{\partial z}$, respectively. The LF equations of motion (equation 2.1) are obtained by transforming the time-domain system of equations using the following LF transform:

$$f(s) = \int_0^\infty f(t)e^{-st}dt, \tag{2.2}$$

where $f(t)$ includes the functions $v_x(t)$, $v_y(t)$, $v_z(t)$, and $P(t)$. The time-domain first-order hyberbolic system (Virieux, 1986) is given by:

$$\begin{aligned}
\rho\partial_t v_x(x,y,z,t) &= \partial_x P(x,y,z,t),\\
\rho\partial_t v_y(x,y,z,t) &= \partial_y P(x,y,z,t),\\
\rho\partial_t v_z(x,y,z,t) &= \partial_z P(x,y,z,t),\\
\partial_t P(x,y,z,t) &= \kappa\left[\partial_x v_x(x,y,z,t) + \partial_y v_y(x,y,z,t) + \partial_z v_z(x,y,z,t)\right] + \partial_t m(x,y,z,t),
\end{aligned} \tag{2.3}$$

where the symbol ∂_t denotes the partial differential operator $\frac{\partial}{\partial_t}$ and t denotes time.

This system of equations must be augmented with boundary conditions. In the case of infinite media, the non-reflecting condition for wavefield components is applied at the boundaries of region Ω. We used the perfectly matched layer (PML) boundary conditions (Hastings et al., 1996; Kim and Pasciak, 2010). However, at a free-surface boundary, one needs to assume vacuum pressure and hence incorporate zero acoustic pressure at the boundary. In this chapter, we present the numerical analysis of the second- and fourth-order accurate LF domain velocity-pressure staggered FD scheme to simulate acoustic wave propagation using a uniform grid in the inner media.

2.2 Analytical solution of the acoustic wave equation in a homogeneous medium

We start by differentiating the first three equations in the first-order hyberbolic system (equation 2.3) with respect to space and the fourth equation is differentiated with respect to time, leading to the second-order system:

$$\begin{aligned}
\partial_x\partial_t v_x(x,y,z,t) &= \frac{1}{\rho}\partial_{xx} P(x,y,z,t),\\
\partial_y\partial_t v_y(x,y,z,t) &= \frac{1}{\rho}\partial_{yy} P(x,y,z,t),\\
\partial_z\partial_t v_z(x,y,z,t) &= \frac{1}{\rho}\partial_{zz} P(x,y,z,t),\\
\partial_{tt} P(x,y,z,t) &= \kappa\left[\partial_x\partial_t v_x(x,y,z,t) + \partial_y\partial_t v_y(x,y,z,t) + \partial_z\partial_t v_z(x,y,z,t)\right]\\
&\quad + \partial_{tt} m(x,y,z,t),
\end{aligned} \tag{2.4}$$

where the symbols ∂_{xx}, ∂_{yy}, ∂_{zz}, and ∂_{tt} denote the partial differential operators $\frac{\partial^2}{\partial x^2}$, $\frac{\partial^2}{\partial y^2}$, $\frac{\partial^2}{\partial z^2}$, and $\frac{\partial^2}{\partial t^2}$, respectively. By combining the time-domain second-order hyberbolic system (equation 2.4) into one equation, we get the following second-order inhomogeneous acoustic time-domain wave equation:

$$\nabla^2 P(x,y,z,t) - V_p^{-2}\partial_{tt} P(x,y,z,t) = -V_p^{-2}\partial_{tt} m(x,y,z,t) \tag{2.5}$$

Since the coefficients to the differential operators in equation 2.5 are independent of time, the dimension of the wave equation can be reduced to three by use of the LF transform (equation 2.2), leading to the LF wave equation, or *Helmholtz equation*,

$$(\nabla^2 + k^2)P(\mathbf{r}, s) = k^2 m(\mathbf{r}, s), \tag{2.6}$$

where $\mathbf{r} = (x, y, z)$ and k is the homogeneous medium wavenumber at LF frequency s:

$$k = i\frac{s}{V_p}. \tag{2.7}$$

Point source in unbounded medium

In a homogeneous medium, the Helmholtz equation (equation 2.6) is easily solved, with a choice of coordinate system being imposed by the source and boundary geometry. In the case of an omni-directional point source, the field only depends on the range from the source, and the solution is conveniently described in a *spherical coordinate system*. The Laplace operator in the *Cartesian coordinate system* $\mathbf{r} = (x, y, z)$ is given by:

$$\nabla^2 = \partial_{xx} + \partial_{yy} + \partial_{zz}, \tag{2.8}$$

and it is equivalent to the Laplacian in the *spherical coordinate system* $\mathbf{r} = (r, \theta, \phi)$ that is given by:

$$\nabla^2 = \frac{1}{r^2}\partial_r r^2 \partial_r + \frac{1}{r^2 \sin^2\phi}\partial_{\phi\phi} + \frac{1}{r^2 \sin\phi}\partial_\phi \sin\phi \partial_\theta. \tag{2.9}$$

Since the omni-directional source changes only with r, the Helmholtz equation can be reduced to:

$$\left[\frac{1}{r^2}\partial_r r^2 \partial_r + k^2\right] P(r, s) = 0, \tag{2.10}$$

and hence the general solution to the point source Helmholtz equation is:

$$P(r, s) = \begin{cases} \frac{A}{r}e^{ikr} \\ \frac{B}{r}e^{-ikr} \end{cases}. \tag{2.11}$$

The solution to the Helmholtz equation is a linear combination of the two independent solutions in equation 2.11, but since we assume the sphere is the only source in the infinite medium, we can apply the *radiation condition* of no incoming waves at infinity to require that $B = 0$, i.e.:

$$P(r, s) = A\frac{e^{ikr}}{r}. \tag{2.12}$$

Defining the *source strength* $S(s) = -4\pi A$ as the volume-injection amplitude produced by the source at LF frequency s, we then obtain the solution from equation 2.12 for the acoustic pressure:

$$P(r, s) = -S(s)\frac{e^{ikr}}{4\pi r}. \tag{2.13}$$

The fraction in equation 2.13 is called the *Green's function*. For a source at $\mathbf{r} = \mathbf{r_0}$, it is given by:

$$g_s(\mathbf{r}, \mathbf{r_0}) = \frac{e^{ikR}}{4\pi R}, \quad R = |\mathbf{r} - \mathbf{r_0}|. \tag{2.14}$$

The Green's function satisfies the inhomogeneous Helmholtz equation:

$$(\nabla^2 + k^2) g_s(\mathbf{r}, \mathbf{r_0}) = -\delta(\mathbf{r} - \mathbf{r_0}), \tag{2.15}$$

which is easily verified by integrating equation 2.15 over a small volume containg the source point at $\mathbf{r_0}$. By multiplying equation 2.15 by $-S(s)$, we get the inhomogeneous Helmholtz equation for a simple point source of strength $S(s)$ at point $\mathbf{r}_0$:

$$(\nabla^2 + k^2) P(r, s) = S(s)\delta(\mathbf{r} - \mathbf{r_0}). \tag{2.16}$$

Furthermore, the Green's function of the time-domain wave equation is obtained by the inverse LF transform of g_s:

$$g_t(\mathbf{r}, \mathbf{r_0}) = \frac{\delta(t - R/V_p)}{4\pi R} \tag{2.17}$$

and can be thought of as the impulse response in an unbounded medium.

Point source in fluid half-space

As an example of the use of Green's function to boundary value problems, we apply it to the simplest possible example of a bounded acoustic medium, which is the halfspace shown in Figure 2.1. The upper halfspace is assumed to be a vacuum, and the boundary condition to be satisfied by the field in the fluid is that the pressure must vanish at the free-surface ($z = 0$). In Figure 2.1, we introduce a Cartesian coordinate system with the origin on the surface and with the z-axis perpendicular to the surface. A simple point source is assumed to be placed at $\mathbf{r}_s = (x_s, y_s, z_s)$.

The pressure-release at the free-surface boundary is given by:

$$P(\mathbf{r_B}, s) = 0, \quad \mathbf{r_B} = (x, y, 0). \tag{2.18}$$

Hence, for this simple case, it is straightforward to choose a Green's function which vanishes on the free-surface $z = 0$:

$$g_s(\mathbf{r}, \mathbf{r_B}) = \frac{e^{ikR}}{4\pi R} - \frac{e^{ikR'}}{4\pi R'} \tag{2.19}$$

with

$$\begin{aligned} R &= \sqrt{(x - x_s)^2 + (y - y_s)^2 + (z - z_s)^2}, \\ R' &= \sqrt{(x - x_s)^2 + (y - y_s)^2 + (z + z_s)^2}. \end{aligned} \tag{2.20}$$

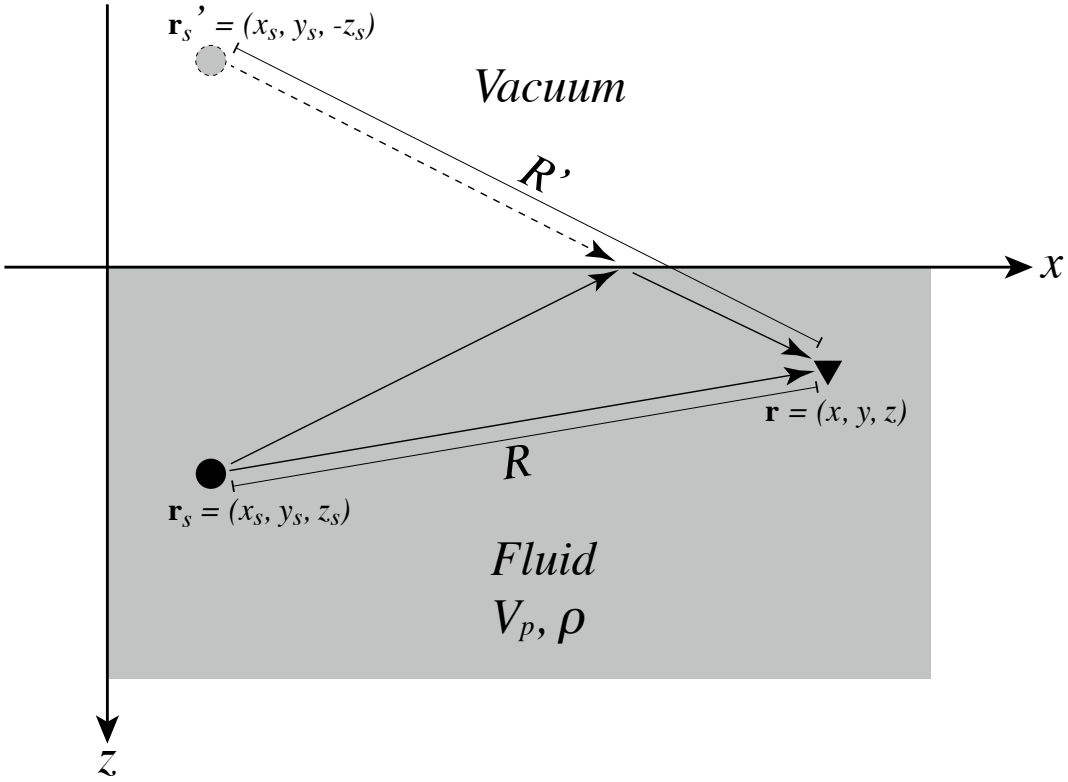

Figure 2.1: Point source in a fluid halfspace illustrating the method of images.

The solution for the pressure now takes the form:

$$P(r,s) = -S(s)\left[\frac{e^{ikR}}{4\pi R} - \frac{e^{ikR'}}{4\pi R'}\right], \tag{2.21}$$

which corresponds to the superposition of the free-space solutions for the source at depth $z = z_s$ and an image source at $z = -z_s$ in the vacuum halfspace. The solution is identical to the *mirror* or *image method* found in electrostatics boundary-value problems (Griffiths, 2005; Jackson, 2007).

2.3 Second-order accurate FD discretization of the acoustic wave equation

The layout of the three velocity components and acoustic pressure is shown in Figure 2.2, indicating the most basic way to use a velociy-pressure staggered-grid. We discretize equa-

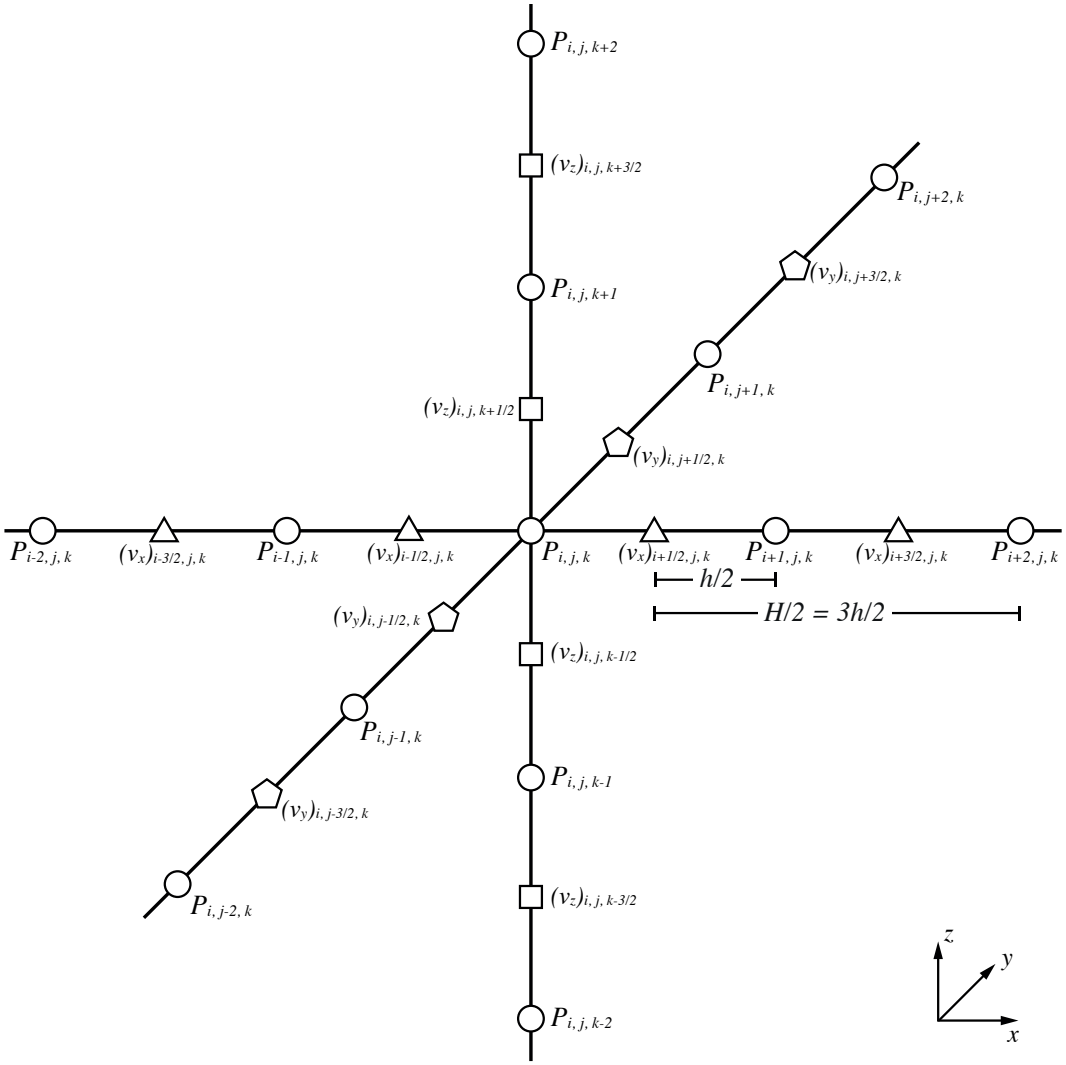

Figure 2.2: Layout of pressure and velocity components for staggered-grid acoustic wave propagation FD method. Updating $(v_x)_{i+1/2,j,k}$ requires $P_{i,j,k}$, and $P_{i+1,j,k}$ for second-order FD and $P_{i-1,j,k}$, $P_{i,j,k}$, $P_{i+1,j,k}$, $P_{i+2,j,k}$ for fourth-order FD approximation.

tion 2.1 using the second-order accurate central FD formula in Appendix A.1 to get:

$$\begin{aligned} s\rho_{i+\frac{1}{2},j,k} v_x|_{i+\frac{1}{2},j,k} &= \frac{P_{i+1,j,k} - P_{i,j,k}}{h}, \\ s\rho_{i,j+\frac{1}{2},k} v_y|_{i,j+\frac{1}{2},k} &= \frac{P_{i,j+1,k} - P_{i,j,k}}{h}, \\ s\rho_{i,j,k+\frac{1}{2}} v_z|_{i,j,k+\frac{1}{2}} &= \frac{P_{i,j,k+1} - P_{i,j,k}}{h}, \end{aligned} \tag{2.22}$$

and

$$sP_{i,j,k} = \frac{\kappa_{i,j,k}}{h}\left[v_x|_{i+\frac{1}{2},j,k} - v_x|_{i-\frac{1}{2},j,k} + v_y|_{i,j+\frac{1}{2},k} - v_y|_{i,j-\frac{1}{2},k} + v_z|_{i,j,k+\frac{1}{2}} - v_z|_{i,j,k-\frac{1}{2}}\right]. \tag{2.23}$$

We then substitute equations 2.22 into equation 2.23 and get the following relationship for acoustic pressure:

$$\begin{aligned} P_{i,j,k} = \frac{\kappa_{i,j,k}}{h^2 s^2}\Bigg[& \frac{1}{\rho_{i-\frac{1}{2},j,k}} P_{i-1,j,k} + \frac{1}{\rho_{i,j-\frac{1}{2},k}} P_{i,j-1,k} + \frac{1}{\rho_{i,j,k-\frac{1}{2}}} P_{i,j,k-1} \\ & - \left(\frac{1}{\rho_{i+\frac{1}{2},j,k}} + \frac{1}{\rho_{i-\frac{1}{2},j,k}} + \frac{1}{\rho_{i,j+\frac{1}{2},k}} + \frac{1}{\rho_{i,j-\frac{1}{2},k}} + \frac{1}{\rho_{i,j,k+\frac{1}{2}}} + \frac{1}{\rho_{i,j,k-\frac{1}{2}}}\right) P_{i,j,k} \\ & + \frac{1}{\rho_{i+\frac{1}{2},j,k}} P_{i+1,j,k} + \frac{1}{\rho_{i,j+\frac{1}{2},k}} P_{i,j+1,k} + \frac{1}{\rho_{i,j,k+\frac{1}{2}}} P_{i,j,k+1}\Bigg]. \end{aligned} \tag{2.24}$$

Using equation 2.24, we can generate the mass matrix A for the second-order accurate FD LF domain acoustic wave equation with a size of $N_x \times N_y \times N_z$ and solve the system as:

$$AP = m. \tag{2.25}$$

Internal row $[i + jN_x + kN_xN_y]$ for the mass matrix A, with the first row starting at zero ($i = 0$, $j = 0$, $k = 0$), is approximated by:

$$\begin{aligned} A_{i+jN_x+kN_xN_y,\, i+jN_x+(k-1)N_xN_y} &= -\frac{a}{\rho_{i,j,k-\frac{1}{2}}}, \\ A_{i+jN_x+kN_xN_y,\, i+(j-1)N_x+kN_xN_y} &= -\frac{a}{\rho_{i,j-\frac{1}{2},k}}, \\ A_{i+jN_x+kN_xN_y,\, (i-1)+jN_x+kN_xN_y} &= -\frac{a}{\rho_{i-\frac{1}{2},j,k}}, \\ A_{i+jN_x+kN_xN_y,\, i+jN_x+kN_xN_y} &= 1 + b_{2^{nd}} \cdot a, \\ A_{i+jN_x+kN_xN_y,\, (i+1)+jN_x+kN_xN_y} &= -\frac{a}{\rho_{i+\frac{1}{2},j,k}}, \\ A_{i+jN_x+kN_xN_y,\, i+(j+1)N_x+kN_xN_y} &= -\frac{a}{\rho_{i,j+\frac{1}{2},k}}, \\ A_{i+jN_x+kN_xN_y,\, i+jN_x+(k+1)N_xN_y} &= -\frac{a}{\rho_{i,j,k+\frac{1}{2}}}, \end{aligned} \tag{2.26}$$

where:

$$\begin{aligned} a &= \frac{\kappa_{i,j,k}}{h^2 s^2}, \\ b_{2^{nd}} &= \left(\frac{1}{\rho_{i+\frac{1}{2},j,k}} + \frac{1}{\rho_{i-\frac{1}{2},j,k}} + \frac{1}{\rho_{i,j+\frac{1}{2},k}} + \frac{1}{\rho_{i,j-\frac{1}{2},k}} + \frac{1}{\rho_{i,j,k+\frac{1}{2}}} + \frac{1}{\rho_{i,j,k-\frac{1}{2}}} \right). \end{aligned} \tag{2.27}$$

2.4 Fourth-order accurate FD discretization of the acoustic wave equation

We start by discretizing equation 2.1 using the fourth-order accurate central FD formula in Appendix A.2 to get:

$$\begin{aligned} s\rho_{i+\frac{1}{2},j,k} v_x|_{i+\frac{1}{2},j,k} &= \frac{-P_{i+2,j,k} + 27P_{i+1,j,k} - 27P_{i,j,k} + P_{i-1,j,k}}{24h}, \\ s\rho_{i,j+\frac{1}{2},k} v_y|_{i,j+\frac{1}{2},k} &= \frac{-P_{i,j+2,k} + 27P_{i,j+1,k} - 27P_{i,j,k} + P_{i,j-1,k}}{24h}, \\ s\rho_{i,j,k+\frac{1}{2}} v_z|_{i,j,k+\frac{1}{2}} &= \frac{-P_{i,j,k+2} + 27P_{i,j,k+1} - 27P_{i,j,k} + P_{i,j,k-1}}{24h}, \end{aligned} \tag{2.28}$$

and

$$\begin{aligned} sP_{i,j,k} = \frac{\kappa_{i,j,k}}{24h} \Big[&\left(-v_x|_{i+\frac{3}{2},j,k} + 27v_x|_{i+\frac{1}{2},j,k} - 27v_x|_{i-\frac{1}{2},j,k} - v_x|_{i-\frac{3}{2},j,k} \right) \\ &+ \left(-v_y|_{i,j+\frac{3}{2},k} + 27v_y|_{i,j+\frac{1}{2},k} - 27v_y|_{i,j-\frac{1}{2},k} - v_y|_{i,j-\frac{3}{2},k} \right) \\ &+ \left(-v_z|_{i,j,k+\frac{3}{2}} + 27v_z|_{i,j,k+\frac{1}{2}} - 27v_z|_{i,j,k-\frac{1}{2}} - v_z|_{i,j,k-\frac{3}{2}} \right) \Big]. \end{aligned} \tag{2.29}$$

We substitute equations 2.28 into equation 2.29 to get the following relationship for acoustic pressure:

$$
\begin{aligned}
P_{i,j,k} = \frac{\kappa_{i,j,k}}{h^2 s^2} \Bigg[& \left(\frac{1}{\rho_{i-\frac{3}{2},j,k}} \right) P_{i-3,j,k} + \left(\frac{-27}{\rho_{i-\frac{3}{2},j,k}} + \frac{-27}{\rho_{i-\frac{1}{2},j,k}} \right) P_{i-2,j,k} \\
& + \left(\frac{27}{\rho_{i-\frac{3}{2},j,k}} + \frac{729}{\rho_{i-\frac{1}{2},j,k}} + \frac{27}{\rho_{i+\frac{1}{2},j,k}} \right) P_{i-1,j,k} \\
& + \left(\frac{-1}{\rho_{i-\frac{3}{2},j,k}} + \frac{-729}{\rho_{i-\frac{1}{2},j,k}} + \frac{-729}{\rho_{i+\frac{1}{2},j,k}} + \frac{-1}{\rho_{i+\frac{3}{2},j,k}} \right) P_{i,j,k} \\
& + \left(\frac{27}{\rho_{i-\frac{1}{2},j,k}} + \frac{729}{\rho_{i+\frac{1}{2},j,k}} + \frac{27}{\rho_{i+\frac{3}{2},j,k}} \right) P_{i+1,j,k} \\
& + \left(\frac{-27}{\rho_{i+\frac{1}{2},j,k}} + \frac{-27}{\rho_{i+\frac{3}{2},j,k}} \right) P_{i+2,j,k} + \left(\frac{1}{\rho_{i+\frac{3}{2},j,k}} \right) P_{i+3,j,k} \\
& + \left(\frac{1}{\rho_{i,j-\frac{3}{2},k}} \right) P_{i,j-3,k} + \left(\frac{-27}{\rho_{i,j-\frac{3}{2},k}} + \frac{-27}{\rho_{i,j-\frac{1}{2},k}} \right) P_{i,j-2,k} \\
& + \left(\frac{27}{\rho_{i,j-\frac{3}{2},k}} + \frac{729}{\rho_{i,j-\frac{1}{2},k}} + \frac{27}{\rho_{i,j+\frac{1}{2},k}} \right) P_{i,j-1,k} \\
& + \left(\frac{-1}{\rho_{i,j-\frac{3}{2},k}} + \frac{-729}{\rho_{i,j-\frac{1}{2},k}} + \frac{-729}{\rho_{i,j+\frac{1}{2},k}} + \frac{-1}{\rho_{i,j+\frac{3}{2},k}} \right) P_{i,j,k} \\
& + \left(\frac{27}{\rho_{i,j-\frac{1}{2},k}} + \frac{729}{\rho_{i,j+\frac{1}{2},k}} + \frac{27}{\rho_{i,j+\frac{3}{2},k}} \right) P_{i,j+1,k} \\
& + \left(\frac{-27}{\rho_{i,j+\frac{1}{2},k}} + \frac{-27}{\rho_{i,j+\frac{3}{2},k}} \right) P_{i,j+2,k} + \left(\frac{1}{\rho_{i,j+\frac{3}{2},k}} \right) P_{i,j+3,k} \\
& + \left(\frac{1}{\rho_{i,j,k-\frac{3}{2}}} \right) P_{i,j,k-3} + \left(\frac{-27}{\rho_{i,j,k-\frac{3}{2}}} + \frac{-27}{\rho_{i,j,k-\frac{1}{2}}} \right) P_{i,j,k-2} \\
& + \left(\frac{27}{\rho_{i,j,k-\frac{3}{2}}} + \frac{729}{\rho_{i,j,k-\frac{1}{2}}} + \frac{27}{\rho_{i,j,k+\frac{1}{2}}} \right) P_{i,j,k-1} \\
& + \left(\frac{-1}{\rho_{i,j,k-\frac{3}{2}}} + \frac{-729}{\rho_{i,j,k-\frac{1}{2}}} + \frac{-729}{\rho_{i,j,k+\frac{1}{2}}} + \frac{-1}{\rho_{i,j,k+\frac{3}{2}}} \right) P_{i,j,k} \\
& + \left(\frac{27}{\rho_{i,j,k-\frac{1}{2}}} + \frac{729}{\rho_{i,j,k+\frac{1}{2}}} + \frac{27}{\rho_{i,j,k+\frac{3}{2}}} \right) P_{i,j,k+1} \\
& + \left(\frac{-27}{\rho_{i,j,k+\frac{1}{2}}} + \frac{-27}{\rho_{i,j,k+\frac{3}{2}}} \right) P_{i,j,k+2} + \left(\frac{1}{\rho_{i,j,k+\frac{3}{2}}} \right) P_{i,j,k+3} \Bigg] .
\end{aligned}
\tag{2.30}
$$

Using equation 2.30, we generate the mass matrix A for the fourth-order accurate FD LF domain acoustic wave equation with a size of $N_x \times N_y \times N_z$ and solve the linear system for pressure P as in equation 2.25. Internal row $[i + jN_x + kN_xN_y]$ for the fourth-order mass

matrix A, with the first row starting at zero ($i = 0$, $j = 0$, $k = 0$), is approximated by:

$$
\begin{aligned}
A_{i+jN_x+kN_xN_y,\,i+jN_x+(k-3)N_xN_y} &= -\frac{a}{\rho_{i,j,k-\frac{3}{2}}},\\
A_{i+jN_x+kN_xN_y,\,i+jN_x+(k-2)N_xN_y} &= -a\left(\frac{-27}{\rho_{i,j,k-\frac{3}{2}}}+\frac{-27}{\rho_{i,j,k-\frac{1}{2}}}\right),\\
A_{i+jN_x+kN_xN_y,\,i+jN_x+(k-1)N_xN_y} &= -a\left(\frac{27}{\rho_{i,j,k-\frac{3}{2}}}+\frac{729}{\rho_{i,j,k-\frac{1}{2}}}+\frac{27}{\rho_{i,j,k+\frac{1}{2}}}\right),\\
A_{i+jN_x+kN_xN_y,\,i+(j-3)N_x+kN_xN_y} &= -\frac{a}{\rho_{i,j-\frac{3}{2},k}},\\
A_{i+jN_x+kN_xN_y,\,i+(j-2)N_x+kN_xN_y} &= -a\left(\frac{-27}{\rho_{i,j-\frac{3}{2},k}}+\frac{-27}{\rho_{i,j-\frac{1}{2},k}}\right),\\
A_{i+jN_x+kN_xN_y,\,i+(j-1)N_x+kN_xN_y} &= -a\left(\frac{27}{\rho_{i,j-\frac{3}{2},k}}+\frac{729}{\rho_{i,j-\frac{1}{2},k}}+\frac{27}{\rho_{i,j+\frac{1}{2},k}}\right),\\
A_{i+jN_x+kN_xN_y,\,(i-3)+jN_x+kN_xN_y} &= -\frac{a}{\rho_{i-\frac{3}{2},j,k}},\\
A_{i+jN_x+kN_xN_y,\,(i-2)+jN_x+kN_xN_y} &= -a\left(\frac{-27}{\rho_{i-\frac{3}{2},j,k}}+\frac{-27}{\rho_{i-\frac{1}{2},j,k}}\right),\\
A_{i+jN_x+kN_xN_y,\,(i-1)+jN_x+kN_xN_y} &= -a\left(\frac{27}{\rho_{i-\frac{3}{2},j,k}}+\frac{729}{\rho_{i-\frac{1}{2},j,k}}+\frac{27}{\rho_{i+\frac{1}{2},j,k}}\right),\\
A_{i+jN_x+kN_xN_y,\,i+jN_x+kN_xN_y} &= 1+b_{4^{th}}\cdot a,\\
A_{i+jN_x+kN_xN_y,\,(i+1)+jN_x+kN_xN_y} &= -a\left(\frac{27}{\rho_{i-\frac{1}{2},j,k}}+\frac{729}{\rho_{i+\frac{1}{2},j,k}}+\frac{27}{\rho_{i+\frac{3}{2},j,k}}\right),\\
A_{i+jN_x+kN_xN_y,\,(i+2)+jN_x+kN_xN_y} &= -a\left(\frac{-27}{\rho_{i+\frac{1}{2},j,k}}+\frac{-27}{\rho_{i+\frac{3}{2},j,k}}\right),\\
A_{i+jN_x+kN_xN_y,\,(i+3)+jN_x+kN_xN_y} &= -\frac{a}{\rho_{i+\frac{3}{2},j,k}},\\
A_{i+jN_x+kN_xN_y,\,i+(j+1)N_x+kN_xN_y} &= -a\left(\frac{27}{\rho_{i,j-\frac{1}{2},k}}+\frac{729}{\rho_{i,j+\frac{1}{2},k}}+\frac{27}{\rho_{i,j+\frac{3}{2},k}}\right),\\
A_{i+jN_x+kN_xN_y,\,i+(j+2)N_x+kN_xN_y} &= -a\left(\frac{-27}{\rho_{i,j+\frac{1}{2},k}}+\frac{-27}{\rho_{i,j+\frac{3}{2},k}}\right),\\
A_{i+jN_x+kN_xN_y,\,i+(j+3)N_x+kN_xN_y} &= -\frac{a}{\rho_{i,j+\frac{3}{2},k}},\\
A_{i+jN_x+kN_xN_y,\,i+jN_x+(k+1)N_xN_y} &= -a\left(\frac{27}{\rho_{i,j,k-\frac{1}{2}}}+\frac{729}{\rho_{i,j,k+\frac{1}{2}}}+\frac{27}{\rho_{i,j,k+\frac{3}{2}}}\right),\\
A_{i+jN_x+kN_xN_y,\,i+jN_x+(k+2)N_xN_y} &= -a\left(\frac{-27}{\rho_{i,j,k+\frac{1}{2}}}+\frac{-27}{\rho_{i,j,k+\frac{3}{2}}}\right),\\
A_{i+jN_x+kN_xN_y,\,i+jN_x+(k+3)N_xN_y} &= -\frac{a}{\rho_{i,j,k+\frac{3}{2}}},
\end{aligned}
\tag{2.31}
$$

where:

$$
\begin{aligned}
a &= \frac{\kappa_{i,j,k}}{h^2 s^2}, \\
b_{4^{th}} &= \left(\frac{1}{\rho_{i-\frac{3}{2},j,k}} + \frac{729}{\rho_{i-\frac{1}{2},j,k}} + \frac{729}{\rho_{i+\frac{1}{2},j,k}} + \frac{1}{\rho_{i+\frac{3}{2},j,k}} \right. \\
&+ \frac{1}{\rho_{i,j-\frac{3}{2},k}} + \frac{729}{\rho_{i,j-\frac{1}{2},k}} + \frac{729}{\rho_{i,j+\frac{1}{2},k}} + \frac{1}{\rho_{i,j+\frac{3}{2},k}} \\
&\left. + \frac{1}{\rho_{i,j,k-\frac{3}{2}}} + \frac{729}{\rho_{i,j,k-\frac{1}{2}}} + \frac{729}{\rho_{i,j,k+\frac{1}{2}}} + \frac{1}{\rho_{i,j,k+\frac{3}{2}}} \right).
\end{aligned}
\tag{2.32}
$$

2.5 Numerical solutions of the acoustic wave equation in a homogeneous medium

We perform two simulations to test both second- and fourth-order numerical analysis schemes. The first simulation is done by solving the acoustic wave equation in an unbounded homogeneous media and the second simulation is done by solving it in a homogeneous half-space. For both simulations, we use a point-source Ricker wavelet with frequency 10 Hz and damping $1\frac{1}{s}$. The homogenous medium's constant velocity and density are 4500 m/s and 2000 kg/m^3, respectively. By implementing these design choices in addition to a 20 m grid-spacing, we ensure having at least 8 points per wavelength according to the following relationship (Petersson and Sjogreen, 2014):

$$
\text{PPW} = \frac{\min V_p}{2.5 \cdot \text{f} \cdot h}, \tag{2.33}
$$

where PPW is the number of points per wavelength, f is the regular frequency, and h is the grid-spacing. To measure the accuracy, we compare the numerical results with the analytical solution by measuring the relative error between the two solutions.

Point source in unbounded medium simulation

For the FD solution of the point-source in unbounded medium simulation, we have PML in all boundaries to represent the infinite media condition. We place the Ricker wavelet point-source 500 m away from the left boundary. The receivers are placed parallel to the source and measure the acoustic pressure P. The acquisition design is depicted in Figure 2.3.

We plot the real and imaginary results of the numerical second- and fourth-order FD simulations with the analytical solution (Figure 2.4). The analytical and numerical solutions are nearly identical to the naked eye in both the real and imaginary parts for second- and fourth-order FD solutions. In Figure 2.5, we show that the numerical simulations have less than 5% average error relative to the true analytical solution.

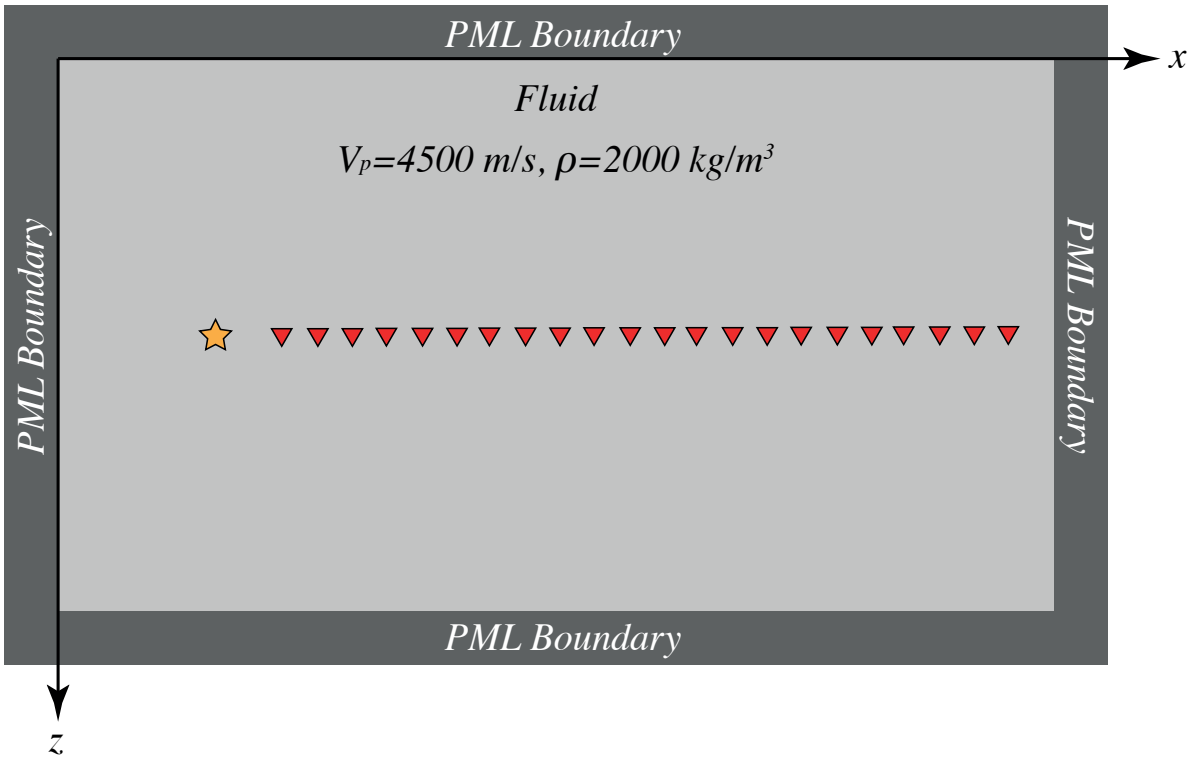

Figure 2.3: Source (*star*) and receiver locations (*inverted triangles*) for the numerical modeling of the infinite homogeneous media acoustic wave simulation.

Point source in fluid half-space simulation

In the fluid half-space simulation, we have PML in all boundaries except at the top ($z = 0$), where we insert a zero pressure boundary to represent vacuum. We place a Ricker wavelet point-source, at 500 m depth. The receivers are placed along the vertical source line at the center of the system to measure the acoustic pressure P. The situation is depicted in Figure 2.6.

We compare the real and imaginary results of the numerical second- and fourth-order FD half-space simulations with analytical solution in Figure 2.7. The analytical and numerical solutions are well correlated and show less than 5% average error (Figure 2.8).

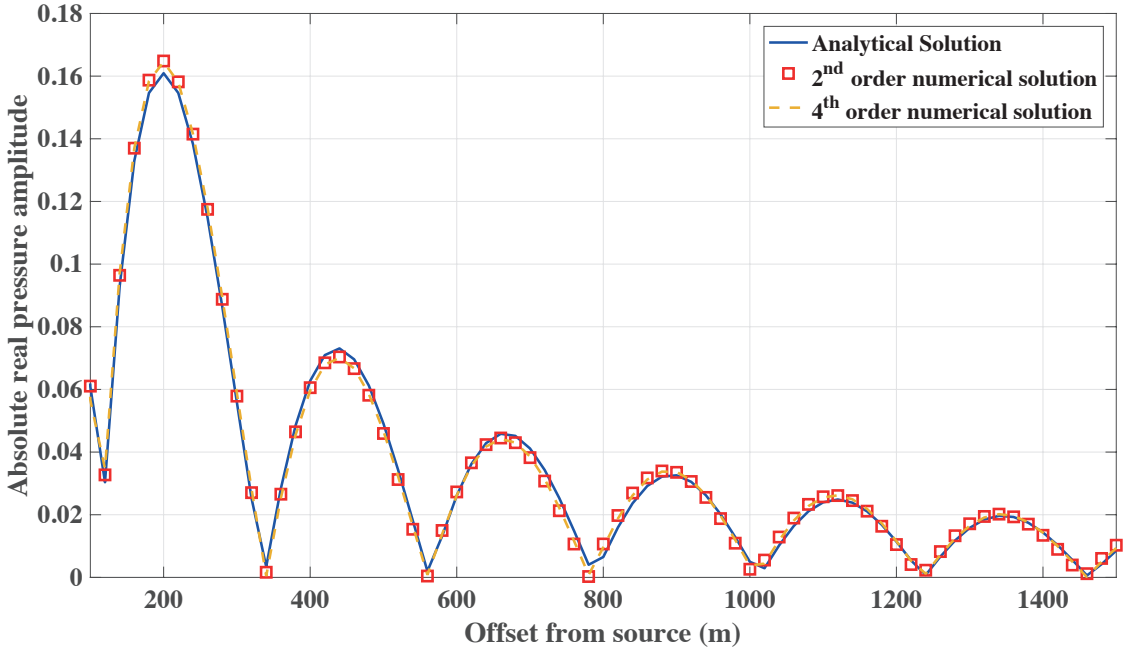

(a) Absolute real part

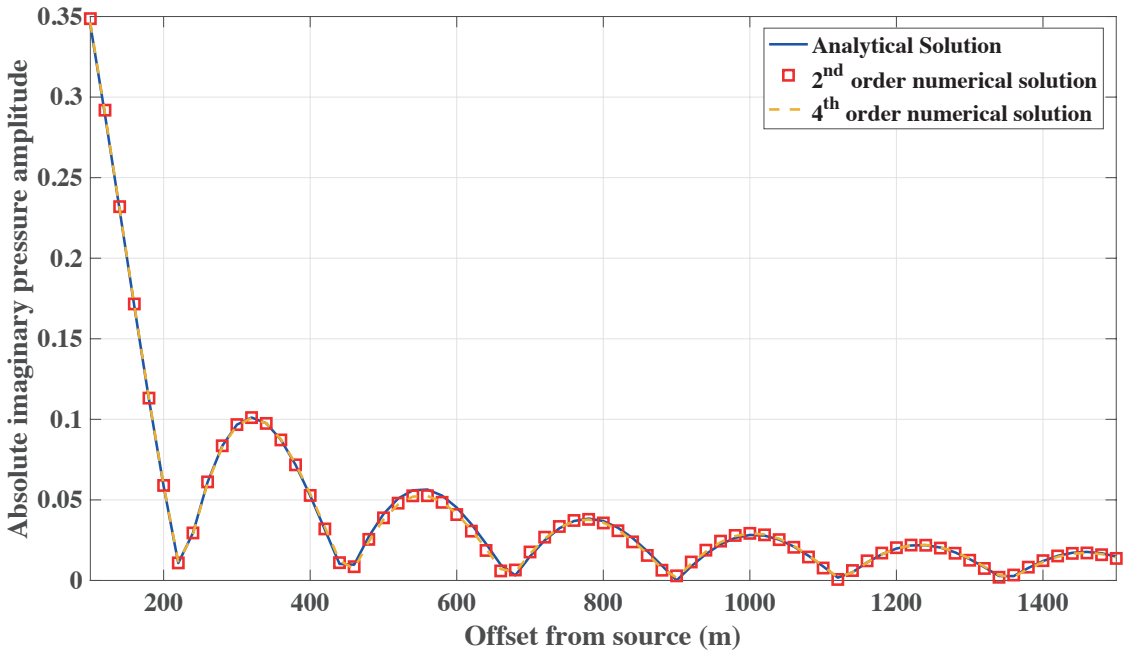

(b) Absolute imaginary part

Figure 2.4: Comparison between analytical and numerical solutions for the acoustic wave equation in an infinite homogeneous media using frequency 10 Hz and damping $1\frac{1}{s}$.

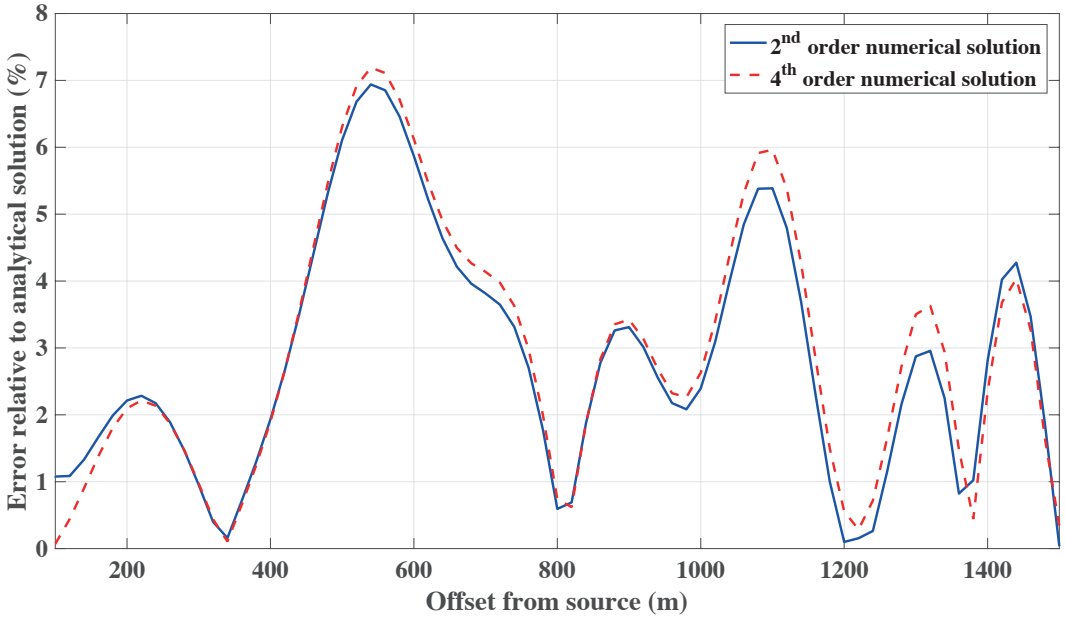

Figure 2.5: Error of numerical solutions relative to analytical solution for the acoustic wave equation in an infinite homogeneous media using frequency 10 Hz and damping $1\frac{1}{s}$.

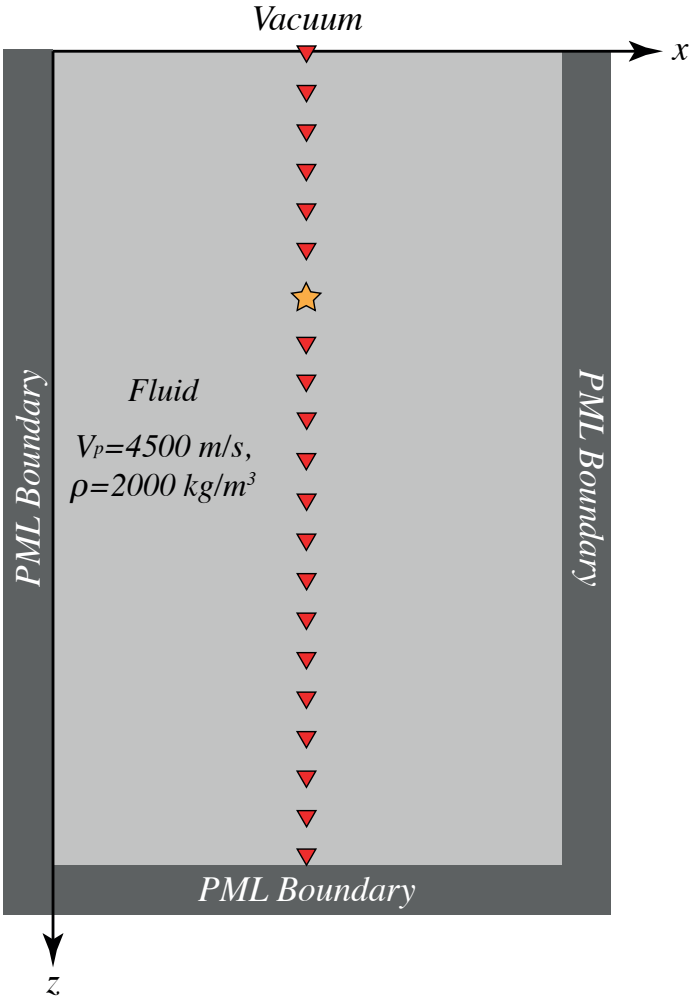

Figure 2.6: Source (*star*) and receiver locations (*inverted triangles*) for the numerical modeling of the half-space homogeneous media acoustic wave simulation.

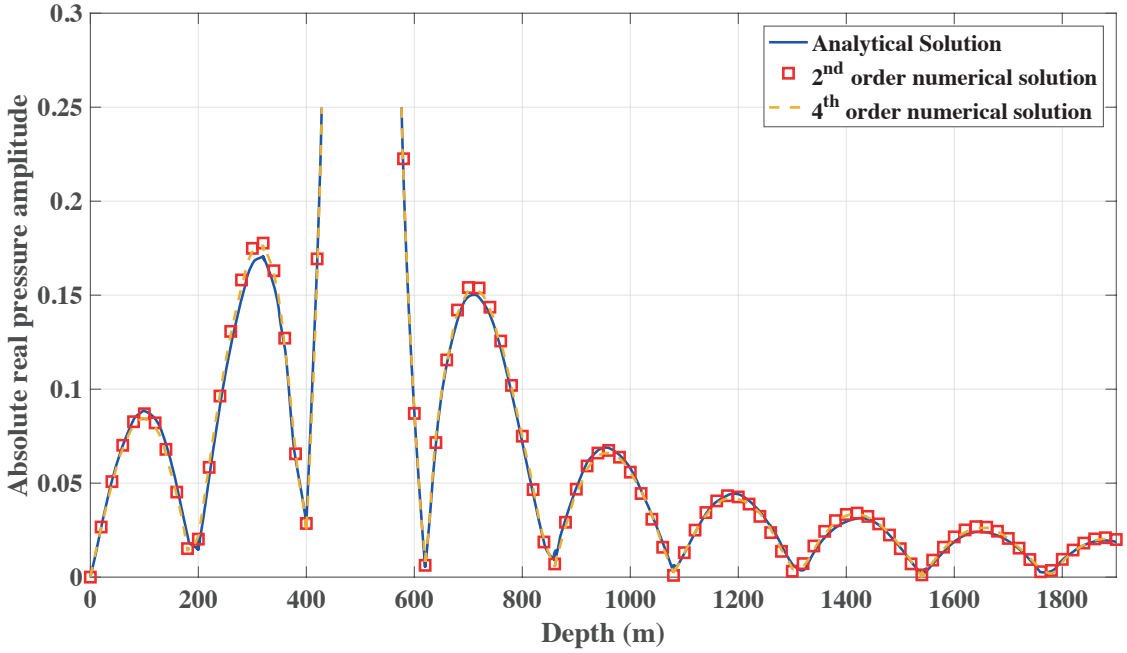

(a) Absolute real part

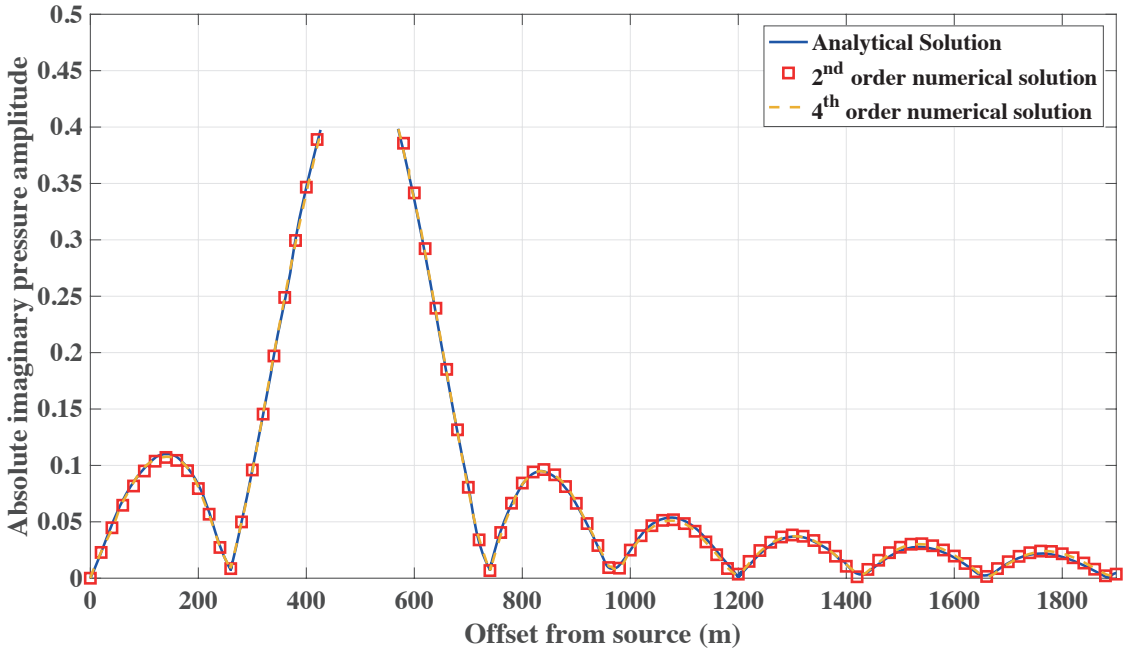

(b) Absolute imaginary part

Figure 2.7: Comparison between analytical and numerical solutions for the acoustic wave equation in an infinite homogeneous media with free-surface boundary using frequency 10 Hz and damping $1\frac{1}{s}$.

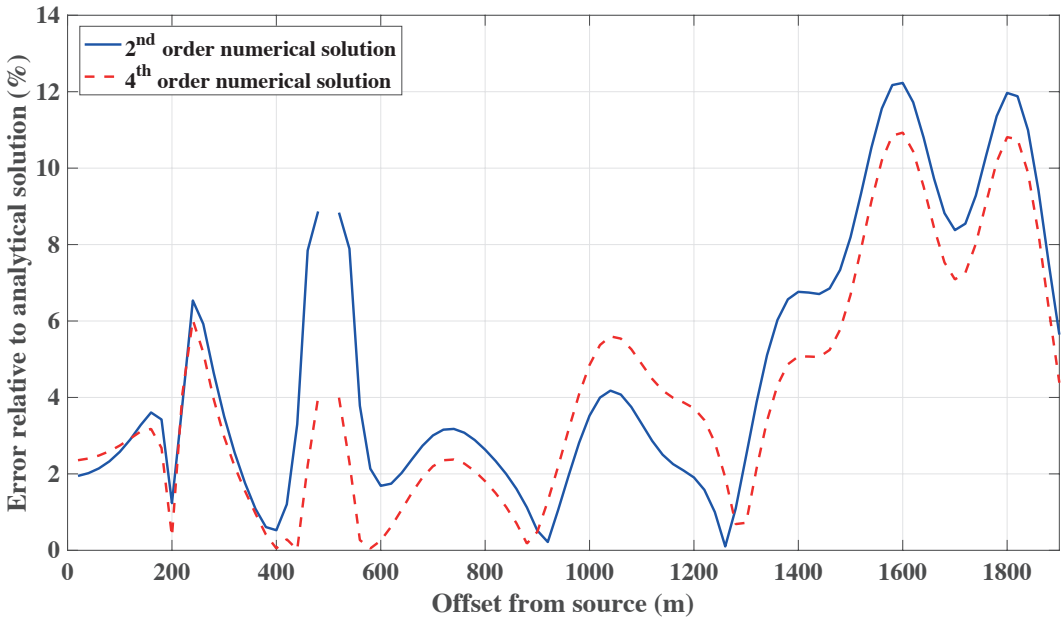

Figure 2.8: Error of numerical solutions relative to analytical solution for the acoustic wave equation in an infinite homogeneous media with free-surface boundary using frequency 10 Hz and damping $1\frac{1}{s}$.

Chapter 3

Embedded boundary methods

3.1 Introduction

A straightforward approach to the implementation of the free surface is to set the acoustic parameters at and above the free surface to zero. The method is commonly referred to as vacuum formulation or staircase method. The free-surface boundary condition is thus not treated explicitly; instead, it is assumed to be implicitly fulfilled. Staircase-method applications can be found in Zahradník and Urban (1984), Zahradník et al. (1993), and Ohminato and Chouet (1997). The method is attractive because of its trivial implementation and the possibility to model topography. Bohlen and Saenger (2006) concluded that to model topography with a staircase method, more than 60 grid points per minimum wavelength are required in a second-order scheme to obtain acceptable results.

Another solution is the curvilinear method which transforms the velocity-pressure formulation system of equations from a curved to a rectangular grid (Tessmer et al., 1992; Tessmer and Kosloff, 1994; Hestholm, 1999; Hestholm and Ruud, 2000). At the free surface, the pressure and velocities are transformed into local systems in which the vertical coordinate axis is parallel to the normal of the local surface element. The free-surface conditions are then implemented by a 'characteristic' treatment of both the velocity and pressure components, before they are rotated back to the original system. More recent studies applied the embedded-boundary condition for 2D FD solution of the wave equation with success (Kreiss and Petersson, 2006; Li et al., 2010). The studies applied the embedded-boundary method to 2D frequency- and time-domain modeling problems. They investigated quadratic interpolation when computing the pressure above the free surface.

This chapter describes an embedded-boundary method for the three-dimensional acoustic wave equation with irregular free-surface boundary on a Cartesian grid. By computing pressure on either sides of the interface, we can satisfy a zero acoustic pressure at the free surface, yielding superior results compared to conventional implementations that model topography as a staircase approximation.

At a free-surface boundary, we assume vacuum pressure by incorporating zero acoustic

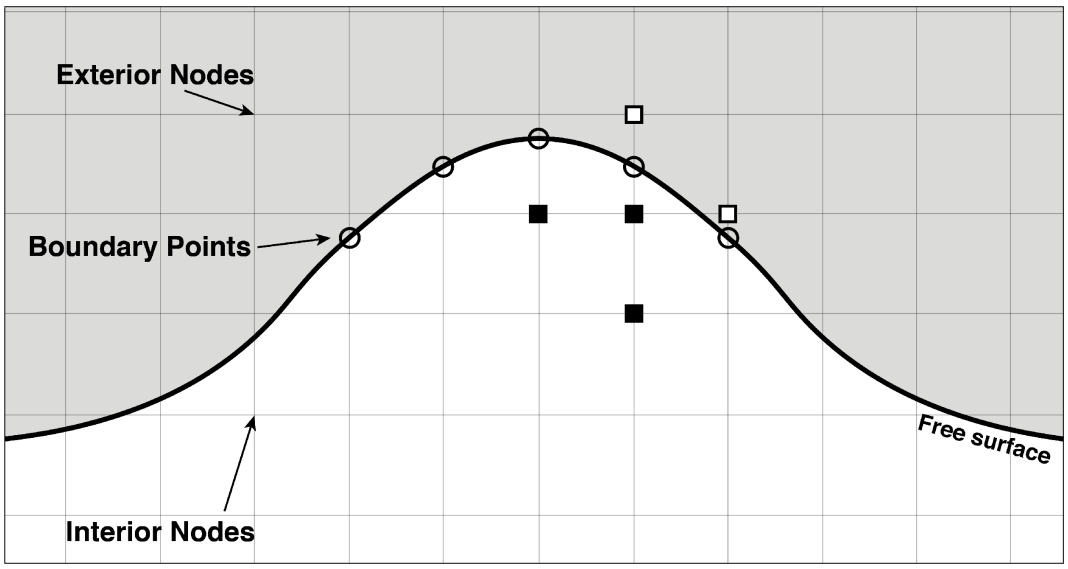

Figure 3.1: Smooth curved free surface on a uniform Cartesian grid for a second-order FD stencil. *White squares* denote ghost nodes required by the stencil. *Black squares* denote the stencil interior grid nodes. *Circles* denote points on the free-surface that are *boundary* points.

pressure P at the boundary using the following relation:

$$P = 0. \tag{3.1}$$

In simple topography settings, where the free surface is a flat plane that coincides with the top plane of the FD grid, the boundary condition may be realized without staircasing error (Graves, 1996; Gottschammer and Olsen, 2001). However, when the free surface has a more complicated geometric structure, incorporating the free-surface boundary condition becomes more challenging because the FD stencil will cross over the free surface as illustrated in Figure 3.1. In this setting, some algorithms perform adaptation of the FD grid to the free surface (Hestholm, 1999; Hestholm and Ruud, 2000; Zhang and Chen, 2006; Zhang et al., 2012a) or construct the values of the wavefield on the exterior nodes if one wishes to keep the grid intact (Lombard et al., 2008; Kreiss and Petersson, 2006; Li et al., 2010).

3.2 Methodology

We consider a case where the free surface is immersed within a regular FD grid and assume a homogeneous media around the boundary. The free surface can be defined by the equation:

$$Z_s = f(x, y). \tag{3.2}$$

We define grid nodes as *interior nodes* if they inside the domain Ω and underneath the free surface, as shown in Figure 3.1. Nodes outside the domain of interest, i.e., above the free

surface, are defined as *exterior nodes*, and points on the free-surface boundary are defined as *boundary points*. The *ghost nodes* are defined to be grid points outside the domain of interest but still being requested by stencils. For example, the second order FD scheme with seven stencil points requires only one layer of nodes above the surface (Figure 3.1).

With the above definitions, the problem of free-surface boundary treatment becomes the problem of updating the wavefield at the ghost nodes such that the wavefield at boundary points is forced to be zero according to the boundary condition in equation 3.1. Because we know the exact values of the pressure at the boundary, the boundary condition may be realized as extrapolation or interpolation of the wavefield from the interior nodes to the ghost nodes via the boundary points. This method is called the embedded boundary method (Lombard et al., 2008; Kreiss and Petersson, 2006; Li et al., 2010).

The value of the pressure at the ghost nodes may be defined by the method of images (Jackson, 2007; Griffiths, 2005):

$$P_g = -P_{g,m}. \tag{3.3}$$

For each ghost node P_g, we define a *ghost mirror* point $P_{g,m}$ inside the surface medium. For planar or spherical boundaries, the relationship ensures the boundary condition is exact (Morse and Feshbach, 2010). For an arbitrary boundary, it becomes an approximation. However, when the distance between the ghost node and the boundary is small (about one or two grid spacings), the boundary may be considered as locally planar. In this case, we can expect that equation 3.3 enforces equation 3.1 with good accuracy. Nodes above the ghost nodes that are not required by stencils are set to zero.

Ghost mirrors location

To locate the position of the ghost mirror, we find the closest distance between each ghost node at (x_g, y_g, z_g) and its interpolated surface $f(x, y)$ (see Appendix B). By considering the normal vector from the surface and the vector between the closest point on the surface and ghost node, we get the following system of non-linear equations:

$$\begin{cases} x - x_g + \partial_x f(x,y)\,[f(x,y) - z_g] &= 0 \\ y - y_g + \partial_y f(x,y)\,[f(x,y) - z_g] &= 0. \end{cases} \tag{3.4}$$

By solving the system for x and y using the steepest-descent method, we attain the location of the closest point at the surface relative to the ghost node (Rheinboldt, 1998). According to Figure 3.2, the normal is extended a distance ξ_R from the closest point at the boundary into the subsurface to locate ghost mirror $P_{g,m}$.

For a planar free surface, the distance ξ_R between P_g and the surface is equivalent to the distance $\xi_R^{'}$ between $P_{g,m}$ and the surface. However, if the surface is curved, the two distances (ξ_R and $\xi_R^{'}$) are not equal (Figure 3.3). Our algorithm accounts for curvature of the surface and corrects the location of the ghost mirror $P_{g,m}$ by assuming the free surface

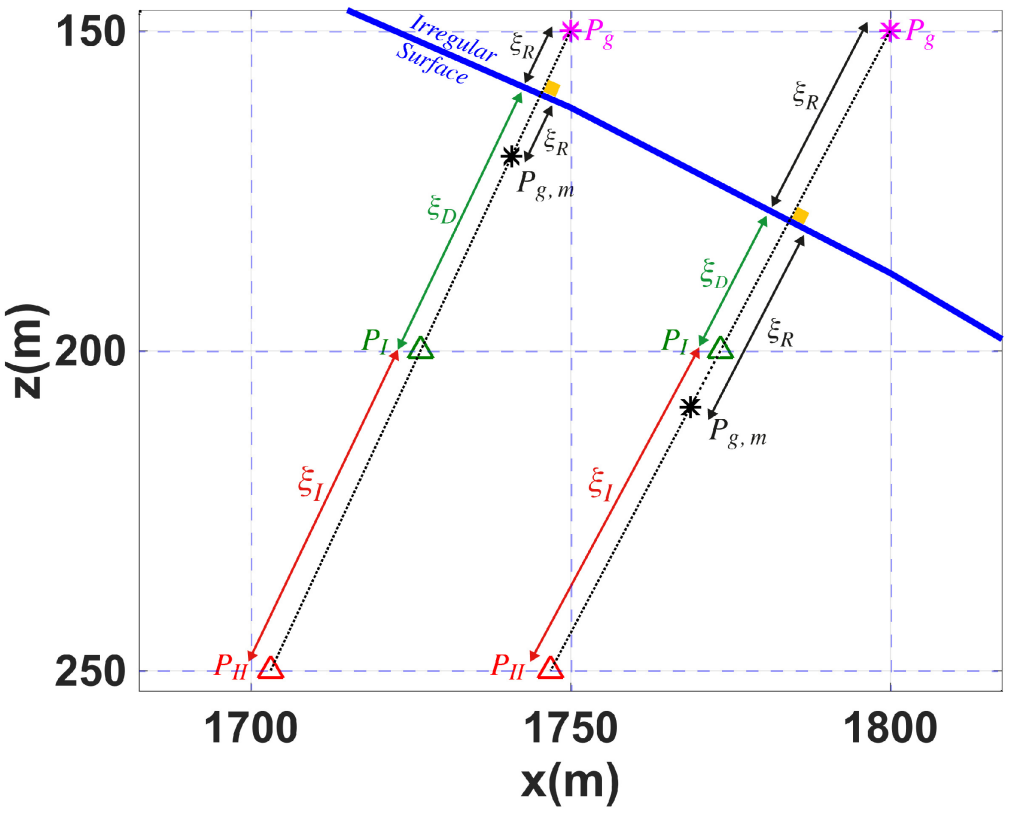

Figure 3.2: 2D y-axis slice from the three-dimensional second-order staggered grid: *Blue Line* denotes irregular surface, *Black Dashed Line* denotes irregular surface normal at each ghost point, *Magenta Stars* denote ghost nodes, *Orange squares* denote the closest point in the surface that is normal to the ghost node, *Black Stars* denote ghost mirrors, *Green and Red Triangles* denote known acoustic pressures, and ξ_R, ξ_D, and ξ_I are relative distances. Nodes have 50 m grid spacing.

is spherical. Since we know the approximated topography f, we can find the mean radius for the curvature using:

$$\begin{aligned} R &= \left| \frac{-2}{\nabla \cdot \hat{n}} \right| \\ &= \left| \frac{2 \cdot \left(1 + (\partial_x f)^2 + (\partial_y f)^2\right)^{3/2}}{(1 + (\partial_x f)^2)\partial_{yy} f - 2\partial_x f \partial_y f \partial_{xy} f + (1 + (\partial_y f)^2)\partial_{xx} f} \right|, \end{aligned} \tag{3.5}$$

where $\hat{n}$ is the normal to the local surface f (Spivak, 1981). Hence, $\xi_R^{'}$ can be found by:

$$\xi_R^{'} = R(1 - \frac{R}{a}), \tag{3.6}$$

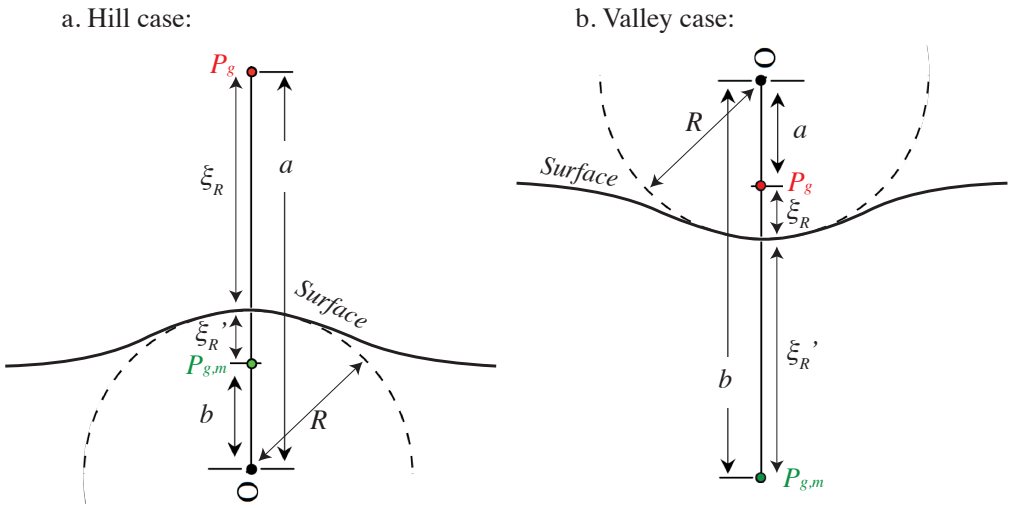

Figure 3.3: Method of images implementation: *Red Dot* denotes the location of the ghost node, *Green Dot* denotes the updated location of the ghost mirror due to the curved surface, R denotes the radius of the curvature, a is the distance between the curvature origin O and ghost node P_g, b is the distance between the curvature origin O and ghost mirror $P_{g,m}$, ξ_R is the distance between ghost node P_g and the surface and $\xi_R^{'}$ is the distance between ghost mirror $P_{g,m}$, and the surface.

and the ghost node P_g is related to the ghost mirror $P_{g,m}$ by:

$$P_g = -\left(\frac{a}{R}\right) P_{g,m}, \tag{3.7}$$

where R is the radius of the curvature and a is the distance between the curvature origin and ghost node P_g. Assuming the surface is curved produces marginally better results compared to assuming a planar surface. This is because topographic surfaces are not curved enough for this method to have a huge impact. For both planar and curved surfaces, the acoustic pressure value at the ghost mirror $P_{g,m}$ is necessary.

Second-order scheme implementation

To calculate the acoustic pressure at the ghost mirror points $P_{g,m}$, we consider both interpolation and extrapolation methods. Thus, the acoustic pressure at the first layer P_I and the acoustic pressure at the second layer P_{II} below the surface are needed (see Figure 3.2). We know the acoustic pressure at the surface to be zero, and the acoustic pressure at P_I and P_{II} can be approximated using bilinear interpolation. We either use linear extrapolation, quadratic interpolation, or a hybrid method to calculate acoustic pressures at ghost mirror points $P_{g,m}$ and hence their corresponding ghost nodes P_g (see Figure 3.2).

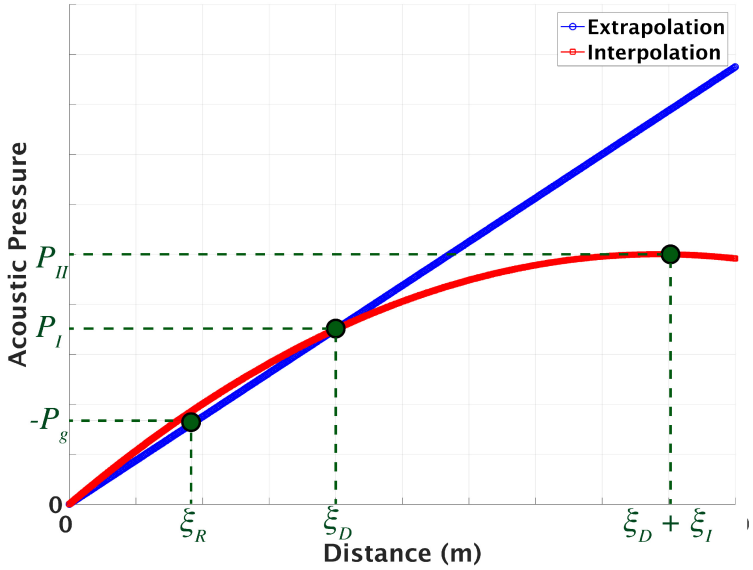

Figure 3.4: Linear extrapolation (*Blue Line*) and quadratic interpolation (*Red Line*) are used to approximate ghost node acoustic pressure P_g.

Quadratic interpolation needs three points to determine the ghost mirror acoustic pressure $P_{g,m}$. Figure 3.4 shows that to approximate the acoustic pressure of ghost nodes P_g, we use Lagrange quadratic interpolation on values 0, P_I, and P_{II} at locations 0, ξ_D, and $\xi_D + \xi_I$ (Li et al., 2010). To improve the accuracy of the quadratic interpolation, we use linear extrapolation.

Linear extrapolation is considered to reduce perturbations caused by points further below the surface such as P_{II}. It needs two points to locally determine each ghost mirror point acoustic pressure $P_{g,m}$, which is located a distance ξ_R from the surface. Following from Figure 3.2, Figure 3.4 illustrates the linear extrapolation method. Thus, the ghost node's acoustic pressure P_g can be found using linear Lagrange extrapolation on values 0, and P_I at positions 0 and ξ_D. We call it extrapolation because the distance ξ_R can be larger than ξ_D.

Hybrid method is a combination of the two previous methods. Depending on the location of the ghost mirror $P_{g,m}$ (Figure 3.2), grid spacing Δz, and a tuning coefficient α, it independently determines whether to use *linear extrapolation* or *quadratic interpolation* for each ghost node. Algorithm 1 illustrates the hybrid method. The hybrid method uses linear extrapolation if the ghost mirror is between the surface and P_I. However, if the ghost mirror is located between P_I and P_{II}, it decides whether to use linear extrapolation or quadratic interpolation depending on α, which ranges between 0 and 1. From the geometry in Figure 3.2, the maximum distance between P_I and ghost mirror is Δz if the mirror is located

between P_I and P_{II}. The hybrid method uses linear extrapolation if the ghost mirror is located between P_I and $P_I + \alpha * \Delta z$, otherwise if it falls between $P_I + \alpha * \Delta z$ and P_{II}, it uses quadratic interpolation.

Algorithm 1: Hybrid method used to determine whether to use linear extrapolation or quadratic interpolation for each ghost node

```
function Hybrid (α, Δz, ξ_R, ξ_D);
Input  : 0 ≤ α ≤ 1, and real values Δz, ξ_R, and ξ_D
Output: method
if ξ_R > (ξ_D + α · Δz) then
    method = 'quadratic interpolation';
    return method;
else
    method = 'linear extrapolation';
    return method;
end
```

Fourth-order scheme implementation

Due to the accuracy demands of the fourth-order FD schemes, the acoustic wave equation solution requires two layers of ghost nodes P_g above the surface. The first layer of ghost nodes is approximated using the *hybrid method*. The second layer of ghost nodes is located above the first layer. The acoustic pressures in the second layer are approximated using *quadratic interpolation*. Thus, three points are used to calculate the acoustic pressure at each ghost mirror $P_{g,m}$ in the second layer. The first two points are P_I, and P_{II}, which are found using bilinear interpolation. The third point P_{III} arises from extending the normal line further in the subsurface. Similarly, we use bilinear interpolation to approximate P_{III}. We also experimented using four points by including the zero acoustic pressure at the surface in addition to the three acoustic pressures P_I, P_{II} and P_{III}. This will result in a Lagrange cubic interpolation. These two methods will be called the two-layer hybrid quadratic and cubic methods. We also experimented with only one hybrid layer by setting the second layer above the surface to zero. We call this the one-layer hybrid method.

3.3 Results

We perform two simulations to test our embedded boundary methods for both second- and fourth-order FD schemes (Petrov and Newman, 2012). The first simulation is done by solving the acoustic wave equation in a homogeneous model with oblique planar topography. To measure the accuracy, we rotate the solution and compare the results with the analytical

solution for a flat free-surface model (Aki and Richards, 2002; Pujol, 2003). Relative error e_1 for the oblique planar topography is defined by:

$$e_1(\mathbf{r}_{\partial\Omega}) = \frac{||P_{sim}(\mathbf{r}_{\partial\Omega})| - |P_A(\mathbf{r}_{\partial\Omega})||}{|P_A(\mathbf{r}_{\partial\Omega})|} \times 100, \tag{3.8}$$

where $\mathbf{r}_{\partial\Omega} \in$ a surface $\partial\Omega$ that is parallel to the free-surface, P_{sim} is the simulation result and P_A is the analytical solution.

The second simulation addresses a homogeneous model with hill topography. Unlike the first simulation, there is no analytical solution for this case, and relative error e_2 is calculated relative to the maximum norm in the region Ω and is given by:

$$e_2(\mathbf{r}_{\partial\Omega}) = \frac{|P_{sim}(\mathbf{r}_{\partial\Omega})|}{\max\limits_{\mathbf{r}\in\Omega} |P_{sim}(\mathbf{r}_{\Omega})|} \times 100, \tag{3.9}$$

where $\mathbf{r}_{\Omega} \in$ region Ω and the denominator denotes the maximum value in the region.

Oblique planar surface

In the oblique planar-surface case, we have a sloping surface in which we can rotate its solution to compare it with the analytical solution (see Figure 3.5). The surface is sloping 42° clockwise from the horizontal. The minimum distance between the Ricker-wavelet source and the sloping surface is 890 m. The complex frequency of the source is $s = 1 + 2i$. We use relative error e_1 and average error $\langle e_1 \rangle$ to measure the accuracy of the oblique planar surface simulation.

For the second-order scheme, we will compare a FD solution that includes staircasing of topography in the simulation, as well as the embedded boundary conditions, based on linear extrapolation, quadratic interpolation, and hybrid method with $\alpha = 0.95$. We use a high tuning parameter α to bias the hybrid method to linear extrapolation. Most ghost mirror points are located closer to P_I than P_{II} and thus linear extrapolation better approximates the ghost mirror pressure $P_{g,m}$ than quadratic interpolation. For this comparison, we will implement a homogeneous media with P-wave velocity (V_P) of 2250 m/s, density (ρ) of 2300 kg/m^3, and grid spacing of 50 m. Figure 3.6a shows the relative error in pressure for the different simulation methods. All three embedded boundary methods provide accurate and similar results for the oblique planar surface relative to the true analytical solution. In general, the embedded boundary methods contain an average error of 1.3%, while the staircase method have an average error of 28.5% (Table 3.1a).

To ensure our method is continuous and differentiable, we study the pressure gradient. The results of the normal gradient (normal velocity component) will be specifically illustrated since geophysical techniques measure normal velocity. Both Figures 3.6b and 3.6c show that the average normal-velocity error for our embedded boundary methods is $\sim 1\%$ with respect to change in distance and depth.

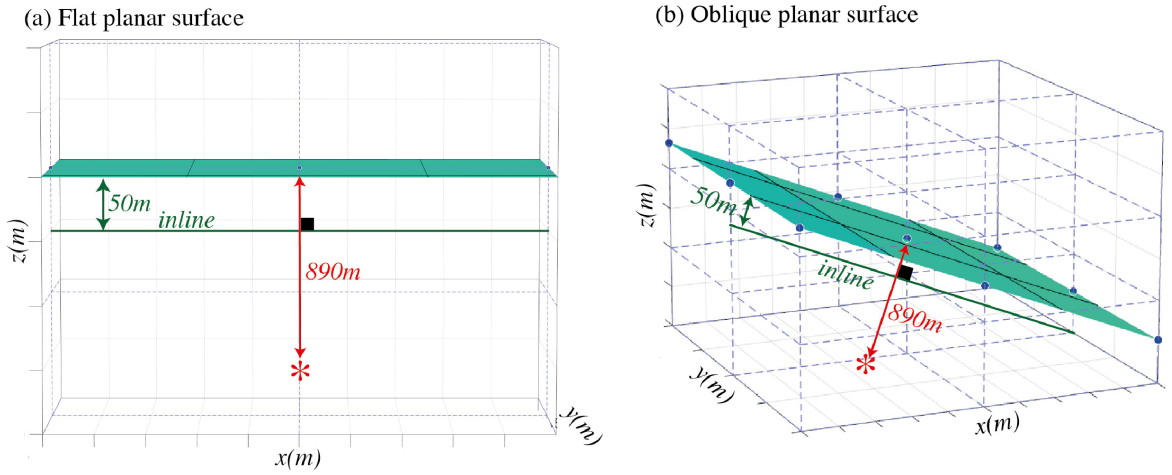

Figure 3.5: (a) The analytical free-surface case. The inline in *Green* is parallel to the flat surface. (b) The oblique planar free-surface case. The inline in *Green* is parallel to the oblique planar surface. The grid spacing is 50 m and the source denoted in *red* is 890 m below the surface.

Bohlen and Saenger (2006) concluded that to model topography with a staircase method, more than 60 grid points per minimum wavelength are required in a second-order scheme to obtain acceptable results. In Figure 3.7, we implemented an extreme case with approximately four points per wavelength at frequency 20 Hz with damping coefficient $1\frac{1}{s}$. To account for this increase in frequency, the velocity of the model was increased from 2250 m/s to 3250 m/s and the grid spacing reduced from 50 m to 15 m. The results show that our hybrid method produces results with an average error of $\sim$ 3% when compared to the analytical solution (Figure 3.8).

In the next numerical simulation, we demonstrate the solution of the acoustic wave equation more accurately with a fourth-order FD scheme. We use the same model setup as in the second-order FD scheme. The model is illustrated in Figure 3.5—it is homogeneous with P-wave velocity (V_P) of 2250 m/s, density (ρ) of 2300 kg/m^3, and grid spacing of 50 m. The complex frequency of the source is $s = 1 + 2i$. In this simulation, we compare the relative error in pressure between the staircase, one- and two-layer hybrid methods with $\alpha = 0.95$. As shown in Figure 3.9, the two-layer method's average error is 1.3%. The one-layer method achieves an average accuracy of 5.4%. Similar to the previous simulation, the average accuracy of the staircase method is 23.5% (Table 3.2a).

Hill model

To further measure the accuracy, we test our schemes on a hill surface. In terms of source type, source location, P-wave velocity, and density, the same configurations will be used as in the oblique planar simulations. As in the previous simulation, the complex frequency of

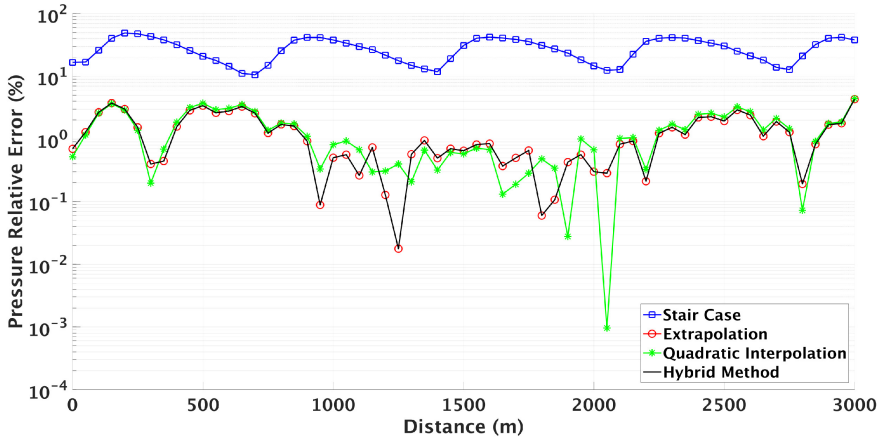

(a) Error in pressure with distance.

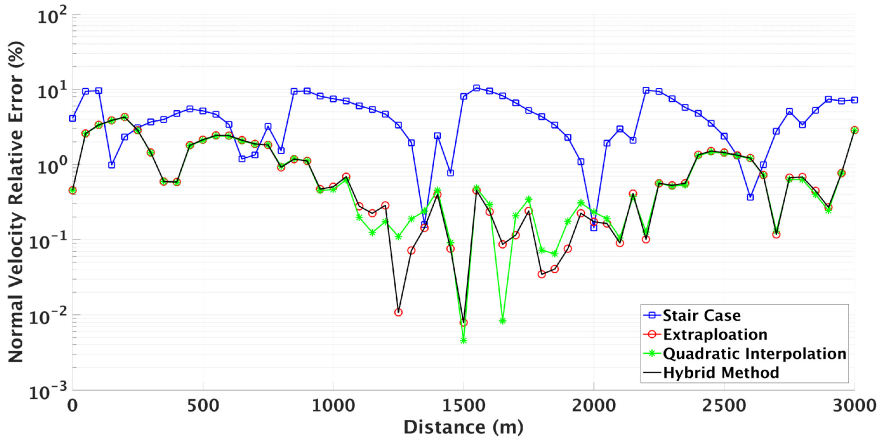

(b) Error in velocity with distance.

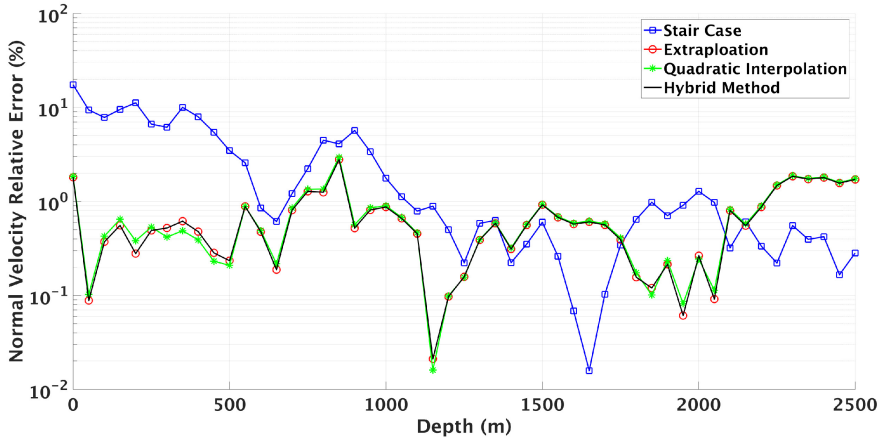

(c) Error in velocity with depth.

Figure 3.6: Error for *second-order* FD scheme staircase and embedded boundary methods relative to the true analytical solution.

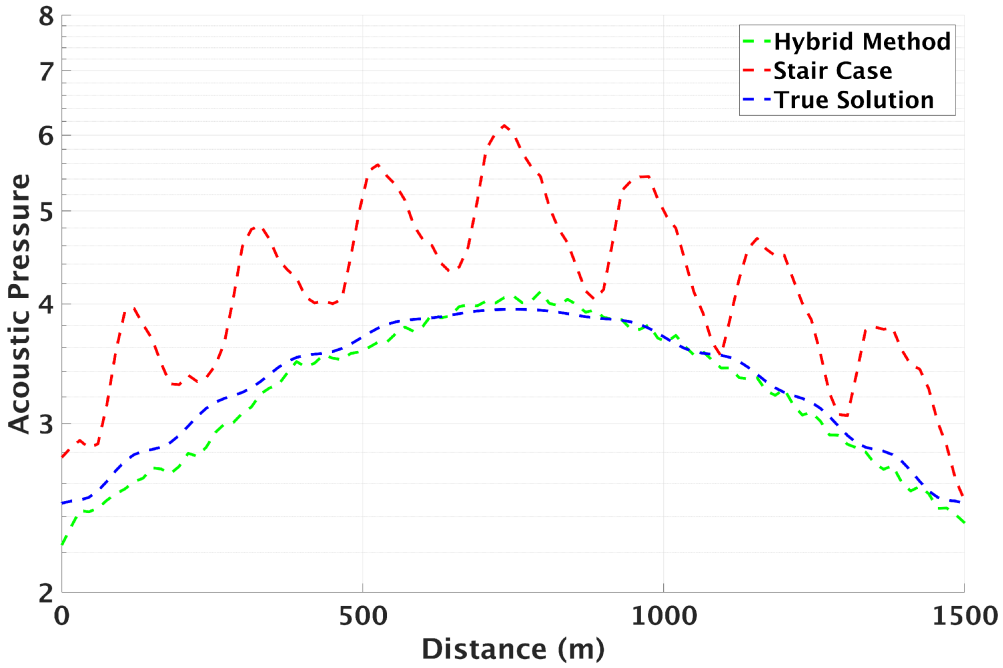

Figure 3.7: Absolute pressure for *second-order* FD scheme true, staircase and hybrid method solutions. The plot demonstrates the solution 50 m below the surface for a frequency of 20 Hz with damping $1\frac{1}{s}$.

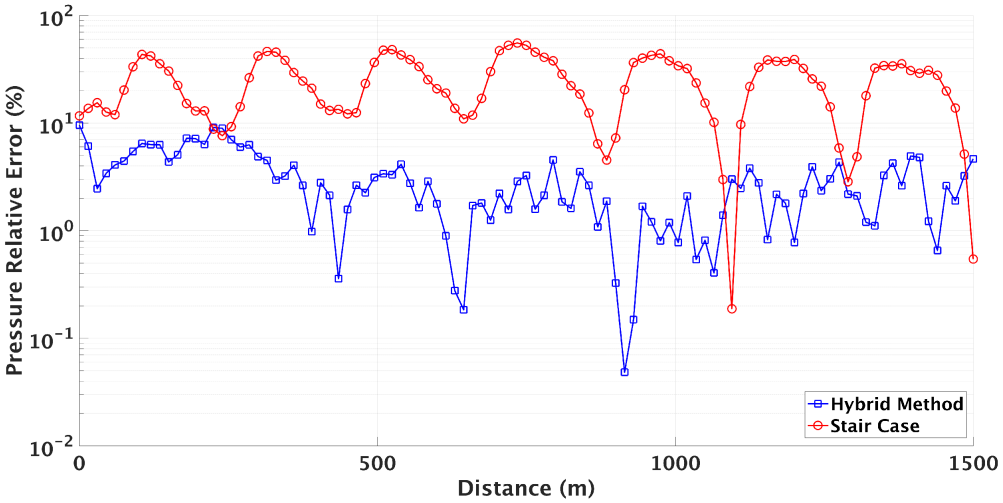

Figure 3.8: Relative error e_1 for *second-order* FD scheme staircase and hybrid method acoustic pressure relative to the true analytical solution. The plot demonstrates the error 50 m below the surface for a frequency of 20 Hz with damping $1\frac{1}{s}$.

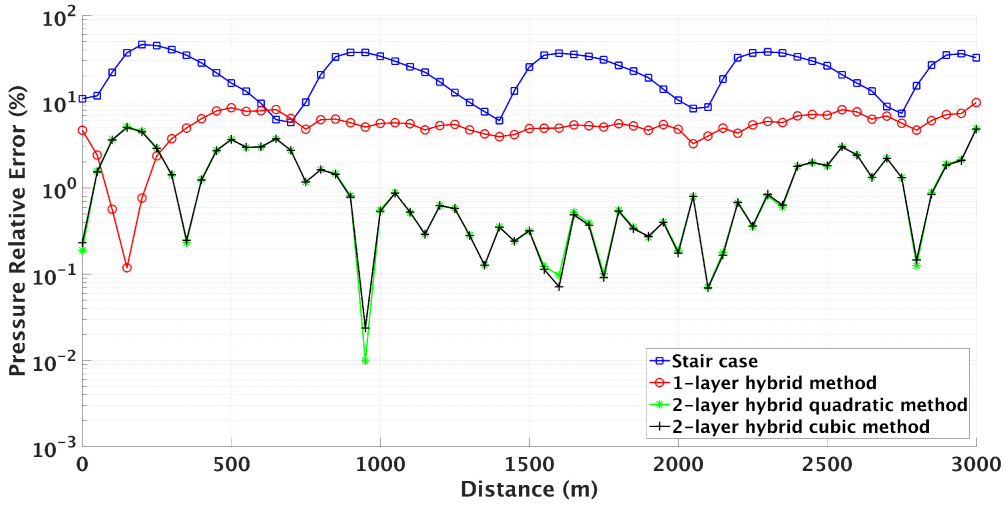

Figure 3.9: Relative error e_1 for *fourth-order* FD scheme staircase and embedded boundary methods relative to the true analytical solution.

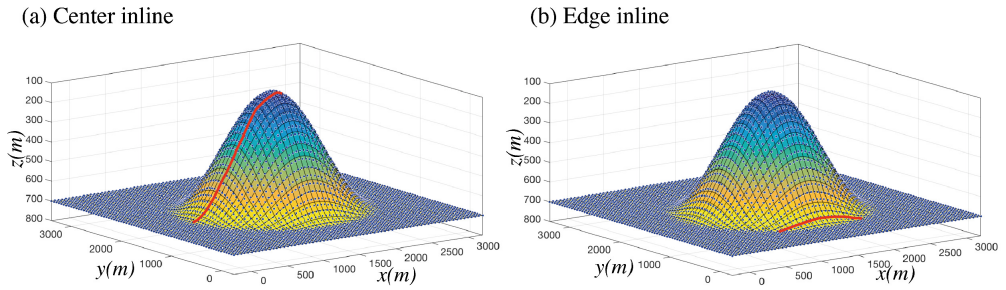

Figure 3.10: (a) Hill topography with *red line* denoting central line profile. (b) Hill topography with *red line* denoting edge line profile. The grid spacing is 50 m in all three components and the source is located at $(x, y, z) = (1200, 1200, 2600)$m.

the source is $s = 1 + 2i$. We use relative error e_2 and average error $\langle e_2 \rangle$ to measure the accuracy of the hill-surface simulation. Figure 3.10 illustrates the hill surface used for this experiment. The *red lines* denote profiles that will be studied in this section.

We use second-order FD scheme to the acoustic wave equation. The tuning constant used for the hybrid method is $\alpha = 0.95$. We first start by comparing the *central line* profile shown in Figure 3.10a. Similar to the oblique planar simulation, all three embedded boundary methods have two orders of magnitude improvement over the staircase method (Table 3.1b). Furthermore, all three embedded methods show approximately the same improvement (see Figure 3.11a). But for the *edge line* profile (Figure 3.10b), the linear extrapolation and the hybrid method provide more than two times better accuracy compared to the quadratic interpolation (Figure 3.11b and Table 3.1b).

Spacing has been reduced for the staircase solution to demonstrate that when spacing is

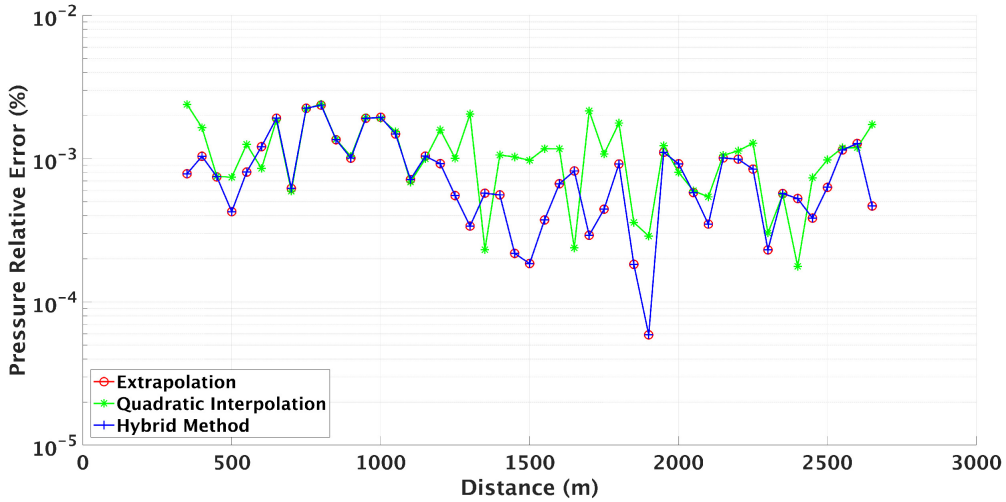

(a) Central line error.

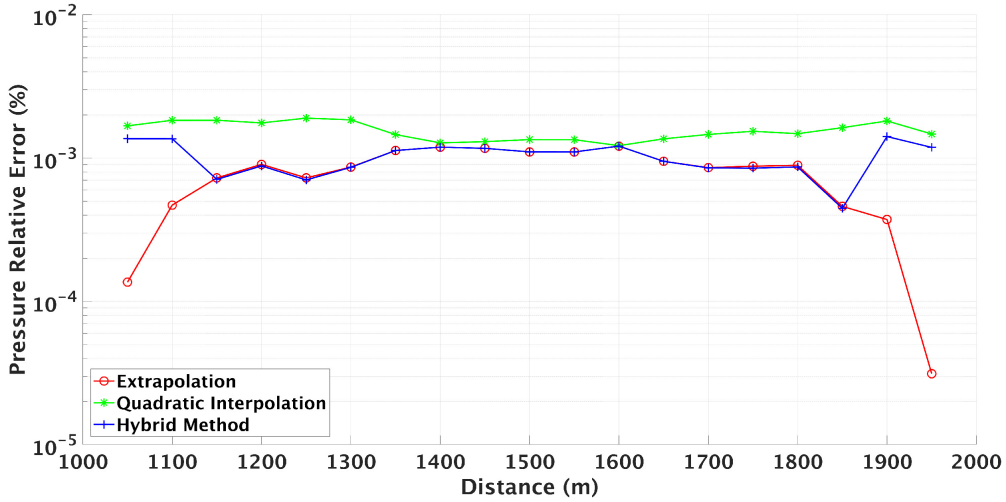

(b) Edge line error.

Figure 3.11: Relative error e_2 for *second-order* FD scheme embedded boundary methods at the (a) *central line* shown in Figure 3.10a and (b) *edge line* shown in Figure 3.10b.

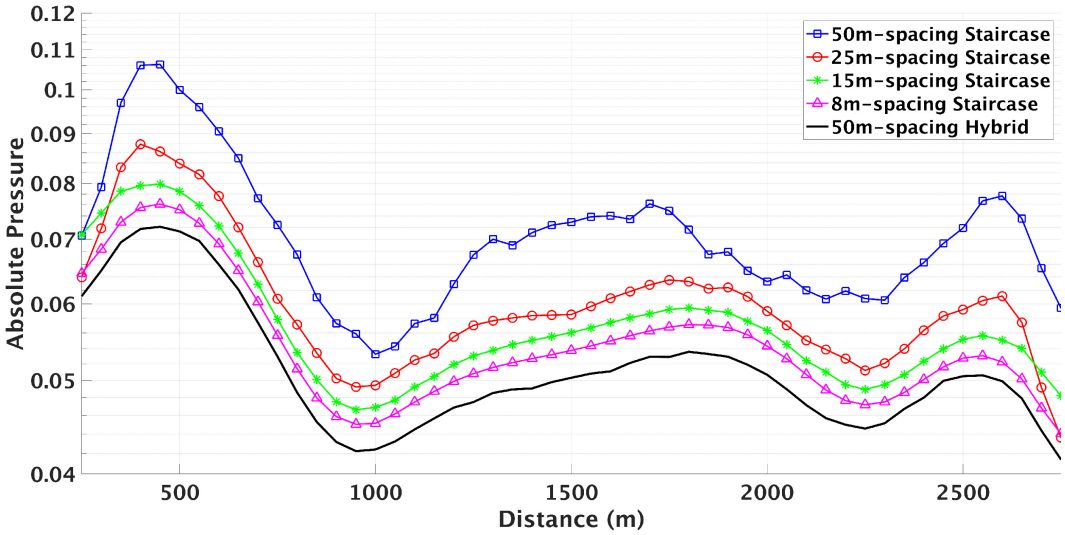

Figure 3.12: Absolute pressure solutions for *second-order* FD scheme embedded boundary methods with different spacings for the hill model *central line* at 50 m below the surface.

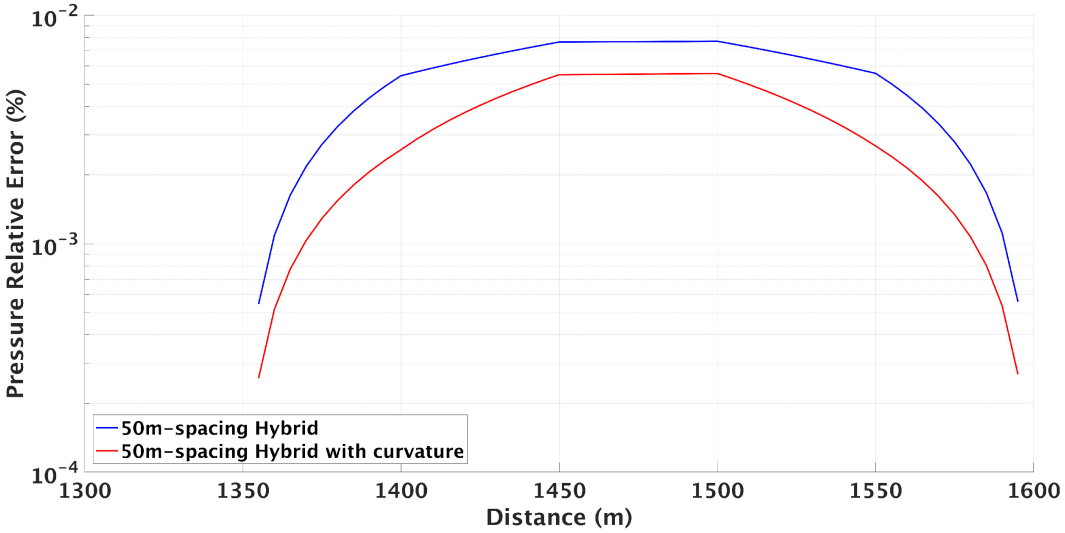

Figure 3.13: Relative error e_2 for *second-order* FD scheme embedded boundary methods at *edge line* for a stretched hill with height 1500 m.

reduced for the staircase method, the higher resolution solution converges to the embedded method solution with spacing 50 m (Figure 3.12).

To study the effectiveness of our curvature method, we stretched the hill model to have a height of 1500 m instead of the 700 m in Figure 3.10. In Figure 3.13, we show that when the *edge line* curvature radius is small, the error for the solution with curvature correction is reduced up to two times than error for the solution without the curvature correction.

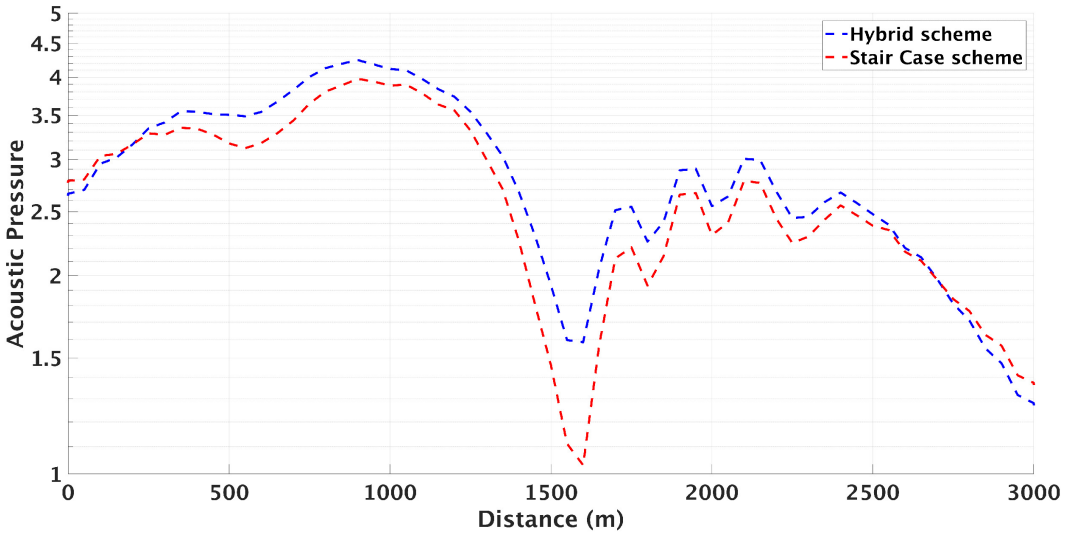

Figure 3.14: Absolute pressure for *second-order* FD scheme embedded boundary methods at *central line* shown in Figure 3.10a at 100 m below the surface. The plot demonstrates the solutions for a frequency of 20 Hz with damping $1\frac{1}{s}$.

In Figure 3.14, we implemented an extreme case with approximately four points per wavelength at frequency 20 Hz with damping coefficient $1\frac{1}{s}$. The velocity and spacing have been changed as in the oblique planar case. The results show that our hybrid method produces results with two orders of magnitude improvement over the staircase method as with frequency 2 Hz (Figure 3.15).

Now, the acoustic wave equation is solved using a fourth-order FD scheme. We compare solutions for both the *central line* and *edge line* profiles shown in Figure 3.10. Contrary to the oblique-planar model simulation, Figure 3.16 only shows marginal improvement when using the two-layer hybrid methods over the one-layer hybrid method (Table 3.2b).

Solver convergence rates

Efficient convergence rates are essential for solving the forward problem because it is the driving engine in the solution of the inverse problem. Thus, the forward problem will be solved many times to reach the best-fit model for the data. Here, we study the convergence rates to decide which embedded boundary method is more computationally efficient. All the tests were conducted on a 2013 Macbook Pro with 2.4GHz dual-core Intel i5 processor, 3MB shared L3 cache and 8GB of 1600MHz DDR3L onboard memory. We use a Krylov subspace IDR iterative solver to solve the forward model at interior nodes (Sonneveld and van Gijzen, 2008). Direct solvers can also be used for small simulations or as a preconditioner for the iterative solver.

We start the first set of tests with second-order FD schemes for a homogeneous medium. We compare between different topographies and embedded boundary methods. For the

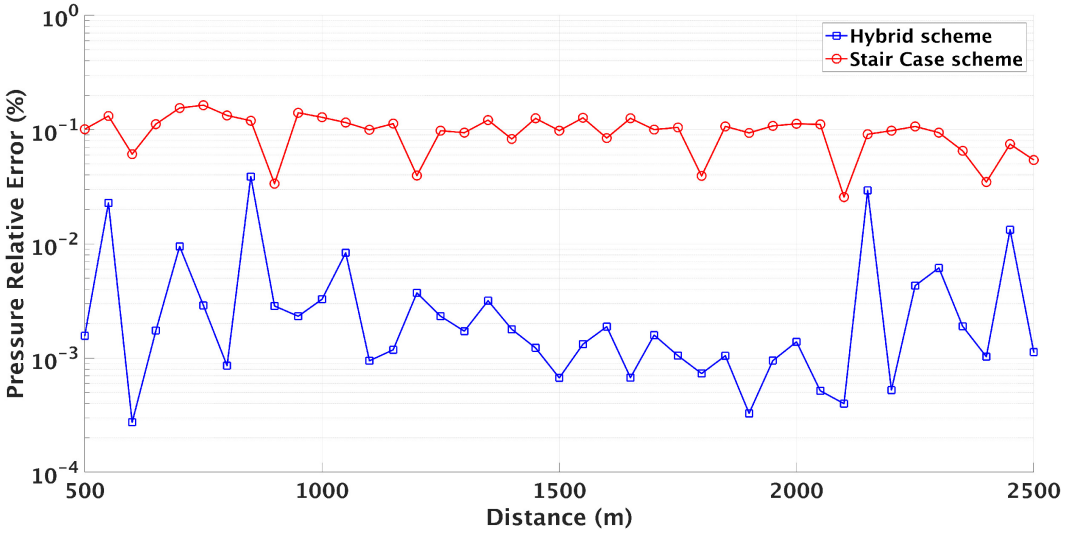

(a) Central line error.

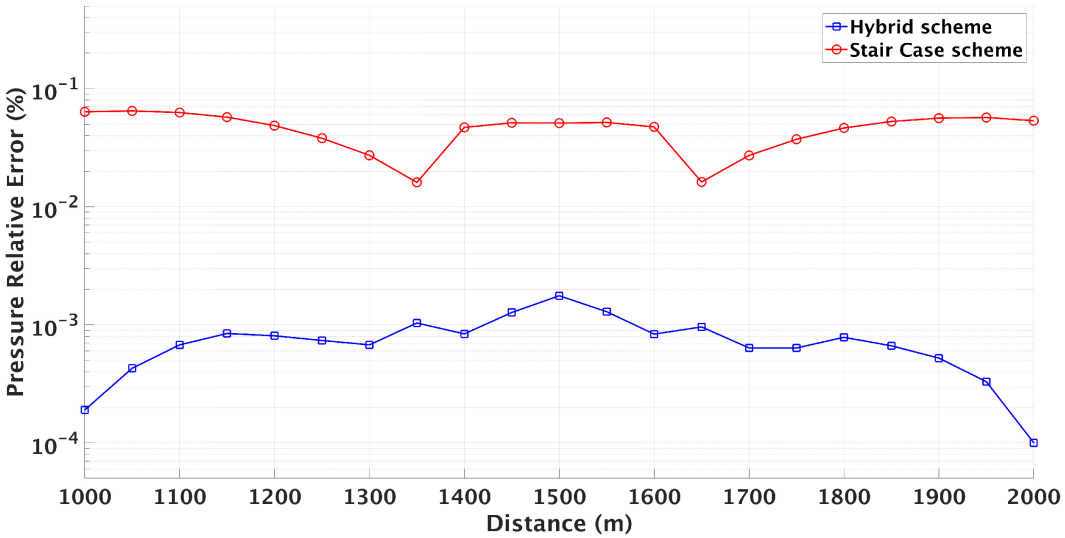

(b) Edge line error.

Figure 3.15: Relative error e_2 for *second-order* FD scheme embedded boundary methods at (a) *central line* shown in Figure 3.10a and (b) *edge line* shown in Figure 3.10b. The plot demonstrates the error for a frequency of 20 Hz with damping $1\frac{1}{s}$.

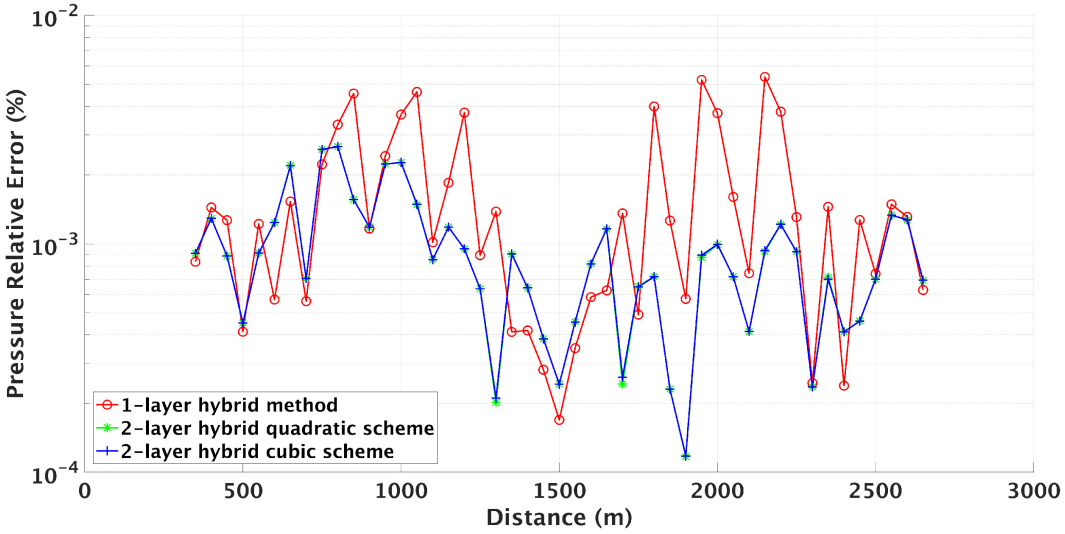

(a) Central line error.

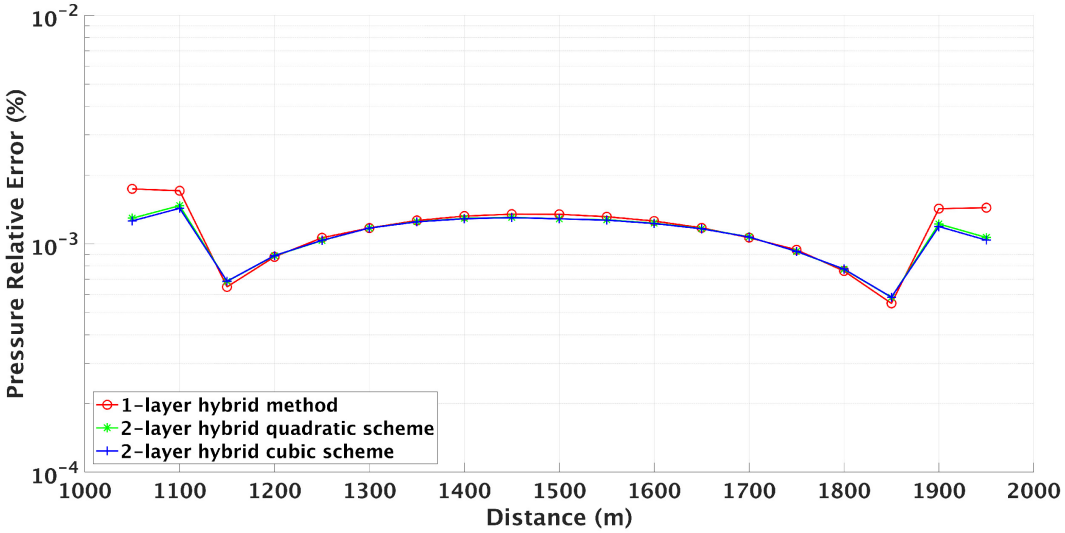

(b) Edge line error.

Figure 3.16: Relative error e_2 for *fourth-order* FD scheme embedded boundary methods at the (a) *central line* shown in Figure 3.10a and (b) *edge line* profile shown in Figure 3.10b.

Table 3.1: Second order FD scheme for the acoustic wave equation in a homogeneous media with mesh size $70 \times 74 \times 85$. The source frequency is 2 Hz with damping coefficient $1\frac{1}{s}$.

a. Oblique-planar

Topography type	Topography method	Iterations	Time (s)	Average Error $\langle e_1 \rangle$ (%)
Flat free-surface	—	980	~ 66	—
Oblique-planar	Staircase	951	~ 71	28.5
Oblique-planar	Linear extrapolation	1038	~ 57	1.3
Oblique-planar	Quadratic interpolation	1221	~ 66	1.4
Oblique-planar	Hybrid with $\alpha = 0.95$	1038	~ 57	1.3

b. Hill Surface

Topography type	Topography method	Iterations	Time (s)	Average Error $\langle e_2 \rangle$ (%)
Hill Surface	Staircase	1079	~ 70	5.8×10^{-2}
Hill Surface	Linear extrapolation	13 542	~ 718	8.1×10^{-4}
Hill Surface	Quadratic interpolation	1432	~ 80	1.4×10^{-3}
Hill Surface	Hybrid with $\alpha = 0.95$	3768	~ 211	9.3×10^{-4}

oblique-planar surface, there is no considerable difference in terms of number of iterations or convergence rate (Table 3.1). It is better to use the linear extrapolation method since it is slightly more accurate. However, the hill irregular surface shows a spike in the number of iterations and a corresponding increase in time for the linear extrapolation solution (Table 3.1). We have observed that the linear extrapolation takes more time to converge when there are more ghost points closer to P_{II} than P_I. Thus, it is more efficient to implement the hybrid method with $\alpha = 0.95$. The hybrid-method results are similar in accuracy to the linear extrapolation but have better convergence rates as shown in Table 3.1. On the other hand, the quadratic interpolation is faster but has marginally less accuracy.

Since linear extrapolation is accurate but inefficient and quadratic interpolation is efficient but not as accurate, we experimented with different tuning ratios α to find the best compromise in efficiency and accuracy. In Figure 3.17, we show that $\alpha = 0.95$ provides a good trade-off. It is accurate relative to linear extrapolation ($\alpha = 1$) and also efficient as shown in Table 3.1b.

We compare tests for the fourth-order FD schemes for a homogeneous medium. In these tests, we compare between the one- and two-layer hybrid methods as shown in Table 3.2. For the oblique-planar and hill surfaces, the two-layer hybrid quadratic method is approximately ten times slower than the one-layer hybrid method. Despite its slightly less accurate solution, the one-layer hybrid method is substantially more time efficient than the two-layer

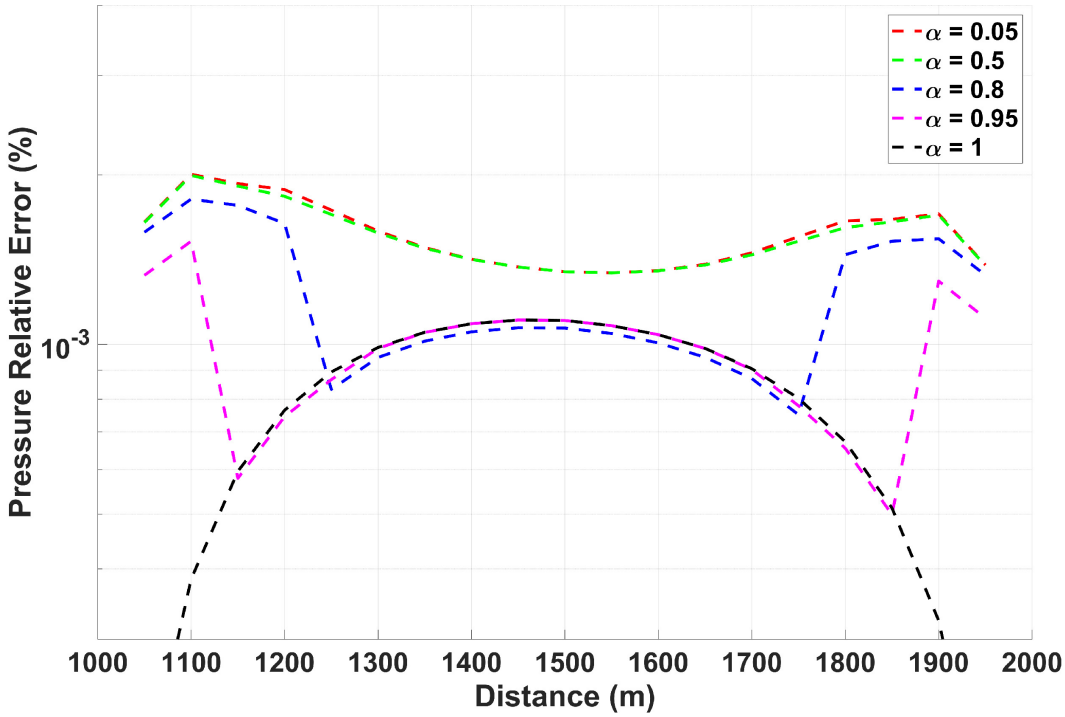

Figure 3.17: Relative error e_2 for *second-order* FD scheme hybrid method at *edge line* for different tuning ratios α.

hybrid quadratic method. However, using a two-layer hybrid cubic method can reduce time inefficiencies. In fact, for the central hill profile, the solution times for the two-layer hybrid cubic are comparable with the one-layer hybrid method.

Table 3.2: Fourth order FD scheme for the acoustic wave equation in a homogeneous media with mesh size $70 \times 74 \times 85$. The source frequency is 2 Hz with damping coefficient $1\frac{1}{s}$.

a. Oblique-planar

Topography type	Topography method	Iterations	Time (s)	Average Error $\langle e_1 \rangle$ (%)
Flat free-surface	—	1328	~ 105	—
Oblique-planar	Staircase	1084	~ 77	23.5
Oblique-planar	One-layer hybrid with $\alpha = 0.95$	1531	~ 106	5.4
Oblique-planar	Two-layer hybrid quadratic with $\alpha = 0.95$	12 012	~ 815	1.3
Oblique-planar	Two-layer hybrid cubic with $\alpha = 0.95$	9590	~ 650	1.3

b. Hill Surface

Topography type	Topography method	Iterations	Time (s)	Average Error $\langle e_2 \rangle$ (%)
Hill Surface	Staircase	1395	~ 113	6.2×10^{-2}
Hill Surface	One-layer hybrid with $\alpha = 0.95$	4281	~ 300	1.5×10^{-3}
Hill Surface	Two-layer hybrid quadratic with $\alpha = 0.95$	40 002	~ 2800	1.0×10^{-3}
Hill Surface	Two-layer hybrid cubic with $\alpha = 0.95$	4745	~ 309	1.0×10^{-3}

Chapter 4

Discontinuous mesh method

4.1 Introduction

Finite-difference (FD) methods that solve the acoustic wave equation over a discrete set of grid points have the great advantage of being able to handle realistic geological structures of arbitrary complexity (Graves, 1996). However, their computational cost grows with the number of required grid nodes making it a computationally challenging problem (Operto et al., 2007; Fichtner, 2011). One of the important reasons is the high contrast of seismic-wave velocities found in real earth structures, especially the near-surface low-velocity regions in arid environments. Other reasons include requiring more grid points for 3-D models (vs. 2-D), and applying a high-frequency point source. Simulation of wave propagation either ignores the relatively thin low-velocity regions or includes them using a uniform grid size that is determined by the lowest velocity because it has the shortest wavelength. The first simulation produces inaccurate results which causes the simulated data to misrepresent the true data. The second simulation results in oversampling the deeper regions with higher velocity inevitably leading to a considerable increase of computational time and memory. For these reasons, it is preferable to use different discretizations in shallow and deep regions.

There are several other numerical solution methods naturally suited for modeling seismic fields over complex surfaces. For example, finite element (FE) methods solve a system of equations derived from a weak form of the wave equation. Using unstructured grids (e.g. tetrahedral meshes), FE methods can accurately and economically discretize arbitrary complex topography and horizons (Bao et al., 1998). Spectral element (SE) methods (Komatitsch and Tromp, 1999) are similar to the p version of FE methods (Jin, 2015) and can also discretize a computational domain into unstructured meshes adapted to irregular surfaces.

However, their advantage over FD methods come with extra complications. For example, it is not straightforward to develop an effective regularization matrix for tetrahedral meshes (Zhang, 2017). Generation, visualization and analysis of tetrahedral meshes are also cumbersome and difficult especially when fine scale elements for complex irregular surface

and faults are mixed with large scale elements for regional geology (Casarotti et al., 2008). Fast and accurate generation and display of large multi-scale tetrahedral meshes is currently an active research area in computational mathematics and engineering. In contrast, the use of the structured FD grids allows us to easily and rapidly construct, visualize and analyze earth models. More importantly, from a practical point of view, most geoscience modeling tools are built on rectangular meshes. Thus, the use of rectangular meshes in seismic modeling allows us to import and export velocity models to flow and reservoir simulators.

Several authors have developed FD methods with grid spacing changing in time-domain. Moczo (1989) and Pitarka (1999) developed FD methods with grid spacing changing gradually over a distance separating a fine and coarse mesh, which are less efficient and less flexible to apply as compared to discontinuous mesh (DM) methods. To accurately and efficiently model realistic geological structures, other varieties of DM methods have been proposed (e.g., Aoi and Fujiwara, 1999; Tessmer, 2000; Hayashi et al., 2001; Wang et al., 2001; Kristek et al., 2010; Zhang et al., 2012b). The time-domain FD DM implementations suffer inherently from stability problems after a large number of timesteps (Nie et al., 2017). Furthermore, none of the authors assessed the DM method in the frequency or Laplace-Fourier (LF) domain.

In this chapter, we introduce a DM into second- and fourth-order LF domain velocity-pressure staggered FD scheme with topography to simulate acoustic wave propagation. The uniform grid acoustic implementation from Petrov and Newman (2012) and AlSalem et al. (2018) is now developed to be highly scalable using PETSc numerical libraries (Balay et al., 2018). The implementation is currently an important forward modeling tool for the full waveform inversion iterative simulations. These simulations are being pushed to higher frequencies with realistic 3D heterogeneous velocity models to meet the requirements of gas and oil exploration in arid environments. Here, we introduce an interface between fine and coarse meshes and benchmark the method for accuracy, convergence and efficiency in a series of tests. Furthermore, we evaluate direct and iterative parallel solvers that are included in PETSc for computational speed, memory requirements and convergence. These validation tests include a simple homogeneous model in a sloping free surface, a low contrast layered velocity model underlying a hill free surface, and a high contrast layered velocity model underlying realistic topography provided by Saudi Aramco.

4.2 Discontinuous mesh implementation

Theory

In typical seismic models, the velocity and density tend to increase with depth. Hence, simulation of seismic wave propagation using a spatially uniform mesh can be computationally very demanding due to the over-discretization of the high-velocity material. Thus, small grid sizes can be used at the top and larger grid sizes can be used at deeper regions of the model. This issue can be partly addressed by varying grid sizes (Δz) with depth. However,

lateral grid sizes (Δx and Δy) are still constrained by the global minimum velocity (Pasalic and McGarry, 2010). One approach is to discontinuously vary Δx, Δy, and Δz grid sizes along the z direction to take advantage of variations in velocity. Figure 2.2 shows the layout of the three velocity components and acoustic pressure, indicating that the most basic way to implement a DM is to use a ratio of spatial discretization H/h between the coarse (H) and the fine (h) grids. In this example, we consider the case of $H/h = 3$ to demonstrate the advantage of the DM method. Updating v_x in a high-velocity material using the uniform second-order FD method requires pressure values at $\pm(1/2)h$, while the DM method skips the nearest pressure values and uses $\pm(3/2)h$ instead.

Since the velocity components are partial derivatives of acoustic pressure (equation 2.1), we focus on only illustrating the acoustic pressure values in the DM FD approximation. Our approach divides the model into a number of regions, separated by horizontal planes (Figure 4.1). Within each region, Δx, Δy and Δz are uniform and equal; however, they vary from one region to another. In this way, discretization becomes a discontinuous function of depth.

Communication across region interfaces

In each discontinuous region, the wave propagation FD discretization can be performed as for the uniform mesh. However, we clearly need to have some communication across the regions' interfaces (Figure 4.1). To demonstrate the communication, we consider a fourth-order FD example with two 1D regions as illustrated in Figure 4.2. The spacing ratio between the coarse and fine regions is $H/h = 1.5$. The open nodes in the Figure are approximated using fourth-order FD while the filled nodes are approximated using interpolation and down-sampling to update the missing fine grid and coarse grid nodes, respectively. To realize these approximations in one matrix, we provide the following steps:

1. Generate fine- and coarse-mesh 1D fourth-order FD matrices for each region with grid sizes h and H, respectively:

$$A_f = \begin{bmatrix} A_{f_{11}} & A_{f_{12}} \\ A_{f_{21}} & A_{f_{22}} \end{bmatrix}, \quad A_c = \begin{bmatrix} A_{c_{11}} & A_{c_{12}} \\ A_{c_{21}} & A_{c_{22}} \end{bmatrix}. \tag{4.1}$$

   Here, A_f and A_c are the fourth-order FD square matrices for the fine and coarse regions, respectively. A_f includes n_f fine grid nodes (rows) in the fine region plus three fine grid nodes (rows) in the coarse region. Similarly, A_c includes n_c coarse grid nodes in the coarse region plus three coarse grid nodes in the fine region as shown in Figure 4.2. Using this information, we split A_f to four submatrices where the size of $A_{f_{11}}$ is $(n_f \times n_f)$, $A_{f_{12}}$ is $(n_f \times 3)$, $A_{f_{21}}$ is $(3 \times n_f)$, and $A_{f_{22}}$ is (3×3). Inversely, we split A_c into four submatrices where the size of $A_{c_{11}}$ is (3×3), $A_{c_{12}}$ is $(3 \times n_c)$, $A_{c_{21}}$ is $(n_c \times 3)$, and $A_{c_{22}}$ is $(n_c \times n_c)$.

2. Remove rows containing non-regional grid nodes ($A_{f_{21}}$, $A_{f_{22}}$, $A_{c_{11}}$, and $A_{c_{12}}$) in the square matrices (A_f and A_c) and keep the regional grid nodes ($A_{f_{11}}$ and $A_{c_{22}}$) and

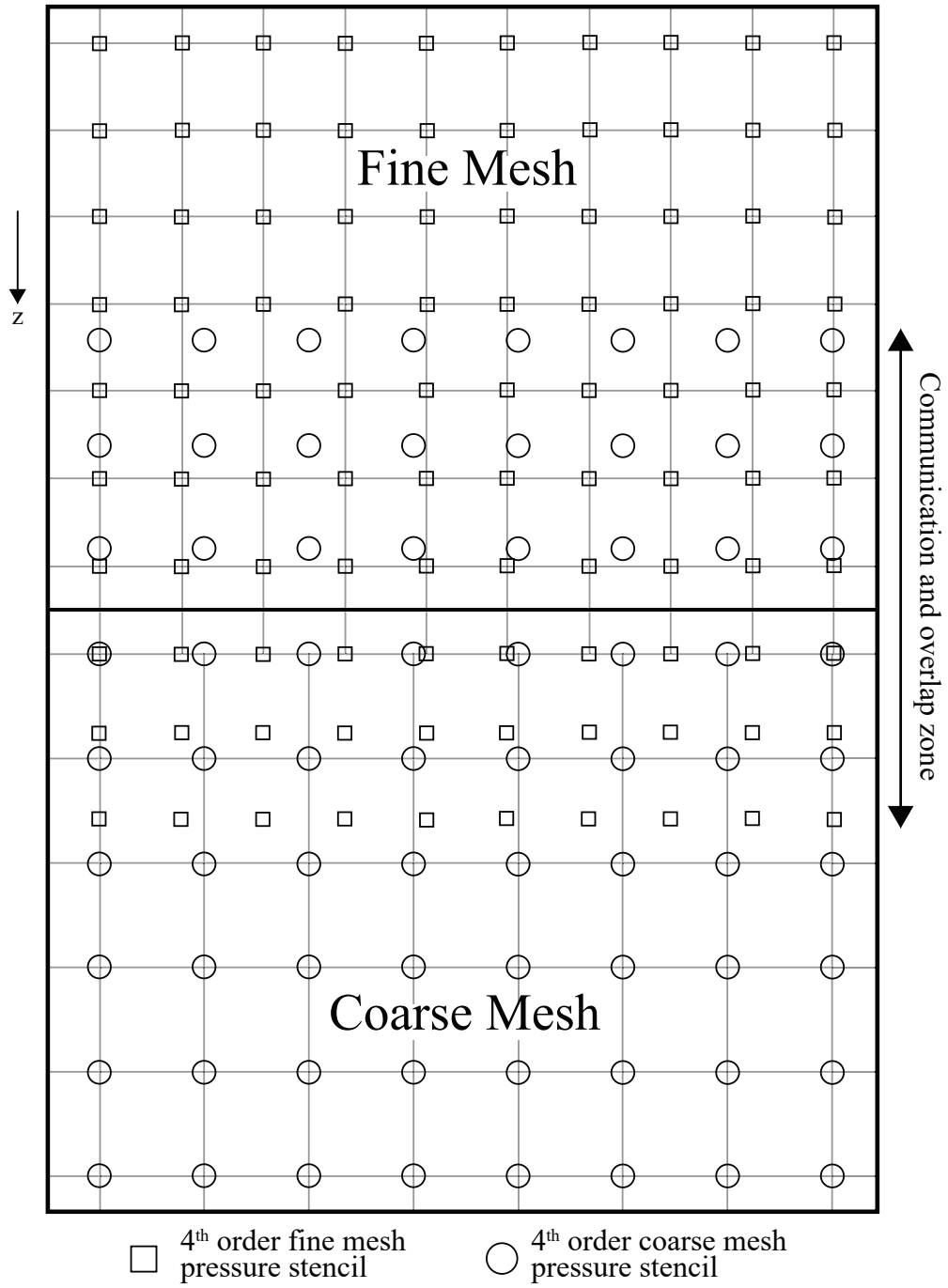

Figure 4.1: Communication between a fine and coarse mesh in 2D for fourth-order FD scheme. Overlapped stencils for each region in 2D are found using simple bilinear interpolation for three layers of stencils. The interface between the differently-spaced meshes is shown as a bold horizontal line.

their communication stencils ($A_{f_{12}}$ and $A_{c_{21}}$). We end up with the following rectangular matrices:

$$A'_f = \begin{bmatrix} A_{f_{11}} & A_{f_{12}} \end{bmatrix}, \quad A'_c = \begin{bmatrix} A_{c_{21}} & A_{c_{22}} \end{bmatrix}. \tag{4.2}$$

3. Generate the coarse to fine grid linear interpolation (trilinear interpolation in 3D) matrix depending on the positions of the interpolated fine grid nodes (filled squares) in Figure 4.2:

$$A_{fc} = \begin{bmatrix} 1 & 0 & 0 \\ \frac{1}{3} & \frac{2}{3} & 0 \\ 0 & \frac{2}{3} & \frac{1}{3} \end{bmatrix}. \tag{4.3}$$

4. Generate the fine to coarse grid linear downsampling (trilinear downsampling in 3D) matrix depending on the positions of the downsampled coarse grid nodes (filled circles) in Figure 4.2:

$$A_{cf} = \begin{bmatrix} \frac{1}{2} & \frac{1}{2} & 0 & 0 & 0 \\ 0 & 0 & 1 & 0 & 0 \\ 0 & 0 & 0 & \frac{1}{2} & \frac{1}{2} \end{bmatrix}. \tag{4.4}$$

5. Merge the matrices together to get the fourth-order DM FD square matrix for two regions:

$$A_{DM} = \begin{bmatrix} A_{f_{11}} & A_{f_{12}} \cdot A_{fc} \\ A_{c_{21}} \cdot A_{cf} & A_{c_{22}} \end{bmatrix}. \tag{4.5}$$

We call $A_{f_{11}}$ and $A_{c_{22}}$ the forward modeling operators and $A_{f_{12}} \cdot A_{fc}$ and $A_{c_{21}} \cdot A_{cf}$ the interpolation and downsampling operators, respectively. We pad the right side of the interpolation operator and the left side of the downsampling operator with zeros to ensure the matrix is square. We can rewrite the linearlized problem for two regions as:

$$\begin{bmatrix} A_{f_{11}} & A_{f_{12}} \cdot A_{fc} \\ A_{c_{21}} \cdot A_{cf} & A_{c_{22}} \end{bmatrix} \begin{bmatrix} P_f \\ P_c \end{bmatrix} = \begin{bmatrix} F_f \\ F_c \end{bmatrix}, \tag{4.6}$$

where the size of each of P_f and F_f is n_f, and the size of each of P_c and F_c is n_c. We observe from equation 4.6 that the communication stencils $A_{f_{12}}$ and $A_{c_{21}}$ are linked to the differently-spaced grid nodes using the interpolation A_{fc} and downsampling A_{cf} matrices, respectively.

For the 3D case, this is done by simple trilinear interpolation and downsampling across the relevant acoustic pressure values from one region to another for any H/h ratio. Hence, using FD, the acoustic wave propagation in LF domain can be approximated by:

$$\begin{bmatrix} A_1 & A_{1,2} & 0 & \cdots & 0 \\ A_{2,1} & A_2 & A_{2,3} & \ddots & \vdots \\ 0 & \ddots & \ddots & \ddots & 0 \\ \vdots & \ddots & A_{n-1,n-2} & A_{n-1} & A_{n-1,n} \\ 0 & \cdots & 0 & A_{n,n-1} & A_n \end{bmatrix} \begin{bmatrix} P_1 \\ \vdots \\ P_n \end{bmatrix} = \begin{bmatrix} F_1 \\ \vdots \\ F_n \end{bmatrix}, \tag{4.7}$$

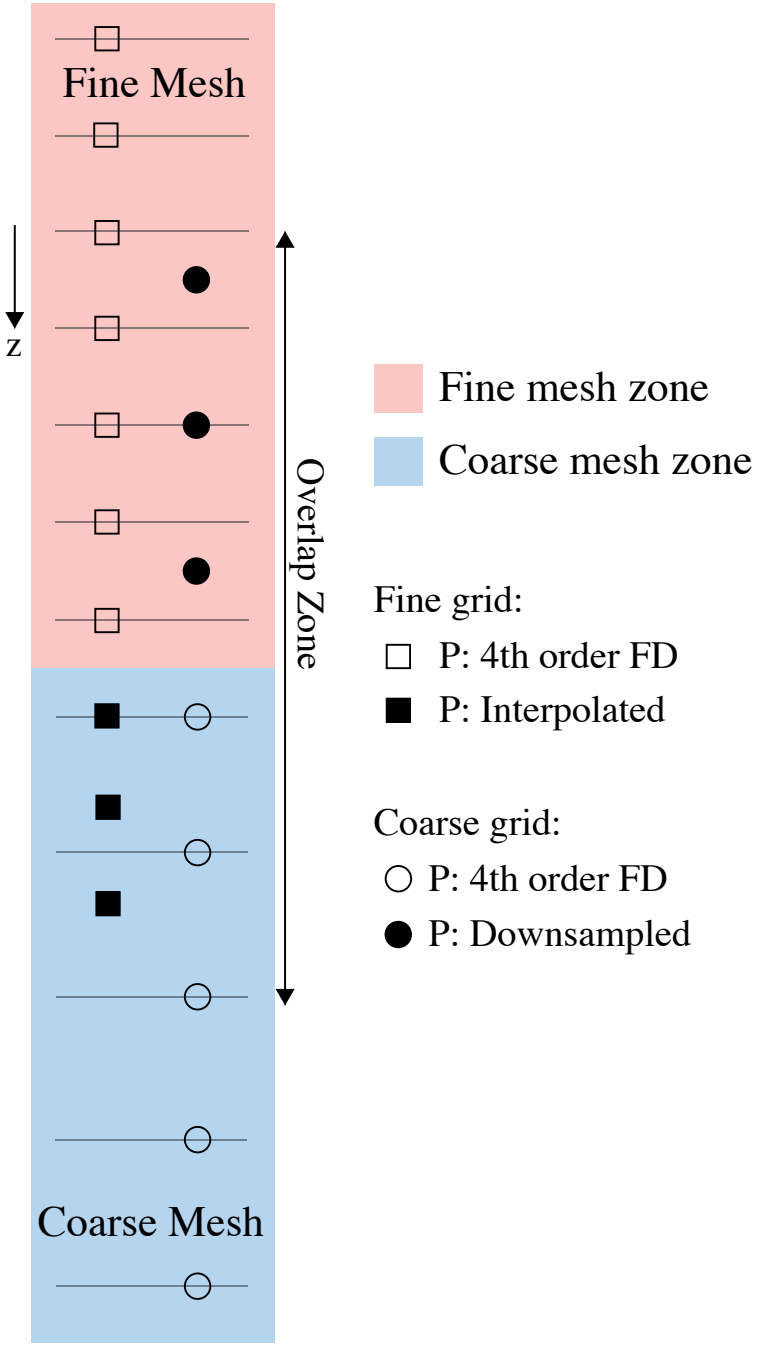

Figure 4.2: Distribution of 4th-order FD acoustic pressure nodes on the z-axis in the overlap zone between the fine and coarse meshes. Open symbols represent nodes that are 4th-order accurate. Filled squares represent nodes that are interpolated from the coarse grid nodes and filled circles represent nodes that are downsampled from the fine grid nodes.

where A_i is the forward modeling operator for region i, $A_{i,j}$ is the interpolation or down-sampling operator from region j to region i, and P_i and F_i are the acoustic pressure and source function for region i, respectively.

The proposed DM FD scheme is a flexible technique that brings significant savings in computational effort and memory requirements. However, certain constraints must be observed. The most important is the number of communication layers across the region interfaces (Figure 4.1). To ensure minimum reflection from the interface, the communication will occur over two and six layers (planes for 3D case) in z-direction for second- and fourth-order FD schemes, respectively. We call the communication layers overlapping planes because it is where differently-spaced grid points overlap in 3D.

4.3 Accuracy of DM

To verify the accuracy of our DM with embedded boundary FD method, we present three scenarios: a homogeneous velocity model with a sloping free surface, a layered velocity model with a hill free surface, and a layered velocity model with realistic topography. For all the tests, we use a point-source and receivers slightly below the surface. The accuracy of our first test is compared with the analytical solution while the following tests are compared with the uniform fine mesh solution that has been thoroughly verified with respect to analytical solutions in AlSalem et al. (2018). For these comparisons, relative error is calculated by:

$$e_{DM}(\mathbf{r}_\Omega) = \frac{||P_{sim}(\mathbf{r}_\Omega)| - |P_R(\mathbf{r}_\Omega)||}{|P_R(\mathbf{r}_\Omega)|} \times 100, \tag{4.8}$$

where $\mathbf{r}_\Omega \in$ region Ω, P_{sim} is the simulation result and P_R is the reference solution.

Homogeneous model with a sloping free surface

The first experiment is performed on a homogeneous velocity model, with a velocity of 5000 m/s and a density of 2000 kg/m^3. The excitation is applied 20 m below and normal to the 10° sloping free surface. Grid spacing discontinuously increases with depth in such a way as to ensure a minimum of 8 points per shortest wavelenghth. A Ricker wavelet with a frequency of 20 Hz and damping 1 $\frac{1}{s}$ is used as the source waveform. Observation points are placed 5 m below and normal to the sloping free surface. The situation is depicted in Figure 4.3.

In the experiment, the DM with embedded boundary method is applied on a second-order FD scheme to calculate the pressure response at observation points. Here, we use two overlapping planes for communication since the FD scheme is second-order. In Figure 4.4, we compare the absolute acoustic pressure values obtained by the analytical solution and DM with embedded boundary. Overall, the average error for the DM method is less than 5% (Figure 4.5).

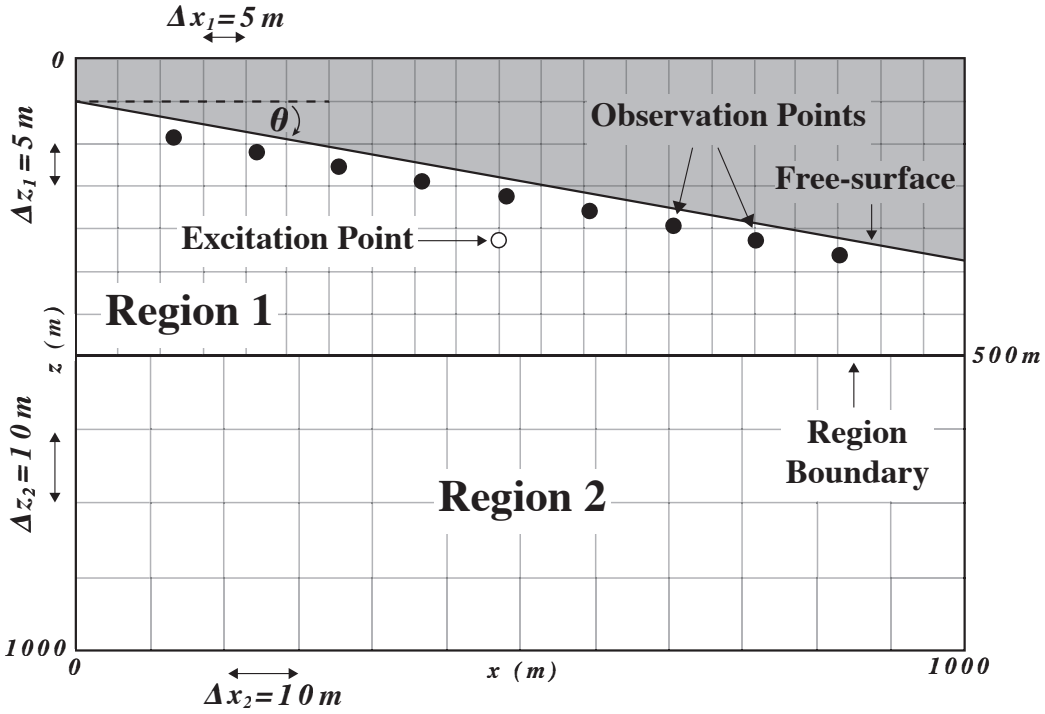

Figure 4.3: Mesh consisting of a sloping free surface and two discontinuous regions. The near-surface observation points are used for calculation of error caused by the embedded boundary and DM methods for a homogeneous model.

Layered model with a hill as free surface

Here, we apply our DM scheme to a layered velocity model under a hill as the free surface. The hill topography and two depth slices, illustrating the layered velocity model with source and receiver locations, are shown in Figure 4.6. The density is 2000 kg/m^3 for all the layers. The uniform simulations have a constant grid size of 5 m. For the DM FD simulations, we place the DM interface at a depth of 750 m, above which the grid size is 5 m, and below which we use 10 m. The overlap zone contains 2 and 6 overlapping planes for the second- and fourth-order DM FD simulations, respectively. The point source is located at (100, 500, 540) m, 40 m below the free surface (Figure 4.6b). We apply a Ricker-wavelet source with a central frequency of 20 Hz. For both the fine- and coarse-grid regions, we sample the minimum spatial wavelength by at least eight nodes.

We compare acoustic pressure solutions between the uniform and DM spatial discretizations at two receiver lines: one is aligned along and 10 m below the free surface and the other is aligned along the z direction and located at $x = 350$ m (see Figure 4.6c). The uniform and DM solutions are nearly identical to the naked eye in both the real and imaginary parts for second- and fourth-order FD solutions (see Figures 4.7 and 4.8), with an average error

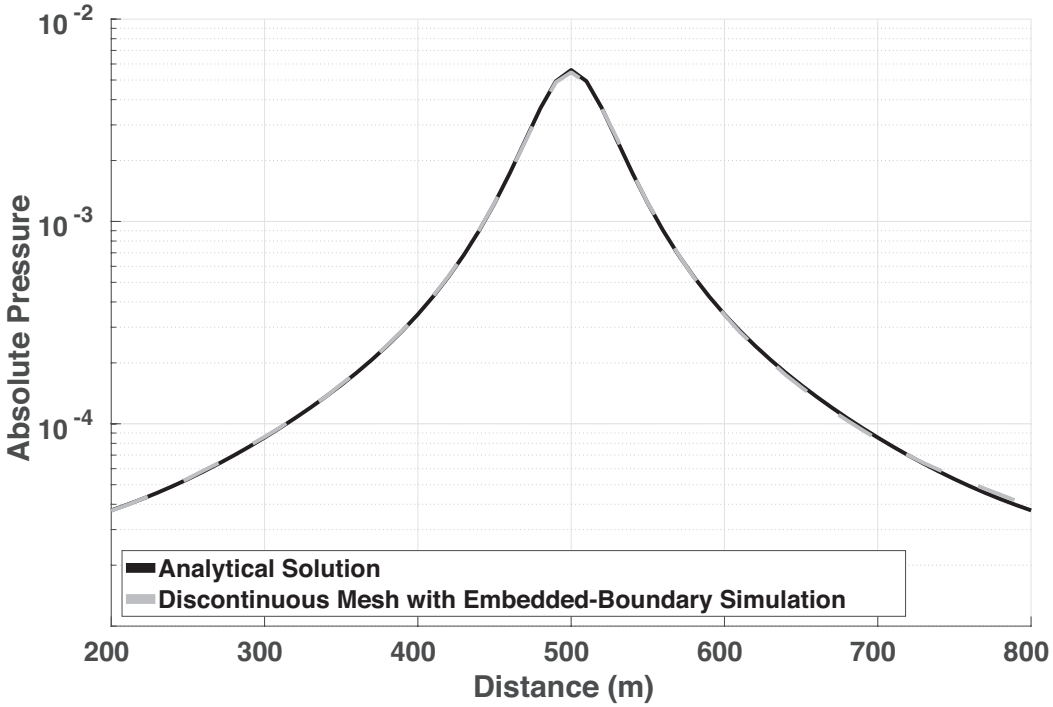

Figure 4.4: Absolute pressure for second-order DM FD with embedded boundary at the observation points in Figure 4.3. The plot demonstrates the solution for a frequency of 20 Hz with damping $1\frac{1}{s}$ relative to the analytical solution.

of less than 5% as shown in Figure 4.9.

Layered model with realistic topography

For our third accuracy test, we apply our DM scheme on a realistic topography surface provided by Saudi Aramco (see Figure 4.10a). The provided model is large in size and contains a high velocity contrast layered model. For the uniform simulations, we use a constant grid size of 10 m. We place the DM interface at a depth of 720 m, above which the grid size is 10 m, and below which we use 15 m. The overlap zone contains 2 overlapping planes for the second-order DM FD simulations. We apply a Ricker wavelet point-source with a central frequency of 10 Hz that is located at (1000, 3000, 340) m (see Figure 4.10b). Similar to our previous tests, the 10 m grid size and 10 Hz frequency allows us to sample the minimum spatial wavelength by at least eight nodes. The frequency is reduced in this simulation to accommodate a larger grid spacing for this spatially large model.

We compare acoustic pressure solutions between the uniform and DM spatial discretizations at two receiver lines: one is aligned along and 10 m below the realistic free surface and the other is aligned along the z directions and located at $x = 3000$ m (see Figure 4.10c). Similar to previous accuracy tests, the solution from the DM is satisfactorily close to the

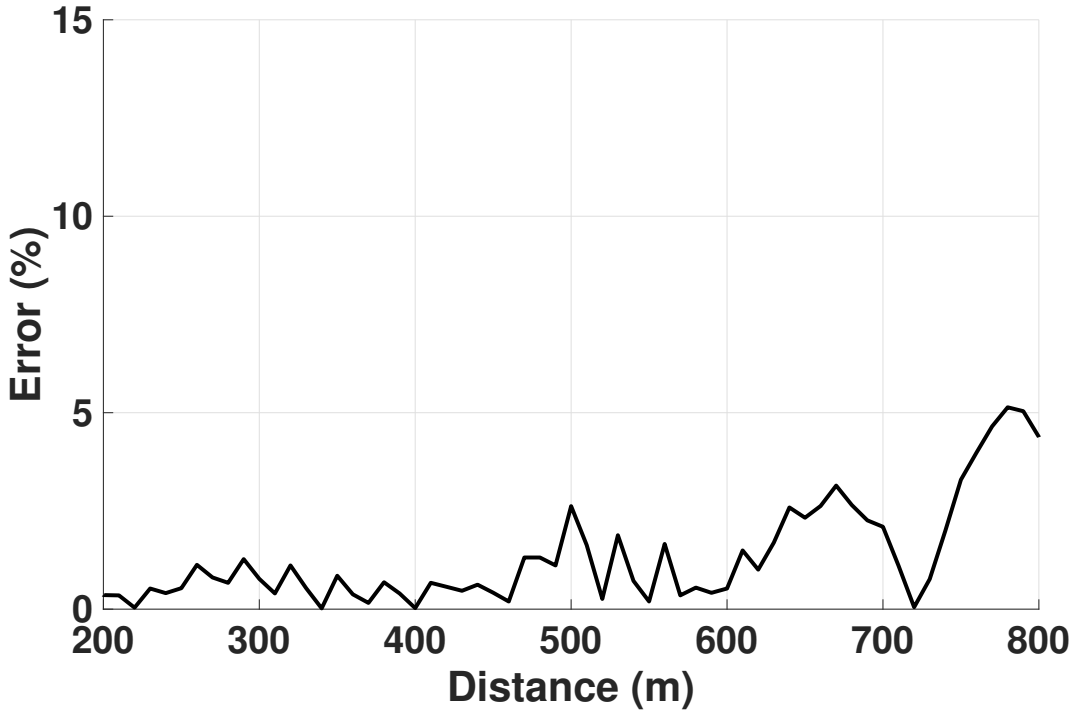

Figure 4.5: Error for second-order DM FD scheme with embedded boundary relative to the analytical solution.

uniform solution in both the real and imaginary parts (see Figures 4.11 and 4.12), with an average error of less than 5% as shown in Figure 4.13. In Figure 4.13a, some points show an inflated error that is caused by having a very small absolute acoustic pressure value near the free surface for the reference uniform fine mesh solution.

4.4 Efficiency and convergence analysis of DM

As discussed above, computational efficiency and convergence is the justification for using a discontinuous staggered-grid mesh instead of a uniform mesh. In this section, we explore solution times for both spatial discretizations using direct and iterative solvers provided by PETSc numerical libraries (Balay et al., 2018). For the direct solvers, we tested MUMPS v5.1.2 (Amestoy et al., 2001, 2006), MUMPS Block Low Rank (BLR) with drop tolerance 10^{-7} (Amestoy et al., 2015) and SuperLU_DIST v5.1.3 (Li et al., 1999; Li and Demmel, 2003; Grigori et al., 2007) and for the iterative solver, we tested the Generalized Minimal Residual (GMRES) method (Saad and Schultz, 1986), all via PETSc. We use NERSC's Cray XC40 supercomputer (Cori), which has 2,388 Intel Xeon "Haswell" processor nodes. Each node has 128 GB DDR4 2133 MHz memory and holds two sockets where each socket is populated with a 16-core Intel® Xeon™ Processor E5–2698 v3 ("Haswell") at 2.3 GHz. We will test efficiency and convergence when implementing DM relative to uniform discretization

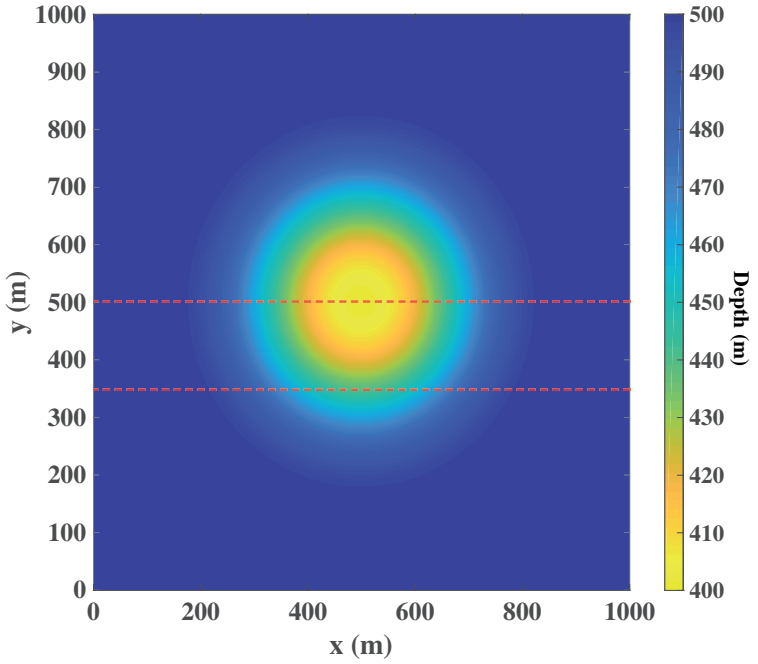

(a) Topography (free surface)

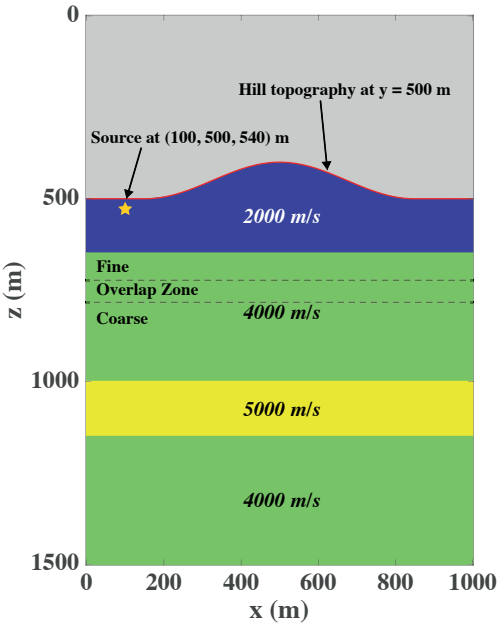

(b) Depth slice at y=500 m

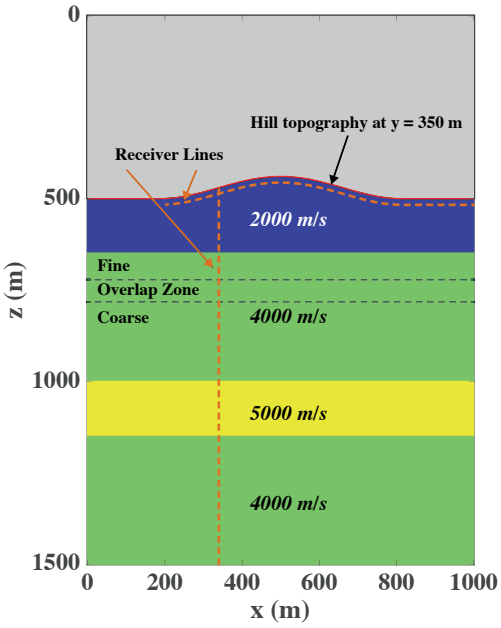

(c) Depth slice at y=350 m

Figure 4.6: (a) Topography of the hill free surface with two *red* lines for cross-sections (b) at $y = 500$ m and (c) at $y = 350$ m. Cross-section (b) shows the source location and cross-section (c) shows the receiver lines.

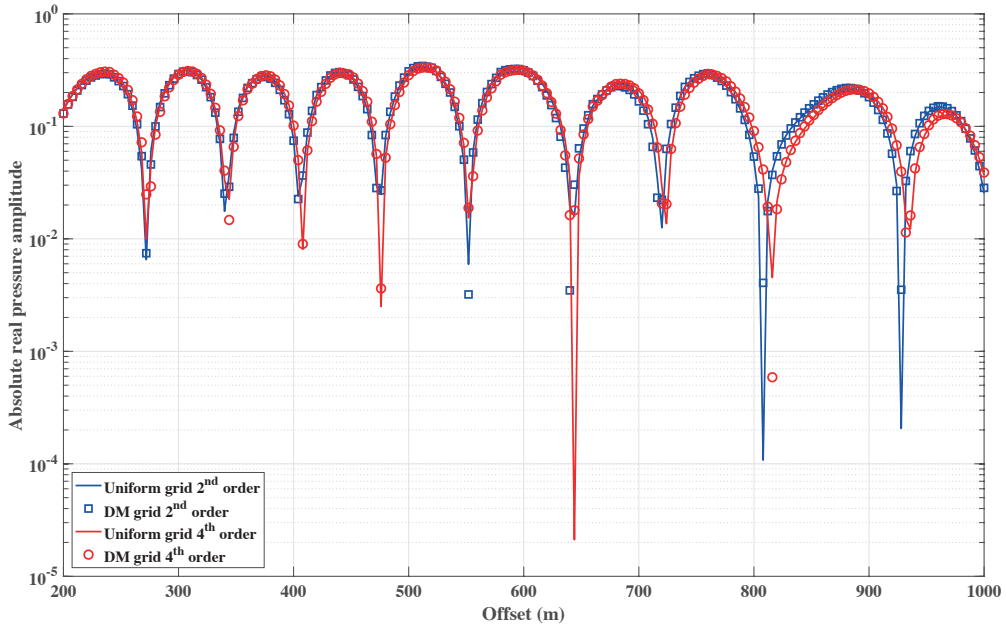

(a) Absolute real part

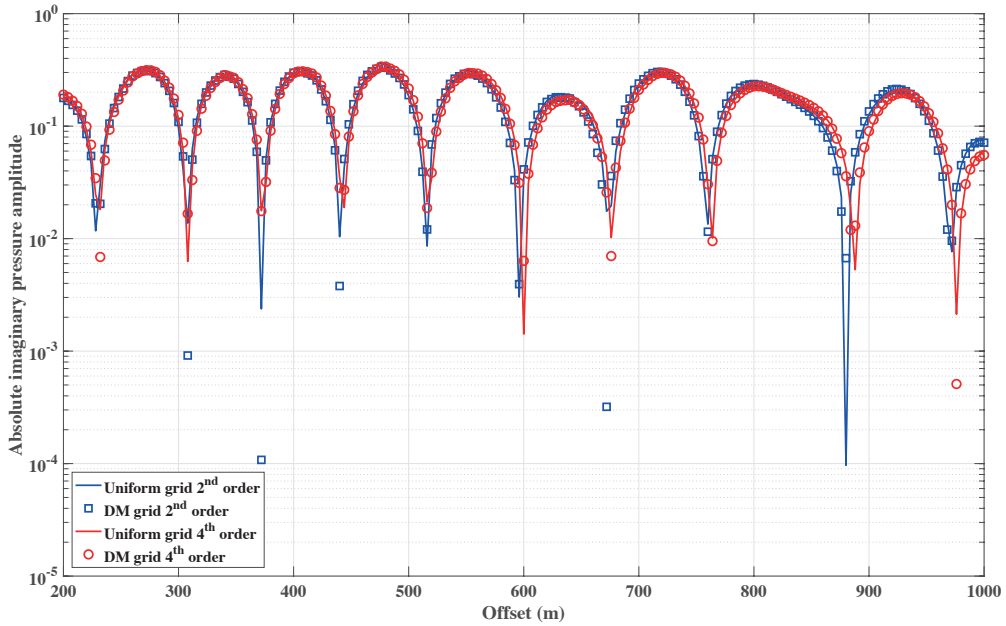

(b) Absolute imaginary part

Figure 4.7: Absolute real and imaginary parts of the pressure solution along the hill free surface for uniform and DM spatial discretizations using second- and fourth-order FD simulations.

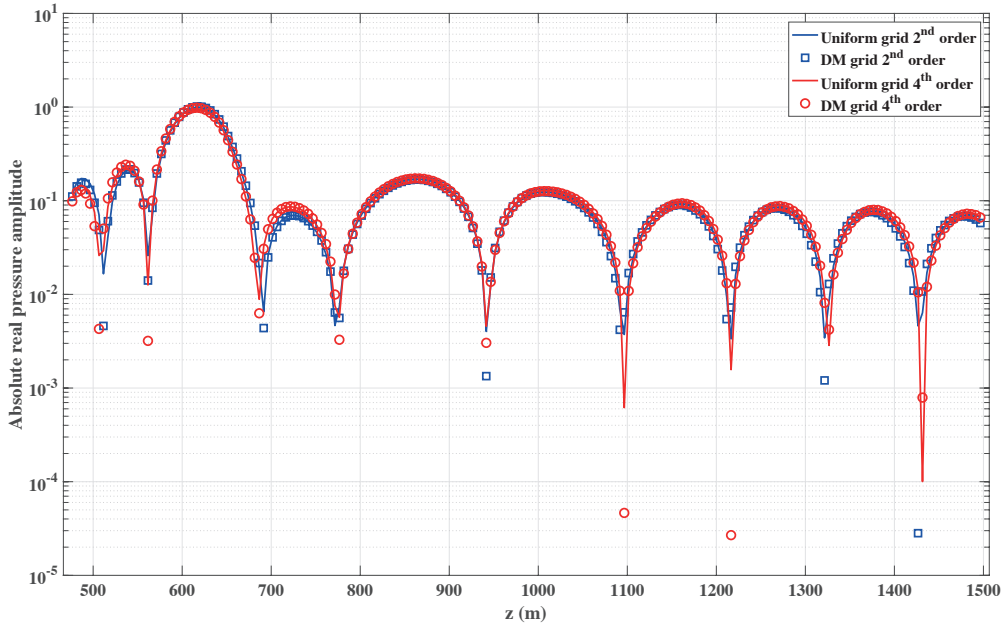

(a) Absolute real part

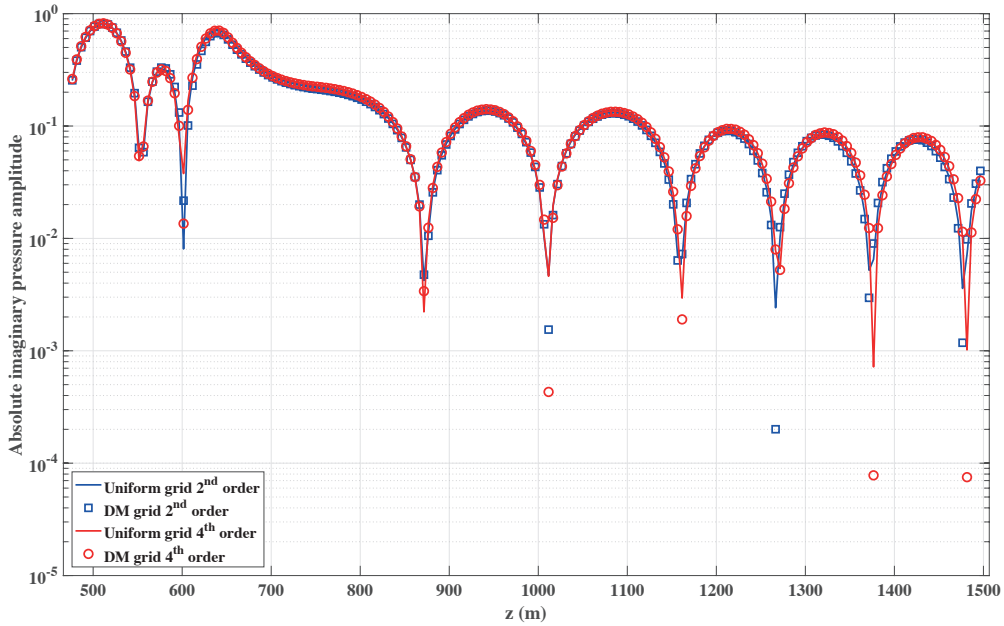

(b) Absolute imaginary part

Figure 4.8: Absolute real and imaginary parts of the pressure solution along the z direction of the hill surface model for uniform and DM spatial discretizations using second- and fourth-order FD simulations.

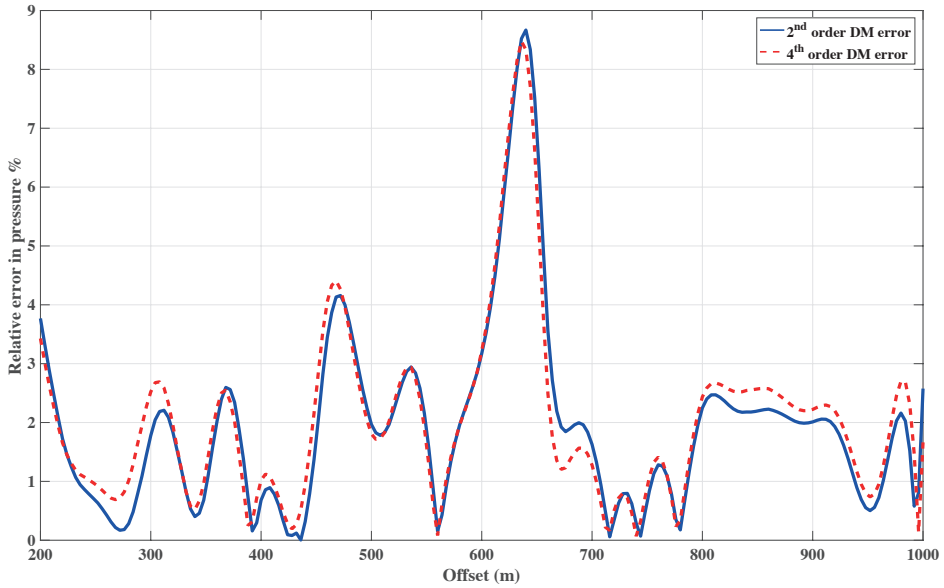

(a) Hill free surface line

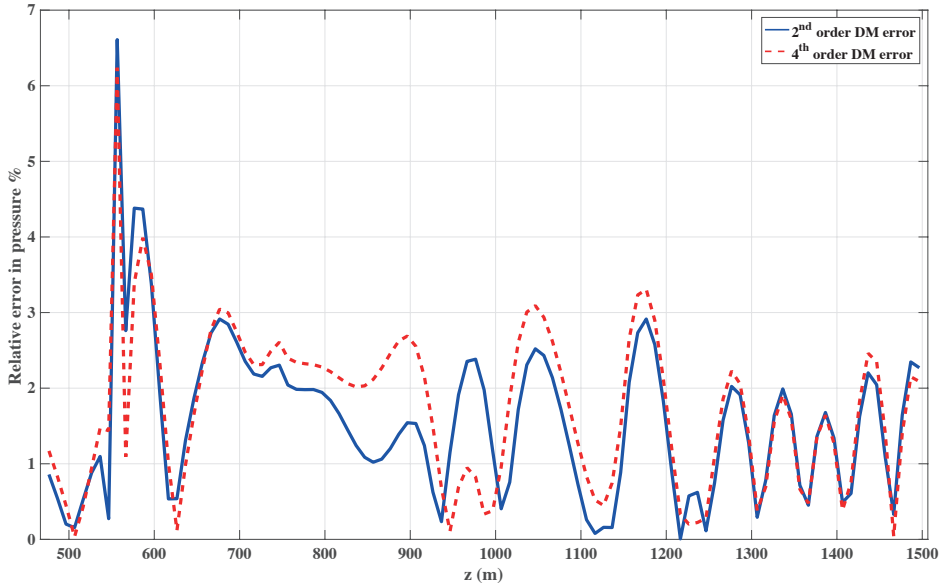

(b) z direction line

Figure 4.9: Absolute relative error in the pressure solution between uniform and DM spatial discretizations along the (a) free surface hill and (b) z direction using second- and fourth-order FD simulations. Here, the reference solution for the second-order DM FD is the second-order uniform fine mesh FD solution and the reference solution for fourth-order DM FD solution is the fourth-order uniform fine mesh FD solution.

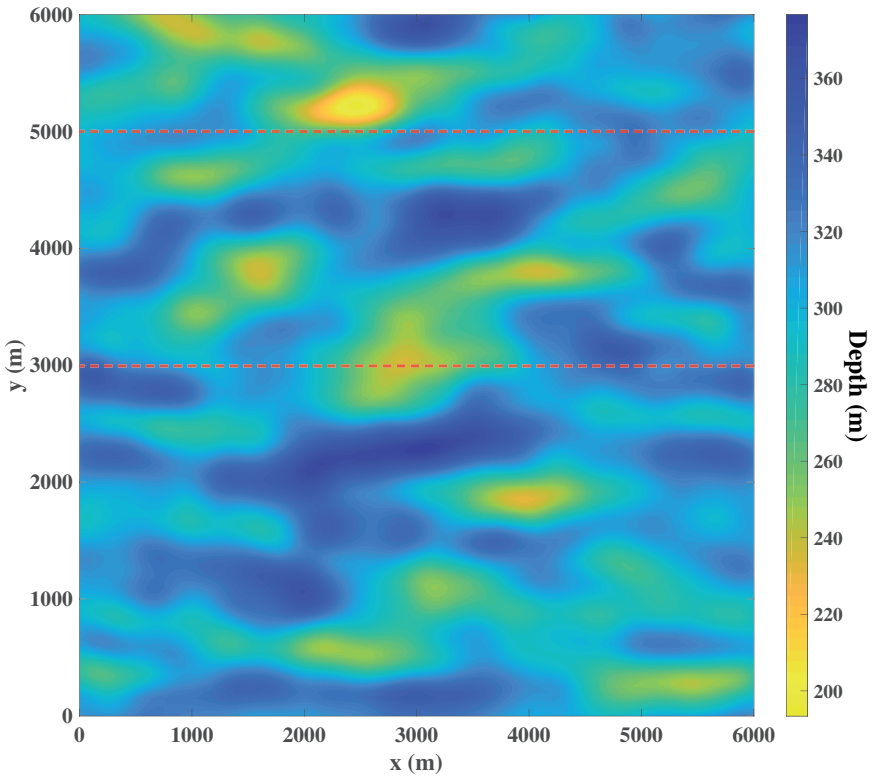

(a) Realistic topography (free surface)

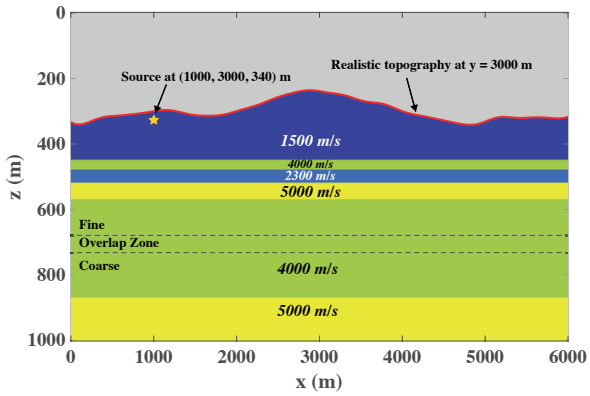

(b) Depth slice at y=3000 m

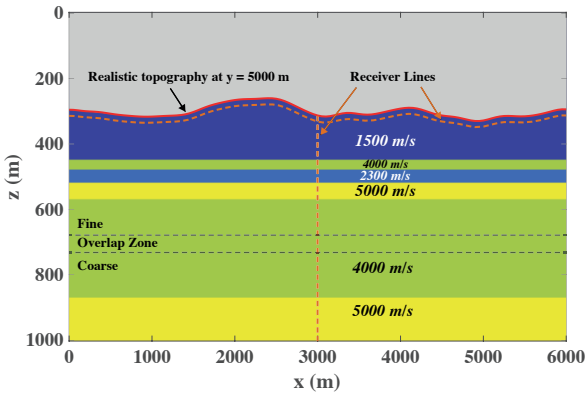

(c) Depth slice at y=5000 m

Figure 4.10: (a) Realistic topography free surface with two *red* lines for cross-sections (b) at $y = 3000$ m and (c) at $y = 5000$ m. Cross-section (b) shows the source location and cross-section (c) shows the receiver lines.

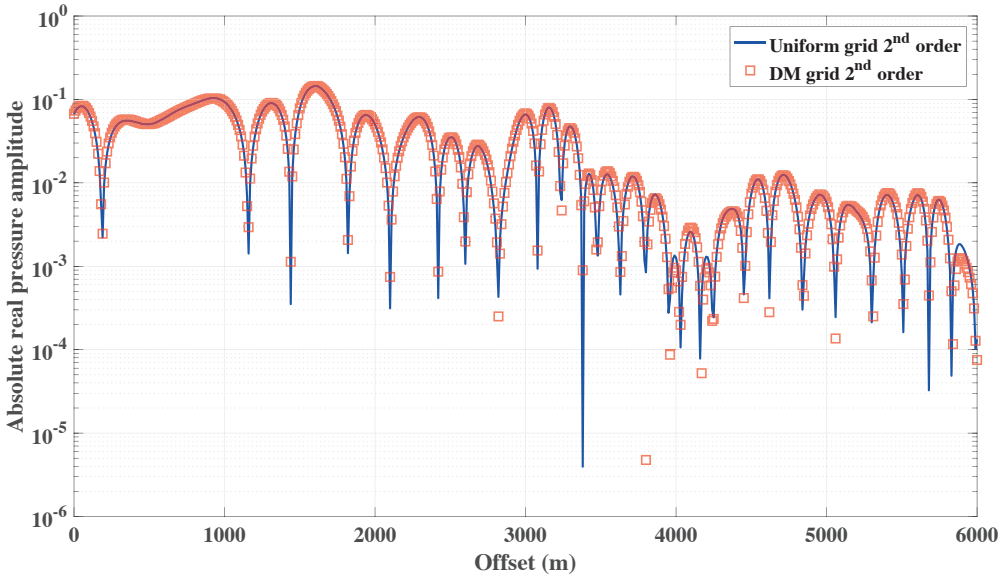

(a) Absolute real part

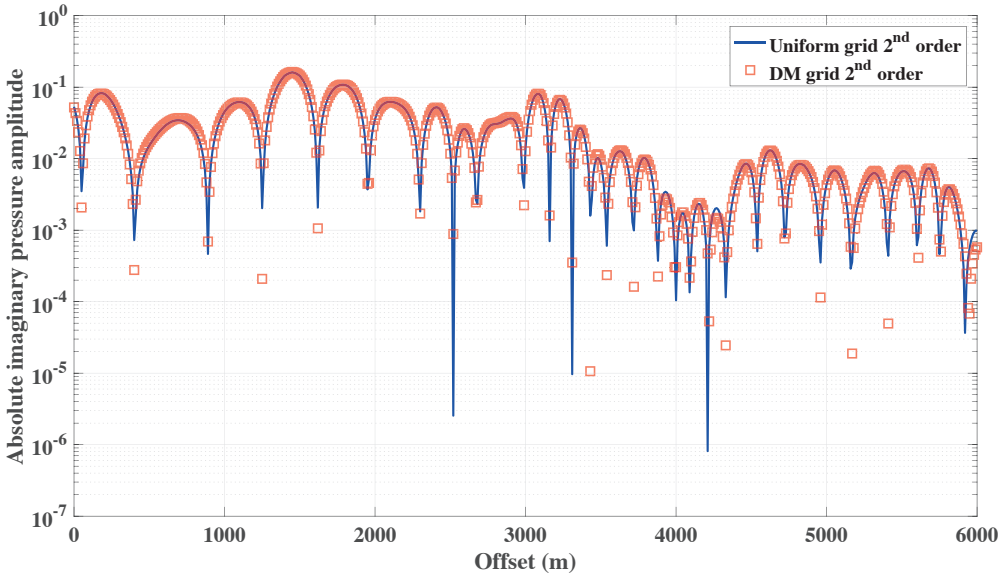

(b) Absolute imaginary part

Figure 4.11: Absolute real and imaginary parts of the pressure solution along the realistic topography free surface for uniform and DM spatial discretizations using second-order FD simulation.

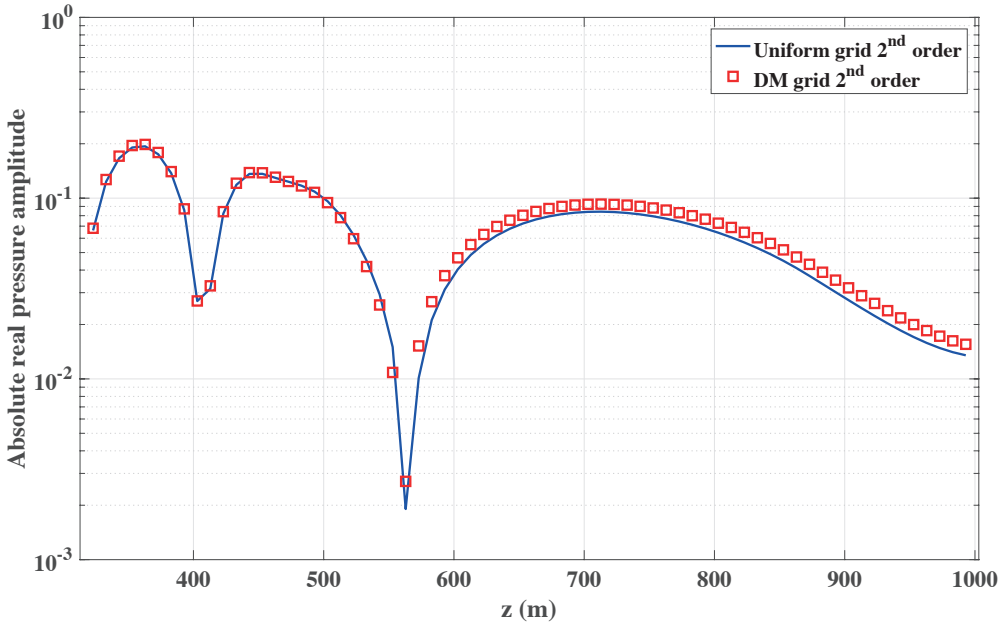

(a) Absolute real part

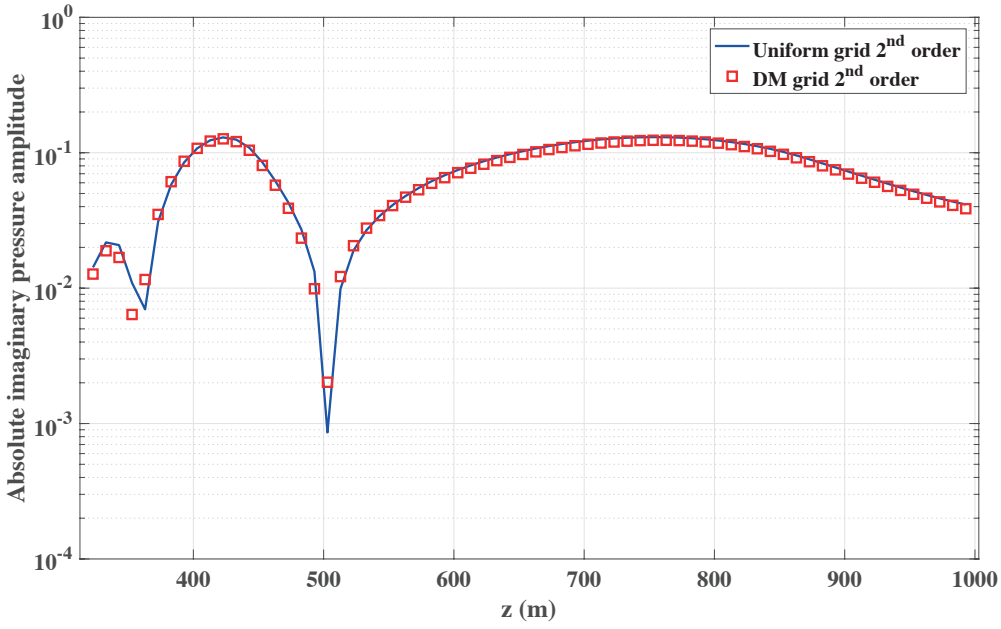

(b) Absolute imaginary part

Figure 4.12: Absolute real and imaginary parts of the pressure solution along the z direction of the realistic topography model for uniform and DM spatial discretizations using second-order FD simulation.

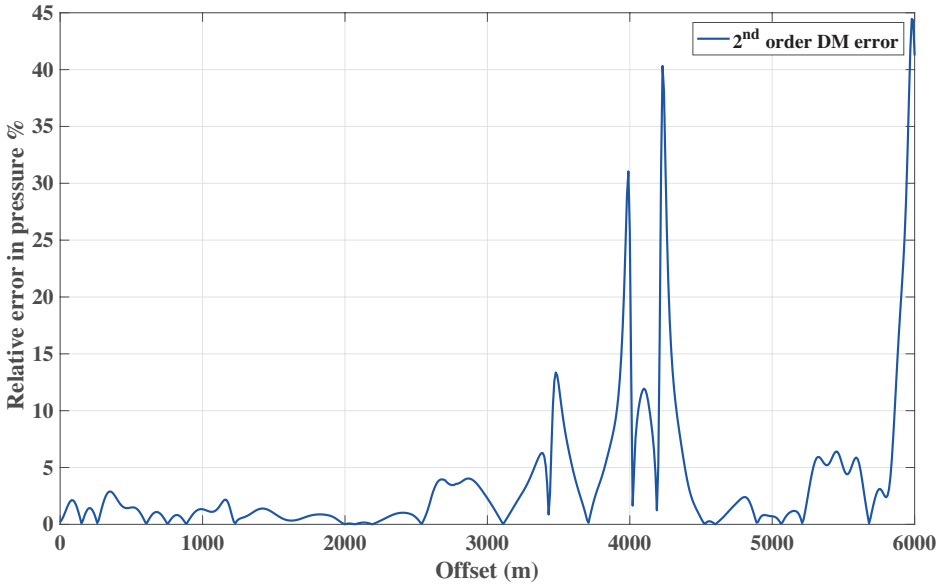

(a) Realistic topography line

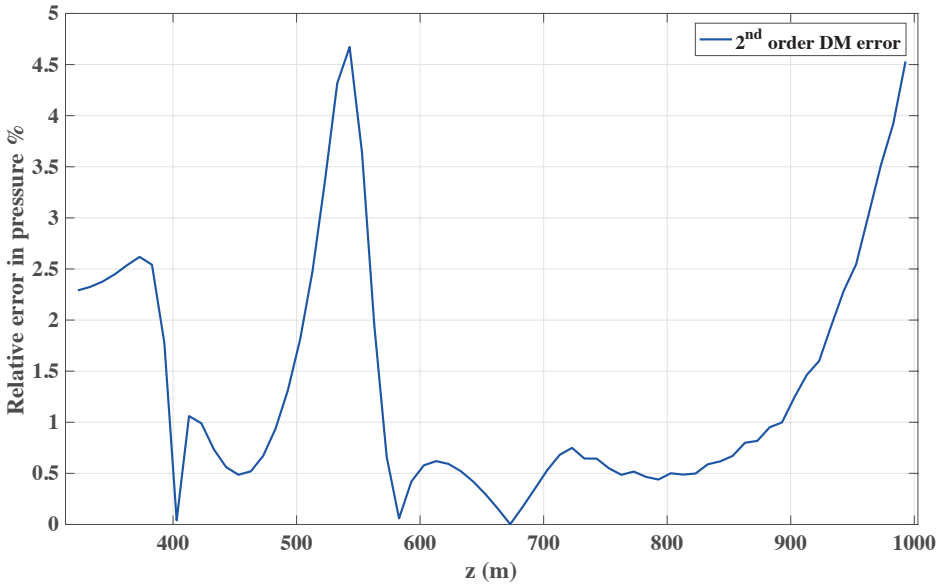

(b) z direction line

Figure 4.13: Absolute relative error in the pressure solution between uniform and DM spatial discretizations along the (a) realistic topography line and (b) z direction using second-order FD simulation. Here, the reference solution for the second-order DM FD is the second-order uniform fine mesh solution and the reference solution for fourth-order DM FD solution is the fourth-order uniform fine mesh FD solution.

Table 4.1: Second-order uniform mesh and DM FD benchmarks of the hill free surface model for several parallel direct and iterative solvers in PETSc numerical libraries.

Spatial discretization	Solver	Nodes	Cores per node	Matrix size	Iterations	Factor time (s)	Solve time (s)
Uniform	GMRES	64	32	13,450,500	17,713	0.00	28.01
DM	GMRES	64	32	8,228,000	16,222	0.00	15.88
DM	MUMPS	64	16	8,228,000	1	792.75	28.98
DM	MUMPS BLR	64	16	8,228,000	2	675.16	39.36
DM	SuperLU_DIST	64	16	8,228,000	1	278.03	5.05

Table 4.2: Fourth-order uniform mesh and DM FD benchmarks of the hill free surface model for several parallel direct and iterative solvers in PETSc numerical libraries.

Spatial discretization	Solver	Nodes	Cores per node	Matrix size	Iterations	Factor time (s)	Solve time (s)
Uniform	GMRES	64	32	13,450,500	23,022	0.00	117.44
DM	GMRES	64	32	8,228,000	20,908	0.00	86.96
DM	MUMPS	64	8	8,228,000	1	2,673.10	30.20
DM	MUMPS BLR	64	8	8,228,000	2	1,191.10	36.39
DM	SuperLU_DIST	64	8	8,228,000	1	1,352.30	11.71

for a layered velocity model with the hill free surface, and the spatially large high-contrast layered velocity model with realistic topography.

Layered model with a hill as free surface

In the first test, we benchmark uniform and DM second- and fourth-order FD simulations of the layered hill free surface model (Figure 4.6). To measure the speed gain without bias, we will use 64 nodes for all the simulations in this section and cap the number of cores per node to 16 for second-order FD and 8 for fourth-order FD to meet direct solvers high memory demands. The second-order FD scheme, which has approximately 7 non-zeros per row in its matrix, shows a speed gain of 1.76 times for DM relative to the uniform fine mesh when using the GMRES iterative solver (Table 4.1 and Figure 4.14a). The fourth-order FD scheme, which has approximately 19 non-zeros per row, shows a speed gain of 1.35 times (Table 4.2 and Figure 4.14b).

To measure the efficiency of direct solvers on DM simulations, we compare them against the GMRES iterative solver on uniform simulations for a large number of sources, where each source is one right-hand side (RHS) in our acoustic wave equation formulation. For the second-order FD test, Figure 4.14a shows a speed gain of more than five times when using SuperLU_DIST and a speed loss when using MUMPS for more than 1000 sources. The speed loss can be attributed to the favorable iterative conditions, which are the low number

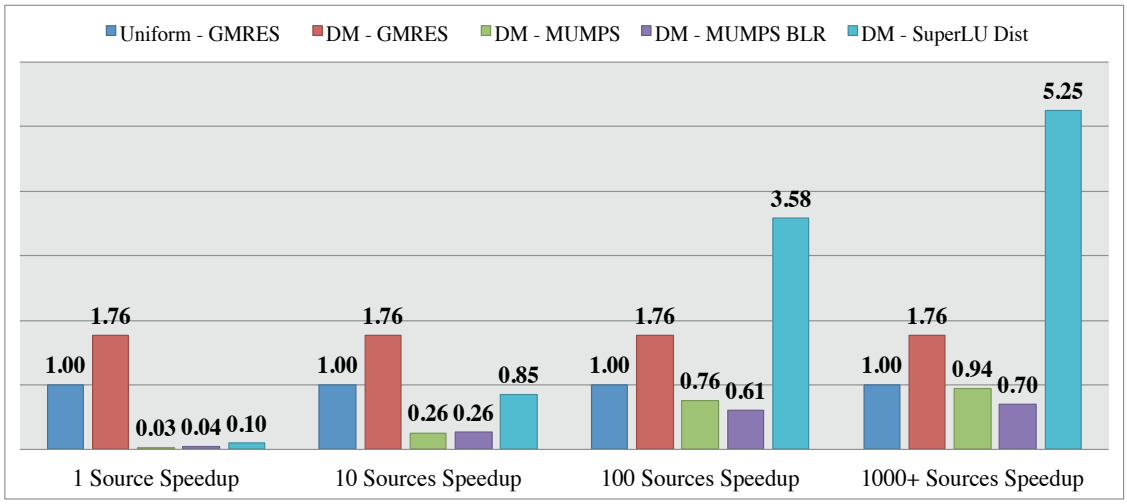

(a) Second-order

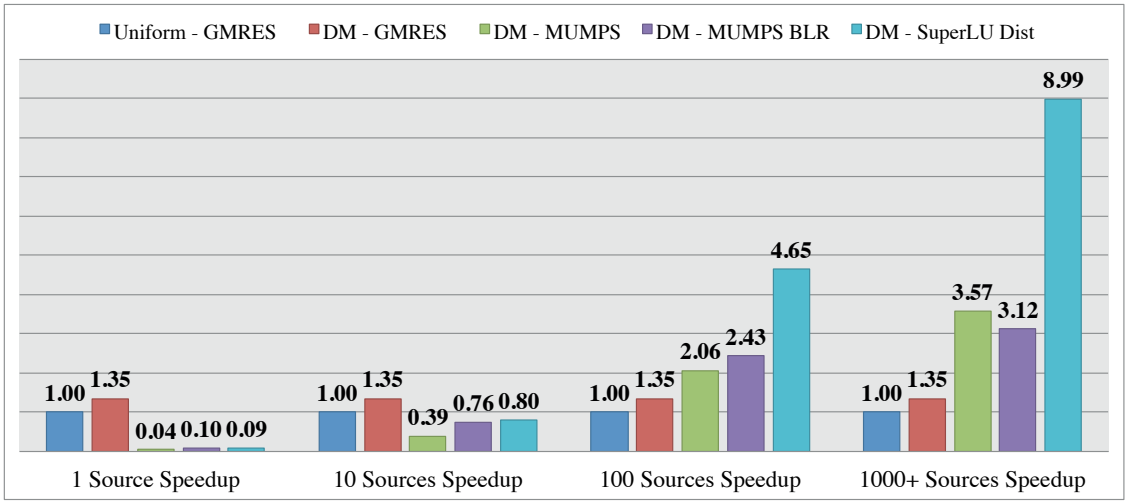

(b) Fourth-order

Figure 4.14: Speedup of (a) second- and (b) fourth-order uniform and DM FD solutions for different parallel direct and iterative solvers in PETSc numerical libraries.

Table 4.3: Second-order uniform and DM FD benchmarks of the realistic topography model for several parallel direct and iterative solvers in PETSc numerical libraries.

Spatial discretization	Solver	Nodes	Cores per node	Matrix size	Iterations	Factor time (s)	Solve time (s)
Uniform	GMRES	128	32	39,070,500	**The problem diverges**		
Uniform	MUMPS	128	4	39,070,500	1	3,955.10	80.45
Uniform	MUMPS BLR	128	4	39,070,500	2	2,229.00	106.97
Uniform	SuperLU_DIST	128	4	39,070,500	**Runs out of memory**		
DM	GMRES	128	32	31,010,012	20,940	0.00	105.76
DM	MUMPS	128	4	31,010,012	1	2,658.60	58.40
DM	MUMPS BLR	128	4	31,010,012	2	1,614.60	97.41
DM	SuperLU_DIST	128	4	31,010,012	1	1,272.22	57.45

of non-zeros and small condition number due to the low velocity contrast between layers. The fourth-order simulation, which has a relatively higher number of non-zeros, shows a speed gain of nine times for SuperLU_DIST and more than three times for both MUMPS and MUMPS BLR when simulating for more than 1000 sources (Figure 4.14b).

Layered model with realistic topography

To examine the influence of the large condition number and high number of non-zeros on solvers, we benchmark uniform mesh and DM second-order FD simulations of the high velocity contrast realistic topography model (Figure 4.10). To keep the benchmarks fair, we use 128 nodes for all simulations and cap the number of cores per node to four for direct solvers.

Table 4.3 shows that the GMRES iterative solver diverges when using the uniform mesh and converges when using our DM discretization. Here, our DM lowers both the number of non-zeros and the condition number of the simulation matrix. We also observed that MUMPS is more memory efficient than SuperLU_DIST for large simulations (Table 4.3). In summary, our benchmarks indicate that DM discretization is faster and more stable than uniform discretization, especially for large models with high velocity contrasts.

Chapter 5

Conclusion

5.1 Embedded boundary methods

We report improved embedded boundary methods for 3D acoustic seismic wave propagation modeling when arbitrarily free-surface topography is present. Unlike the classic staircase method and finite-difference algorithms that use structured curvilinear body-fitted grids, our embedded boundary methods; quadratic interpolation, linear extrapolation, and one- and two-layer hybrid use a regular Cartesian grid system, which greatly simplifies mesh generation and omits the need to change our current finite-difference formalizations. The free-surface boundary is enforced at actual surface locations through the method of images, allowing for an accurate representation of an arbitrary free-surface geometry. As demonstrated with numerical experiments, our embedded methods significantly reduce the staircasing error. Our results showed that the hybrid method is efficient in terms of accuracy and performance for second-order finite-difference while the two-layer hybrid cubic method is more efficient for fourth-order finite-difference implementation. These methods are designed to choose between linear extrapolation and quadratic interpolation according to a tolerance variable without adversely affecting performance. We use a high tuning parameter α to bias the hybrid method to linear extrapolation, for the increase in accuracy that linear extrapolation achieves over quadratic interpolation. Previous published works only take quadratic interpolation into consideration, which makes their embedded methods dependent on nodes further below the surface. Our results show that linear extrapolation, which depends on nodes close to the surface can produce better results. It achieves slightly more accurate results when compared to quadratic interpolation for the oblique planar surface. For the hill irregular surface, it is about two times better than quadratic interpolation. These algorithms can handle any surface topography under a regular Cartesian coordinate system. Therefore, they have significant potential to become a powerful part of a forward-modeling engine used for full waveform inversion.

5.2 Discontinuous mesh method

We implemented a DM with embedded boundary for second- and fourth-order accurate staggered-grid velocity-pressure FD scheme. It approximates the solution of the LF acoustic wave equation with any spacing ratio between the differently-spaced regions. Our method applies trilinear interpolation to update pressure values at nodes needed by the fine mesh from the coarse mesh and downsampling to update pressure values at nodes needed by the coarse mesh from the fine mesh. We show that our DM with embedded boundary scheme is accurate when using two and six overlapping planes for second- and fourth-order FD approximation, respectively. For spatially large and high velocity contrast models, our DM scheme lowers the condition number and the problem size allowing iterative solvers to converge and direct solvers to require less memory. In any case, our DM with embedded boundary FD scheme has the potential to significantly improve the efficiency of uniform FD methods, especially for simulations with realistic topographies, 3D geological settings, and near-surface low velocities. It is also an important step towards realizing a DM solution for the elastic LF wave equation.

Bibliography

Aki, K. and Richards, P. G. (2002). *Quantitative seismology*. University Science Books, Sausalito, Calif., 2nd edition.

AlSalem, H., Petrov, P., Newman, G., and Rector, J. (2018). Embedded boundary methods for modeling 3d finite-difference laplace-fourier domain acoustic-wave equation with free-surface topography. *Geophysics*, 83(5):T291–T300.

Amestoy, P., Ashcraft, C., Boiteau, O., Buttari, A., L'Excellent, J.-Y., and Weisbecker, C. (2015). Improving multifrontal methods by means of block low-rank representations. *SIAM Journal on Scientific Computing*, 37(3):A1451–A1474.

Amestoy, P. R., Duff, I. S., Koster, J., and L'Excellent, J.-Y. (2001). A fully asynchronous multifrontal solver using distributed dynamic scheduling. *SIAM Journal on Matrix Analysis and Applications*, 23(1):15–41.

Amestoy, P. R., Guermouche, A., L'Excellent, J.-Y., and Pralet, S. (2006). Hybrid scheduling for the parallel solution of linear systems. *Parallel Computing*, 32(2):136–156.

Aoi, S. and Fujiwara, H. (1999). 3d finite-difference method using discontinuous grids. *Bulletin of the Seismological Society of America*, 89(4):918–930.

Balay, S., Abhyankar, S., Adams, M. F., Brown, J., Brune, P., Buschelman, K., Dalcin, L., Eijkhout, V., Gropp, W. D., Kaushik, D., Knepley, M. G., May, D. A., McInnes, L. C., Mills, R. T., Munson, T., Rupp, K., Sanan, P., Smith, B. F., Zampini, S., Zhang, H., and Zhang, H. (2018). PETSc Web page. http://www.mcs.anl.gov/petsc.

Bao, H., Bielak, J., Ghattas, O., Kallivokas, L. F., O'Hallaron, D. R., Shewchuk, J. R., and Xu, J. (1998). Large-scale simulation of elastic wave propagation in heterogeneous media on parallel computers. *Computer methods in applied mechanics and engineering*, 152(1-2):85–102.

Bohlen, T. and Saenger, E. H. (2006). Accuracy of heterogeneous staggered-grid finite-difference modeling of rayleigh waves. *Geophysics*, 71(4):T109–T115.

Casarotti, E., Stupazzini, M., Lee, S. J., Komatitsch, D., Piersanti, A., and Tromp, J. (2008). Cubit and seismic wave propagation based upon the spectral-element method: An

advanced unstructured mesher for complex 3d geological media. In *Proceedings of the 16th International Meshing Roundtable*, pages 579–597. Springer.

Fichtner, A. (2011). *Full seismic waveform modelling and inversion*. Springer.

Gottschammer, E. and Olsen, K. (2001). Accuracy of the explicit planar free-surface boundary condition implemented in a fourth-order staggered-grid velocity-stress finite-difference scheme. *Bulletin of the Seismological Society of America*, 91(3):617–623.

Graves, R. W. (1996). Simulating seismic wave propagation in 3d elastic media using staggered-grid finite differences. *Bulletin of the Seismological Society of America*, 86(4):1091–1106.

Griffiths, D. J. (2005). *Introduction to electrodynamics*. AAPT.

Grigori, L., Demmel, J. W., and Li, X. S. (2007). Parallel symbolic factorization for sparse LU with static pivoting. *SIAM J. Scientific Computing*, 29(3):1289–1314.

Hastings, F. D., Schneider, J. B., and Broschat, S. L. (1996). Application of the perfectly matched layer (pml) absorbing boundary condition to elastic wave propagation. *The Journal of the Acoustical Society of America*, 100(5):3061–3069.

Hayashi, K., Burns, D. R., and Toksoz, M. N. (2001). Discontinuous-grid finite-difference seismic modeling including surface topography. *Bulletin of the Seismological Society of America*, 91(6):1750–1764.

Hestholm, S. (1999). Three-dimensional finite difference viscoelastic wave modelling including surface topography. *Geophysical Journal International*, 139(3):852–878.

Hestholm, S. and Ruud, B. (2000). 2d finite-difference viscoelastic wave modelling including surface topography. *Geophysical Prospecting*, 48(2):341–373.

Hustedt, B., Operto, S., and Virieux, J. (2004). Mixed-grid and staggered-grid finite-difference methods for frequency-domain acoustic wave modelling. *Geophysical Journal International*, 157(3):1269–1296.

Jackson, J. D. (2007). *Classical electrodynamics*. John Wiley & Sons.

Jin, J.-M. (2015). *The finite element method in electromagnetics*. John Wiley & Sons.

Jo, C.-H., Shin, C., and Suh, J. H. (1996). An optimal 9-point, finite-difference, frequency-space, 2-d scalar wave extrapolator. *Geophysics*, 61(2):529–537.

Kim, S. and Pasciak, J. E. (2010). Analysis of a cartesian pml approximation to acoustic scattering problems in r2. *Journal of Mathematical Analysis and Applications*, 370(1):168–186.

Komatitsch, D. and Tromp, J. (1999). Introduction to the spectral element method for three-dimensional seismic wave propagation. *Geophysical journal international*, 139(3):806–822.

Kreiss, H.-O. and Petersson, N. A. (2006). An embedded boundary method for the wave equation with discontinuous coefficients. *SIAM Journal on Scientific Computing*, 28(6):2054–2074.

Kristek, J., Moczo, P., and Galis, M. (2010). Stable discontinuous staggered grid in the finite-difference modelling of seismic motion. *Geophysical Journal International*, 183(3):1401–1407.

Li, J., Zhang, Y., and Toksöz, M. N. (2010). Frequency-domain finite-difference acoustic modeling with free surface topography using embedded boundary method. In *SEG Technical Program Expanded Abstracts 2010*, pages 2966–2971. Society of Exploration Geophysicists.

Li, X., Demmel, J., Gilbert, J., iL. Grigori, Shao, M., and Yamazaki, I. (1999). SuperLU Users' Guide. Technical Report LBNL-44289, Lawrence Berkeley National Laboratory.

Li, X. S. and Demmel, J. W. (2003). SuperLU_DIST: A scalable distributed-memory sparse direct solver for unsymmetric linear systems. *ACM Trans. Mathematical Software*, 29(2):110–140.

Lombard, B., Piraux, J., Gélis, C., and Virieux, J. (2008). Free and smooth boundaries in 2-d finite-difference schemes for transient elastic waves. *Geophysical Journal International*, 172(1):252–261.

Lysmer, J. and Drake, L. A. (1972). A finite element method for seismology. *Methods in computational physics*, 11:181–216.

Marfurt, K. J. (1984). Accuracy of finite-difference and finite-element modeling of the scalar and elastic wave equations. *Geophysics*, 49(5):533–549.

Moczo, P. (1989). Finite-difference technique for sh-waves in 2-d media using irregular grids–application to the seismic response problem. *Geophysical Journal International*, 99(2):321–329.

Morse, P. M. and Feshbach, H. (2010). *Methods of theoretical physics, Vol. II*. AAPT.

Nie, S., Wang, Y., Olsen, K. B., and Day, S. M. (2017). Fourth-order staggered-grid finite-difference seismic wavefield estimation using a discontinuous mesh interface (wedmi). *Bulletin of the Seismological Society of America*, 107(5):2183–2193.

Ohminato, T. and Chouet, B. A. (1997). A free-surface boundary condition for including 3d topography in the finite-difference method. *Bulletin of the Seismological Society of America*, 87(2):494–515.

Operto, S., Virieux, J., Amestoy, P., L'Excellent, J.-Y., Giraud, L., and Ali, H. B. H. (2007). 3d finite-difference frequency-domain modeling of visco-acoustic wave propagation using a massively parallel direct solver: A feasibility study. *Geophysics*, 72(5):SM195–SM211.

Pasalic, D. and McGarry, R. (2010). A discontinuous mesh finite difference scheme for acoustic wave equations. In *SEG Technical Program Expanded Abstracts 2010*, pages 2940–2944. Society of Exploration Geophysicists.

Petersson, N. A. and Sjogreen, B. (2014). Sw4 user's guide version 1.1.

Petrov, P. V. and Newman, G. A. (2012). 3d finite-difference modeling of elastic wave propagation in the laplace-fourier domain. *Geophysics*, 77:T137–T155.

Pitarka, A. (1999). 3d elastic finite-difference modeling of seismic motion using staggered grids with nonuniform spacing. *Bulletin of the Seismological Society of America*, 89(1):54–68.

Pratt, R. G. and Worthington, M. (1990). Inverse theory applied to multi-source cross-hole tomography. part 1: Acoustic wave-equation method. *Geophysical prospecting*, 38(3):287–310.

Pujol, J. (2003). *Elastic wave propagation and generation in seismology*. Cambridge University Press, Cambridge ; New York.

Rheinboldt, W. C. (1998). *Methods for solving systems of nonlinear equations*. SIAM.

Saad, Y. and Schultz, M. H. (1986). Gmres: A generalized minimal residual algorithm for solving nonsymmetric linear systems. *SIAM Journal on scientific and statistical computing*, 7(3):856–869.

Sonneveld, P. and van Gijzen, M. B. (2008). Idr (s): A family of simple and fast algorithms for solving large nonsymmetric systems of linear equations. *SIAM Journal on Scientific Computing*, 31(2):1035–1062.

Spivak, M. (1981). *comprehensive introduction to differential geometry. Vol. IV.[A]*. Publish or Perish, Inc., University of Tokyo Press.

Štekl, I. and Pratt, R. G. (1998). Accurate viscoelastic modeling by frequency-domain finite differences using rotated operators. *Geophysics*, 63(5):1779–1794.

Tessmer, E. (2000). Seismic finite-difference modeling with spatially varying time steps. *Geophysics*, 65(4):1290–1293.

Tessmer, E. and Kosloff, D. (1994). 3-d elastic modeling with surface topography by a chebychev spectral method. *Geophysics*, 59(3):464–473.

Tessmer, E., Kosloff, D., and Behle, A. (1992). Elastic wave propagation simulation in the presence of surface topography. *Geophysical Journal International*, 108(2):621–632.

Virieux, J. (1986). P-sv wave propagation in heterogeneous media: Velocity-stress finite-difference method. *Geophysics*, 51(4):889–901.

Wang, Y., Xu, J., and Schuster, G. (2001). Viscoelastic wave simulation in basins by a variable-grid finite-difference method. *Bulletin of the Seismological Society of America*, 91(6):1741–1749.

Zahradník, J., Moczo, P., and Hron, F. (1993). Testing four elastic finite-difference schemes for behavior at discontinuities. *Bulletin of the Seismological Society of America*, 83(1):107–129.

Zahradník, J. and Urban, L. (1984). Effect of a simple mountain range on underground seismic motion. *Geophysical Journal International*, 79(1):167–183.

Zhang, W. and Chen, X. (2006). Traction image method for irregular free surface boundaries in finite difference seismic wave simulation. *Geophysical Journal International*, 167(1):337–353.

Zhang, W., Zhang, Z., and Chen, X. (2012a). Three-dimensional elastic wave numerical modelling in the presence of surface topography by a collocated-grid finite-difference method on curvilinear grids. *Geophysical Journal International*, 190(1):358–378.

Zhang, Y. (2017). *Parallel Goal-Oriented Adaptive Finite Element Modeling For 3D Electromagnetic Exploration*. PhD thesis, San Diego State University.

Zhang, Z., Zhang, W., Li, H., and Chen, X. (2012b). Stable discontinuous grid implementation for collocated-grid finite-difference seismic wave modelling. *Geophysical Journal International*, 192(3):1179–1188.

Appendix A

Second- and fourth-order accurate first derivatives approximation in a staggered grid

A.1 Central formula of order $\mathcal{O}(h^2)$

If the function $f(x)$ can be evaluated at values that lie left and right of x, then the best two-point formula will involve abscissas that are chosen symmetrically on both sides of x.

Assume that $f \in \mathbb{C}^3[a,b]$ and that $x - \frac{h}{2}$, x, $x + \frac{h}{2} \in [a,b]$. The fourth degree Taylor expansions for $f(x + \frac{h}{2})$ and $f(x - \frac{h}{2})$ are:

$$f(x + \frac{h}{2}) = f(x) + \frac{h}{2}f'(x) + \frac{1}{2!}\left(\frac{h}{2}\right)^2 f''(x) + \frac{1}{3!}\left(\frac{h}{2}\right)^3 f^{(3)}(x) + \frac{1}{4!}\left(\frac{h}{2}\right)^4 f^{(4)}(x) + \mathcal{O}(h^5), \tag{A.1}$$

$$f(x - \frac{h}{2}) = f(x) - \frac{h}{2}f'(x) + \frac{1}{2!}\left(\frac{h}{2}\right)^2 f''(x) - \frac{1}{3!}\left(\frac{h}{2}\right)^3 f^{(3)}(x) + \frac{1}{4!}\left(\frac{h}{2}\right)^4 f^{(4)}(x) + \mathcal{O}(h^5). \tag{A.2}$$

After equation A.2 is substracted from equation A.1 and rearangement, the result is:

$$f'(x) = \frac{f(x + \frac{h}{2}) - f(x - \frac{h}{2})}{h} + \mathcal{O}(h^2). \tag{A.3}$$

The first term on the right side of equation A.3 is the second-order accurate central-difference formula and the second term is the truncation error.

A.2 Central formula of order $\mathcal{O}(h^4)$

If the function $f(x)$ can be evaluated at values that lie left and right of x, then the best four-point formula will involve abscissas that are chosen symmetrically on both sides of x.

Assume that $f \in \mathbb{C}^3[a,b]$ and that $x - \frac{3h}{2}$, x, $x + \frac{3h}{2} \in [a,b]$. The fourth degree Taylor expansions for $f(x + \frac{3h}{2})$ and $f(x - \frac{3h}{2})$ are:

$$f(x+\frac{3h}{2}) = f(x) + \frac{3h}{2}f'(x) + \frac{1}{2!}\left(\frac{3h}{2}\right)^2 f''(x) + \frac{1}{3!}\left(\frac{3h}{2}\right)^3 f^{(3)}(x) + \frac{1}{4!}\left(\frac{3h}{2}\right)^4 f^{(4)}(x) + \mathcal{O}(h^5), \tag{A.4}$$

$$f(x-\frac{3h}{2}) = f(x) - \frac{3h}{2}f'(x) + \frac{1}{2!}\left(\frac{3h}{2}\right)^2 f''(x) - \frac{1}{3!}\left(\frac{3h}{2}\right)^3 f^{(3)}(x) + \frac{1}{4!}\left(\frac{3h}{2}\right)^4 f^{(4)}(x) + \mathcal{O}(h^5). \tag{A.5}$$

After equation A.2 is substracted from equation A.1, we get:

$$f\left(x+\frac{h}{2}\right) - f\left(x-\frac{h}{2}\right) = hf'(x) + \frac{2}{3!}\left(\frac{h}{2}\right)^3 f^{(3)}(x) + \mathcal{O}(h^5), \tag{A.6}$$

and after equation A.5 is substracted from equation A.4, we get:

$$f\left(x+\frac{3h}{2}\right) - f\left(x-\frac{3h}{2}\right) = 3hf'(x) + \frac{2}{3!}\left(\frac{3h}{2}\right)^3 f^{(3)}(x) + \mathcal{O}(h^5). \tag{A.7}$$

By multiplying equation A.6 by $\frac{9}{8}$ and equation A.7 by $-\frac{1}{24}$ and adding them, the result is:

$$\begin{aligned} f'(x) &= \frac{-\frac{1}{24}f\left(x+\frac{3h}{2}\right) + \frac{9}{8}f\left(x+\frac{h}{2}\right) - \frac{9}{8}f\left(x-\frac{h}{2}\right) + \frac{1}{24}f\left(x-\frac{3h}{2}\right)}{h} + \mathcal{O}(h^4) \\ &= \frac{-f\left(x+\frac{3h}{2}\right) + 27f\left(x+\frac{h}{2}\right) - 27f\left(x-\frac{h}{2}\right) + f\left(x-\frac{3h}{2}\right)}{24h} + \mathcal{O}(h^4). \end{aligned} \tag{A.8}$$

The first term on the right side of equation A.8 is the fourth-order accurate central-difference formula and the second term is the truncation error.

Appendix B

Piecewise free-surface equation

Using topography data points $T_{i,j}$, a piecewise quadratic topography equation $f_{i,j}(x,y)$ is approximated. The quadratic approximation in multiple variables is given by:

$$\begin{aligned} f_{i,j}(x,y) \approx\ & f_{i,j}(x_0,y_0) + \partial_x f_{i,j}(x_0,y_0)(x-x_0) + \partial_y f_{i,j}(x_0,y_0)(y-y_0) + \\ & \frac{1}{2!}\left[\partial_{xx} f_{i,j}(x_0,y_0)(x-x_0)^2 + 2\partial_{xy} f_{i,j}(x_0,y_0)(x-x_0)(y-y_0) + \right. \\ & \left. \partial_{yy} f_{i,j}(x_0,y_0)(y-y_0)^2\right], \end{aligned} \tag{B.1}$$

where $f_{i,j}(x,y)$ is the approximated topography equation for the surface about the point (x_0,y_0), and the symbols ∂_x, ∂_y, ∂_{xx}, ∂_{xy}, and ∂_{yy}, respectively denote the partial differential operators $\frac{\partial}{\partial x}$, $\frac{\partial}{\partial y}$, $\frac{\partial^2}{\partial x^2}$, $\frac{\partial^2}{\partial x \partial y}$, and $\frac{\partial^2}{\partial y^2}$, respectively. Furthermore, the piecewise Eq. B.1 is bounded by:

$$\begin{cases} x_{i-1} < x < x_{i+1} \\ y_{i-1} < y < y_{i+1}. \end{cases} \tag{B.2}$$

where i and j are the indices of the topography nodes. Thus, x_i corresponds to $i \cdot h_x$ and y_j to $j \cdot h_y$. The coefficients of Eq. B.1 are found by the central finite-difference relationships. We use topography data points to calculate the coefficients of the equation:

$$\begin{aligned} \partial_x f_{i,j}(x,y) &\approx \frac{T_{i+1,j} - T_{i-1,j}}{2h_x}, \\ \partial_y f_{i,j}(x,y) &\approx \frac{T_{i,j+1} - T_{i,j-1}}{2h_y}, \\ \partial_{xx} f_{i,j}(x,y) &\approx \frac{T_{i+1,j} - 2T_{i,j} + T_{i-1,j}}{h_x^2}, \\ \partial_{xy} f_{i,j}(x,y) &\approx \frac{T_{i+1,j+1} - T_{i-1,j+1} - T_{i+1,j-1} + T_{i-1,j-1}}{4h_x h_y}, \\ \partial_{yy} f_{i,j}(x,y) &\approx \frac{T_{i,j+1} - 2T_{i,j} + T_{i,j-1}}{h_y^2}. \end{aligned} \tag{B.3}$$

The best-fit surface equation can then be approximated by:

$$f_{i,j}(x,y) \approx p_{00} + p_{10}x + p_{01}y + p_{20}x^2 + p_{11}xy + p_{02}y^2, \tag{B.4}$$

where the coefficients are given by:

$$\begin{aligned}
p_{20} &= \frac{1}{2}\partial_{xx} f_{i,j}(0,0) = \frac{1}{2} \cdot \frac{T_{i+1,j} - 2T_{i,j} + T_{i-1,j}}{h_x^2}, \\
p_{02} &= \frac{1}{2}\partial_{yy} f_{i,j}(0,0) = \frac{1}{2} \cdot \frac{T_{i,j+1} - 2T_{i,j} + T_{i,j-1}}{h_y^2}, \\
p_{11} &= \partial_{xy} f_{i,j}(0,0) \\
&= \frac{T_{i+1,j+1} - T_{i-1,j+1} - T_{i+1,j-1} + T_{i-1,j-1}}{4h_x h_y}, \\
p_{10} &= \partial_x f_{i,j}(0,0) = \frac{T_{i+1,j} - T_{i-1,j}}{2h_x} - 2x_0 p_{20} - y_0 p_{11}, \\
p_{01} &= \partial_y f_{i,j}(0,0) = \frac{T_{i,j+1} - T_{i,j-1}}{2h_y} - 2y_0 p_{02} - x_0 p_{11}, \\
p_{00} &= f_{i,j}(0,0) = T_{i,j} - x_0 \cdot \frac{T_{i+1,j} - T_{i-1,j}}{2h_x} - \\
&\qquad y_0 \cdot \frac{T_{i,j+1} - T_{i,j-1}}{2h_y} + x_0^2 p_{20} + \\
&\qquad x_0 y_0 p_{11} + y_0^2 p_{02},
\end{aligned} \tag{B.5}$$